WAYNE

1026
8841

Non-Propagating Cracks in Vee-Notched Specimens Subject to Fatigue Loading

N. E. FROST

(Mechanical Engineering Research Laboratory, East Kilbride, Glasgow)

SUMMARY: Reversed direct stress and rotating bending fatigue tests have been carried out on Vee-notched specimens of aluminium alloy, nickel chromium steel and mild steel.

Diagrams are presented showing the relationship between the geometric stress concentration factor K_t and the strength reduction factor K_f. It was found that non-propagating cracks formed in the roots of the sharper notches. These cracks formed at or above some critical value of K_t, the value depending on the specimen material. Below the critical value of K_t, cracks did not form unless the applied nominal stress exceeded that at the fatigue limit, and a crack, once formed, continued to propagate until the specimen failed. Above the critical value of K_t, non-propagating cracks formed at nominal stresses less than the fatigue limit, the stress having to be increased to the latter value in order to propagate the crack. This critical value of K_t coincided with the maximum K_f value realised. It would appear that K_f equals K_t up to a certain value of K_t; there is then a transition where K_f reaches a maximum at the critical value of K_t. Increasing the value of K_t above the critical value causes no further increase and may tend to decrease the value of K_f.

The conclusions drawn apply only when the fatigue stresses are completely reversed, *i.e.* the mean load is zero.

1. Introduction

The problem of assessing the effect of a stress raiser on the fatigue properties of a material has been the subject of a considerable amount of work. Simply stated, the problem is to derive the value of K_f (the strength reduction factor represented by actual behaviour) from the value of K_t (the geometric stress concentration factor) for the stress raiser in question. K_t is defined as the ratio of the maximum stress in the neighbourhood of the stress raiser to the nominal stress assuming perfect elasticity and can be obtained in certain cases by mathematical analysis or can be determined experimentally, usually by photoelastic techniques. Under conditions of fatigue loading, maximum stress values less than the yield point of the material can cause failure, and hence the value of K_t should be important. In static loading, on

Received December 1955.

[The Aeronautical Quarterly, Vol. VIII, February 1957]

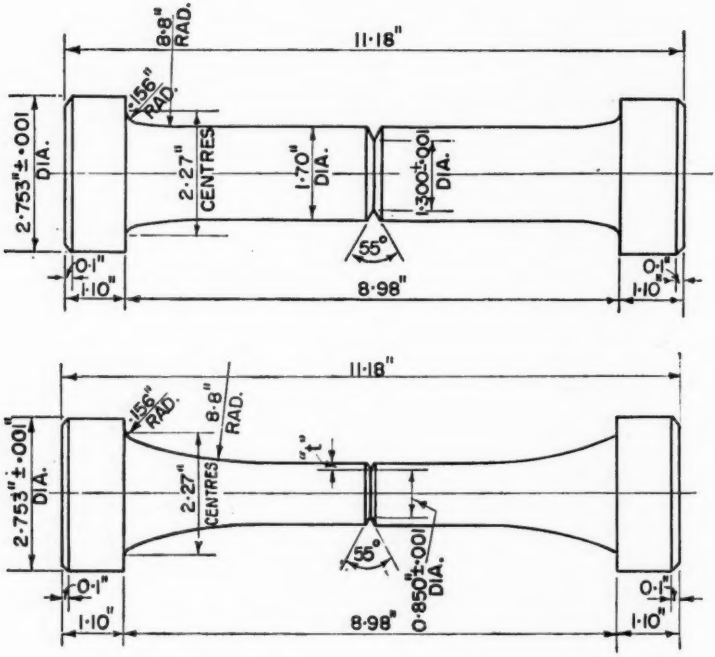

Fig. 1.
Fatigue specimens for direct stress machines (with notch).

the other hand, plastic flow will occur at stresses above the yield point and will alter the elastic stress field around the stress raiser before final failure occurs. As the value of K_t is based on the maximum principal stress, reference to this factor assumes that failure depends on the maximum principal stress. However, combined stress fatigue tests show that for ductile materials failure obeys the von Mises criterion more closely than that of maximum principal stress. Peterson[1], assuming the von Mises criterion of failure to apply, has computed values of a geometric elastic stress concentration factor, which he terms K_t', for several types of stress raisers. The value of K_t' is never greater than K_t, and the maximum possible difference between the two factors is about 15 per cent. As differences much larger than this are found between K_t and K_f, K_t is usually preferred to K_t' on the grounds of greater simplicity.

Much work has been devoted to the experimental determination of K_f, but mostly in small rotating beam machines, and comparatively few tests have been made in reversed direct stress using large specimens.

It is not intended to go into detail regarding the relationships that have been suggested to connect K_t and K_f (*e.g.* the conception of a notch sensitivity index

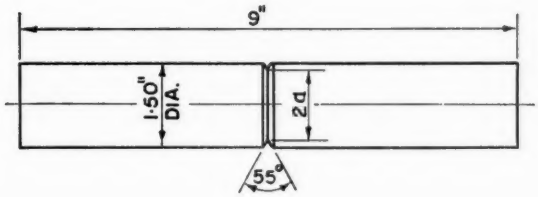

Fig. 2.
Fatigue specimen for rotating bending fatigue machine (with notch).

$q=(K_f-1)/(K_t-1)$ or Kuhn and Hardrath's work[3] based on Neuber's[4] elementary structural unit); examples of these have been collected and discussed by Dolan and Yen[2]. Several Authors, *e.g.* Phillips and Heywood[5], Hikata[6] and Dolan and Hanley[7], have found that, for geometrically similar test pieces, K_f increases with absolute size of test piece. This is termed "size effect." In contrast to these findings, Hyler, Lewis and Grover[8] and Ros and Eichinger[9], appear to find no appreciable size effect for the normal range of sizes met in practice. However, Ros and Eichinger[9] state that a size effect is apparent for very sharp discontinuities.

A further point which will be brought out later is that several authors, *e.g.* Mann[10], Hyler, Lewis and Grover[8], and Ros and Eichinger[9], have found that the sharpest notch does not necessarily have the greatest weakening effect. Mann[10], working with an aluminium alloy 24 S-T in rotating beam tests, found that a notch with a K_t value of 5·8 gave a maximum K_f value of 3·2, K_f decreasing with further increase in K_t. Frost and Phillips[11], from work on the fatigue strength of cracked specimens, suggested that the sharpest notch is not necessarily the most damaging. In the present paper the effect on the relationship between K_t and K_f of the formation of a non-propagating crack at the root of the stress raiser is considered. The presence of such non-propagating cracks has been reported by Fenner, Owen and Phillips[12] for mild steel and Frost[13] for aluminium alloy. For both materials cracks were found at the roots of Vee-notched specimens at stresses from about ± 1 ton/in.^{2} up to the nominal fatigue limit in specimens run for $30 - 100 \times 10^6$ cycles and which normally would be considered unbroken. Further experimental data are presented in the paper regarding the relation of the notch dimensions to the formation of such non-propagating cracks.

NOTATION

K_f	strength reduction factor	
K_t	geometric elastic stress concentration factor	
K_t'	geometric elastic stress concentration factor (Ref. 1)	
a	radius of minimum cross section of specimen	*See* Fig 3
t	notch depth	
r	root radius	

2. Experimental Details

Three materials were used for the investigation:—a 0·15 per cent carbon mild steel, a nickel chromium steel (EN 26) and an aluminium alloy (BS L65). Details of their chemical composition and mechanical properties are given in Table I.

Fatigue tests on notched specimens were carried out under both reversed direct stress and rotating bending. For both these types of loading the mean load of the cycle is zero and hence the applied nominal stress cycle is completely reversed. The types of specimen used in direct stress are shown in Fig. 1, while that used in rotating bending is shown in Fig. 2. Fig. 3 illustrates the dimensions a, t and r used to describe the notch. In all cases a Vee type of notch with an included angle of 55° was used. Great care was taken in the machining of the notches; the accuracy of the root radii obtained can be seen from the various sectional photographs given in the paper.

The reversed direct stress tests were done in a Schenck type fatigue testing machine running at approximately 1,800 cycles/min., while the rotating bending tests were made in a 10,000 in. lb. capacity Sonntag four-point loading machine running at 3,000 r.p.m.

Specimens which were unbroken after running for $10 - 30 \times 10^6$ cycles were examined microscopically as detailed in Ref. 13. Briefly, the section of the specimen containing the notch was sawn across two mutually perpendicular diameters, thus exposing four different faces for viewing. The specimens were polished and etched in the usual manner.

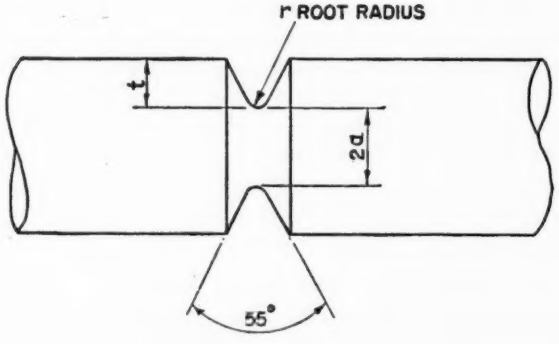

Fig. 3.
Dimensions of notch in terms of a, t and r.

TABLE I

DETAILS OF MATERIALS USED

Material	*Symbol*	*Chemical analysis* (per cent)	*Heat treatment*	*Tensile strength* (tons/in.²)	*0·1 per cent proof stress* (tons/in.²)	*Elongation on 4 √(area)* (per cent)
Mild steel	TON	0·15 C 0·45 Mn 0·014 S 0·015 P	Normalise 920°C	29	22 (yield stress)	30
Nickel chromium steel	RSU	0·43 C 2·64 Ni 0·75 Cr 0·65 Mn 0·58 Mo 0·05 Va 0·32 Si 0·012 P 0·012 S	850°C oil quench 650°C air cool	63	54 (yield stress)	24
Aluminium alloy	MBCG MBHQ	4·4 Cu 0·7 Mg 0·7 Si 0·6 Mn	505°C water quench age 160-190°C	32	28	8

TABLE II

VEE-NOTCHED ALUMINIUM ALLOY SPECIMENS

Values of Fatigue Limit, K_t, K_f

and Remarks on the Microscopic Examination of Notch Root

r (in.)	*a* (in.)	*t* (in.)	*Fatigue endurance limit* (tons/in.²)	K_t	K_f	*Microscopic examination and photograph figure number*
			Reversed Direct Stress			
0·05	0·65	0·2	±3	3·3	3·2	No crack detected (Fig. 6).
0·02	0·65	0·2	±2	4·85	4·85	No crack detected (Fig. 7).
0·008	0·65	0·2	±1·5	7·3	6·5	No crack detected (Fig. 8).
0·004	0·65	0·2	±1·5	10	6·5	Small crack inclined at 45° to applied load (Fig. 9).
0·002	0·65	0·2	±2·5	14	3·9	Crack at 90° to applied load (Fig. 10).
0·0005 (approx.)	0·65	0·2	±2·6	27	3·7	Crack at 90° to applied load. Multi-cracks formed (Fig. 11).
			Rotating Bending			
0·02	0·55	0·2	±3·4 (approx.)	3·8	2·85	No crack detected (Fig. 12).
0·008	0·70	0·05	±3·4	4·9	2·85	No crack detected (Fig. 13).
0·002	0·55	0·2	±2·75	11	3·5	Cracks at 45° to applied load (Fig. 14).
0·0002 (approx.)	0·55	0·2	±3·6	34	2·7	Crack at 90° to applied load (Fig. 15).

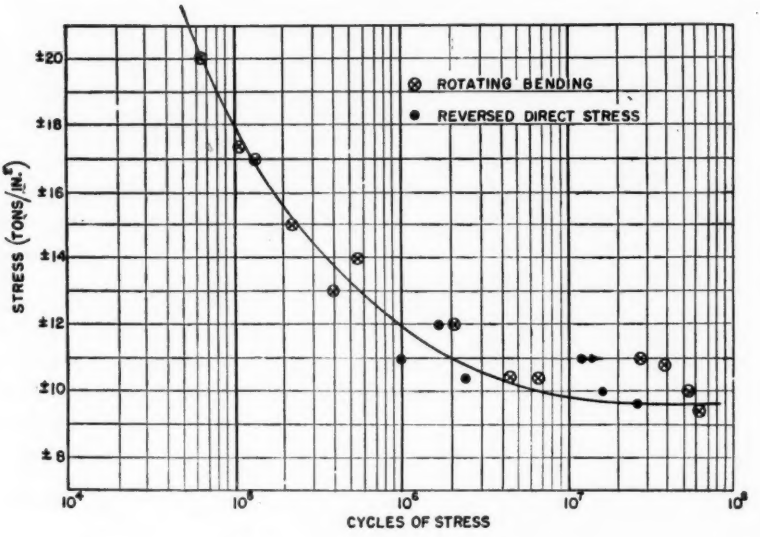

Fig. 4.

S-N curve for plain specimens of aluminium alloy.

3· Experimental Results*

3.1. Aluminium Alloy B.S. L 65

Preliminary fatigue tests under both rotating bending and reversed direct stress were done on plain specimens. The results are shown in Fig. 4. Wöhler specimens of 0·3 in. diameter were used for the rotating bending tests, and specimens 1·38 in. diameter for the reversed direct stress tests. There is little difference between the two sets of points and a common curve, giving a fatigue limit for the material of $\pm 9{\cdot}7$ tons/in.^{2} at an endurance of 50×10^6 cycles, has been drawn.

Table II gives details of the different types of notches tested under reversed direct stress and rotating bending. This table also shows the corresponding estimated fatigue limits, the values of the geometric stress concentration factor K_t and the strength reduction factor K_f, and the results of the microscopic examination of the material at the root of the notch of the unbroken specimens. A typical *S–N* curve for one particular notch shape is given in Fig. 5. K_t is obtained from Neuber's analysis[4], while K_f is the ratio of the plain fatigue limit to the notched fatigue limit. Photomicrographs of the material at the root of the notch of unbroken specimens for each type of notch are given in Figs. 6-15.

*Full experimental details are given in Ref. 18.

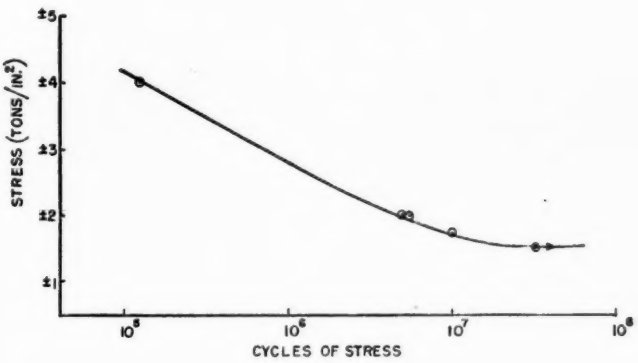

Fig. 5.
S-N curve for Vee-notched aluminium alloy specimens.
$a = 0{\cdot}65$ in. $t = 0{\cdot}2$ in. $r = 0{\cdot}008$ in.
Reversed direct stress.

3.2. Mild Steel 0·15 per cent C

The results of the preliminary fatigue tests on plain specimens are shown in Fig. 16. The conditions were similar to those of the aluminium alloy tests, except that the direct stress specimens were 0·977 in. diameter. The difference between the results obtained from the two types of loading could be explained on a stress re-distribution basis, as considered by Forrest and Tapsell[14]. The lower fatigue limit of $\pm 14{\cdot}0$ tons/in.², *i.e.* the fatigue limit for the direct stress tests, has been used as the basic fatigue limit for the material. This value agrees quite closely with that obtained by Phillips and Heywood[5] for similar material and consequently their results, where appropriate, have been included with those obtained in this paper.

Table III (p. 13) presents information corresponding to that given in Table II for the aluminium alloy. A typical *S–N* curve for a particular notch shape is shown in Fig. 17.

Photomicrographs of the material at the root of the notch of the unbroken specimens are shown in Figs. 18–22.

3.3. Nickel Chromium Steel (EN 26)

Unfortunately, material for only a few tests on this steel was available. As with the mild steel, some results obtained by Phillips and Heywood[5] for a similar steel have been included. These authors found little difference between the fatigue limits determined by rotating bending and reversed direct stress tests on plain specimens, and an average value of $\pm 36{\cdot}5$ tons/in.² has been taken from their results.

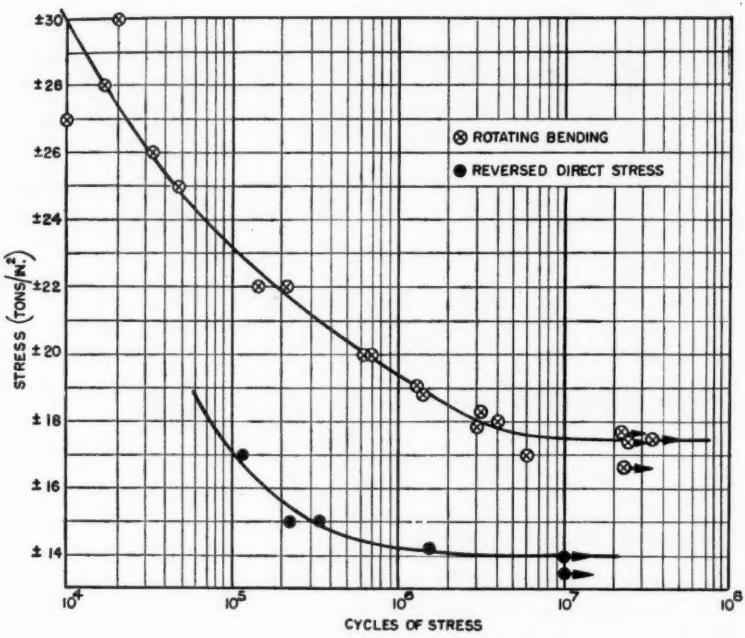

Fig. 16.
S-N curve for plain specimens of mild steel.

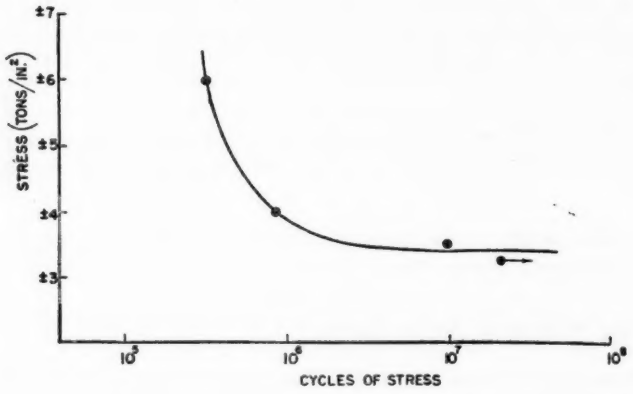

Fig. 17.
S-N curve for Vee-notched mild steel specimens.
$a = 0{\cdot}65$ in. $t = 0{\cdot}2$ in. $r = 0{\cdot}004$ in.
Reversed direct stress.

Vee-notched aluminium alloy specimens.
Reversed direct stress.

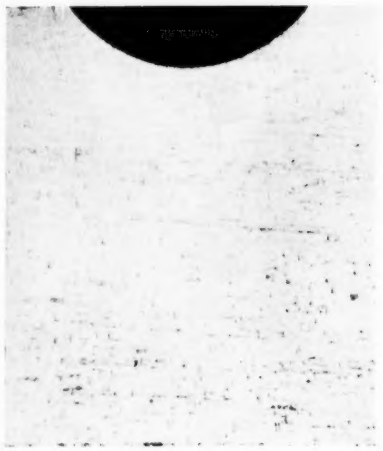

Fig. 6.
Specimen MBCG 2L × 25*
$r = 0{\cdot}05$ in.
± 3 tons/in.^{2} $27{\cdot}32 \times 10^6$ cycles unbroken.

Fig. 7.
Specimen MBCG 2G × 100
$r = 0{\cdot}02$ in.
± 2 tons/in.^{2} $31{\cdot}52 \times 10^6$ cycles unbroken.

Fig. 8.
Specimen MBCG 11N × 100
$r = 0{\cdot}008$ in.
$\pm 1{\cdot}5$ tons/in.^{2} $33{\cdot}26 \times 10^6$ cycles unbroken.

Fig. 9.
Specimen MBCG 18A × 500
$r = 0{\cdot}004$ in.
$\pm 1{\cdot}5$ tons/in.^{2} 30×10^5 cycles unbroken.

*The magnifications quoted in all the microphotographs refer to the originals. In this printed version they are about 20 per cent less.

Vee-notched aluminium alloy specimens.
Reversed direct stress.

Fig. 10.
Specimen MBCG 14M × 500
$r = 0{\cdot}002$ in.
± 2 tons/in.^{2} $28{\cdot}05 \times 10^6$ cycles unbroken.

Fig. 11.
Specimen MBHQ 3C × 500
$r = 0{\cdot}0005$ in. (approx.)
$\pm 2{\cdot}5$ tons/in.^{2} $29{\cdot}26 \times 10^6$ cycles unbroken.

Rotating bending.

Fig. 12.
Specimen MBCG 7Q1 × 100
$r = 0{\cdot}02$ in.
$\pm$ 3 tons/in.^{2} $30{\cdot}3 \times 10^6$ cycles unbroken.

Fig. 13.
Specimen MBHG 16J × 250
$r = 0{\cdot}008$ in.
± 3 tons/in.^{2} $17{\cdot}35 \times 10^6$ cycles unbroken.

Vee-notched aluminium alloy specimens.
Rotating bending.

Fig. 14.
Specimen MBCG 7L1 × 500
$r = 0{\cdot}002$ in.
$\pm 2{\cdot}75$ tons/in.^{2} $30{\cdot}05 \times 10^6$ cycles unbroken.

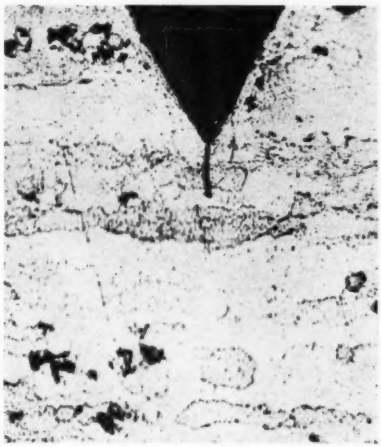

Fig. 15.
Specimen MBHQ 16F × 500
$r = 0{\cdot}0002$ in. (approx.)
$\pm 3{\cdot}25$ tons/in.^{2} $17{\cdot}16 \times 10^5$ cycles unbroken.

Vee-notched mild steel specimens.
Reversed direct stress.

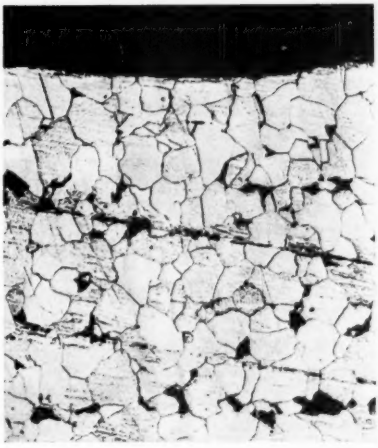

Fig. 18.
Specimen TON 4F × 200
$r = 0{\cdot}05$ in.
$\pm$ 4·25 tons/in.^{2} $10{\cdot}63 \times 10^6$ cycles unbroken.

Vee-notched mild steel specimens.
Reversed direct stress.

Fig. 19.
Specimen TON 4G × 250
$r = 0{\cdot}01$ in.
$\pm 3{\cdot}75$ tons/in.^{2} $23{\cdot}39 \times 10^5$ cycles unbroken.

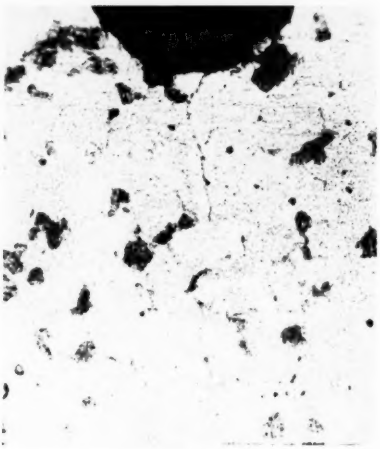

Fig. 20.
Specimen TON 4P × 250
$r = 0{\cdot}004$ in.
$\pm 3{\cdot}25$ tons/in.^{2} $20{\cdot}8 \times 10^5$ cycles unbroken.

Rotating bending

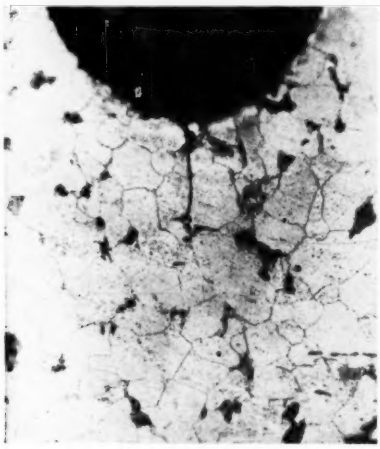

Fig. 21.
Specimen TON 1Q × 250
$r = 0{\cdot}004$ in.
± 4 tons/in.^{2} $12{\cdot}75 \times 10^5$ cycles unbroken.

Fig. 22.
$r = 0{\cdot}004$ in.
Specimen TON 3D × 250
± 5 tons/in.^{2} $15{\cdot}97 \times 10^5$ cycles unbroken.

TABLE III

VEE-NOTCHED MILD STEEL SPECIMENS

Values of Fatigue Limit, K_t, K_f

and Remarks on the Microscopic Examination of Notch Root

r (in.)	a (in.)	t (in.)	*Fatigue limit* (tons/in.²)	K_t	K_f	*Microscopic examination and photograph figure number*
			Reversed Direct Stress			
0·05	0·65	0·2	±4·25	3·3	3·3	No cracks (Fig. 18).
0·025*	0·65	0·2		4·4	3·8	No examination.
0·01	0·65	0·2	±3·75	6·6	3·7	Crack at 90° to applied load (Fig. 19).
0·004	0·65	0·2	±3·4	10	4·1	Crack at 90° to applied load (Fig. 20).
0·002*	0·65	0·2		14	3·8	Cracks present. *See* Ref. 12.
			Rotating Bending			
0·004	0·55	0·2	±4·25	8·0	3·3	Crack at 90° to applied load (Fig. 21).
0·004	0·65	0·1	±5	7·5	2·8	Crack at 90° to applied load (Fig. 22).

TABLE IV

VEE-NOTCHED NICKEL CHROMIUM STEEL SPECIMENS

Values of Fatigue Limit, K_t, K_f

and Remarks on the Microscopic Examination of Notch Root

r (in.)	a (in.)	t (in.)	*Fatigue limit* (tons/in.²)	K_t	K_f	*Microscopic examination and photograph figure number*
			Reversed Direct Stress			
0·005	0·425	0·02	±8·0	4·6	4·6	No crack detected.
0·005	0·425	0·2	±4·6	8·0	7·9	No crack detected.
			Rotating Bending			
0·004	0·55	0·2	±6·25	8·0	5·8	No crack detected.
0·010	0·55	0·2	±7·25	5·2	5·0	No crack detected.

Table IV presents information for this material corresponding to that given in Tables II and III. A typical S–N curve is shown on Fig. 23.

For the few different notches tested, no non-propagating cracks could be detected in any of the unbroken specimens. In view of this, no photomicrographs are given for this material.

4. Discussion of Results

As most results have been obtained with the aluminium alloy, these will be discussed in detail, and the mild steel and nickel chromium steel results dealt with more briefly.

* Results taken from Ref. 5.

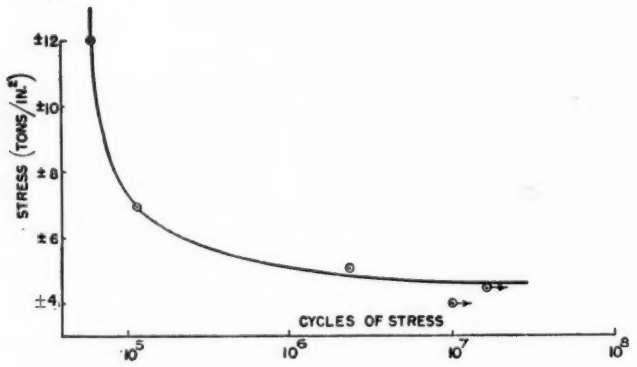

Fig. 23.
S-N curve for Vee-notched nickel chromium steel specimens.
a=0·425 in. t=0·2 in. r=0·005 in.
Reversed direct stress.

The main purpose of the experimental work was to study the formation of cracks and for this reason a wide variety of notch shapes was used. Although only relatively few specimens were tested for each individual notch shape, it is considered that the estimated fatigue limits are not seriously in error.

For the aluminium alloy a series of tests in reversed direct stress was carried out with the values of a (radius of minimum cross section) and t (notch depth) kept constant and only r (root radius) varying. Fig. 24 shows the fatigue limit plotted against root radius for these tests. The point at zero root radius is taken from results by Frost and Phillips[11] relating to cracked specimens. Although this point cannot, for several reasons, be taken as strictly comparable with the others, it accords with their general trend and certainly represents an upper limit to the true value for zero notch radius. It can be seen that the fatigue limit decreases with decreasing root radius to a root radius value of about 0·0055 in. and then increases again. As mentioned previously in Section 1, the fact that a specimen containing a notch of sharp root radius can be stronger than one with a less sharp root radius has been noted by several authors[8, 9, 10], but no completely satisfactory explanation has been put forward.

Now, considering the vertical line on Fig. 24 through the critical root radius, microscopic examination of the material at the root of the notch of unbroken specimens (*i.e.* those run at the fatigue limit or just below) with root radii greater than this value (to the right of the line) showed no breakdown of the material, as can be seen from Figs. 6, 7 and 8. However, equivalent specimens with smaller root radii (to the left of the line) were all found, on examination, to contain non-propagating cracks (*see* Figs. 9, 10, and 11). Hence the increase in fatigue strength obtained with root radii to the left of the vertical line is coincident with the formation of non-propagating cracks.

The notch shown in Fig. 11 was intended to be as sharp as possible, *i.e.* as sharp as could be machined. The resulting notch was rather irregular in profile

but, as it was obviously sharper than the next larger size, the specimens were tested as they were. For the equivalent sharp notch tested in rotating bending, a different machining technique was employed, and a much better notch was obtained (Fig. 15).

The formation of non-propagating cracks in the aluminium alloy material has been discussed previously by the author[13]. For the purpose of this paper it is sufficient to state that the cracks formed extended around the whole periphery and reached a reasonably uniform depth. With the reversed direct stress tests, this uniformity of crack growth is achieved only when the loading is truly axial.

Further work is required before a detailed explanation can be given of the causes and critical conditions necessary for a crack to remain dormant. Any explanation must involve consideration of the stress gradient generated by the notch and the variation of this stress gradient as the crack forms at the notch root. However, as no cracks were detected to the right of the line on Fig. 24, it would appear that the nominal stress has to be increased with increasing notch radius in order to initiate the crack, which then propagates automatically; while to the left of the line a non-propagating crack is formed, and the nominal stress needs to be increased with decreasing notch radius in order to cause the crack to propagate and the specimen to fail.

If, in Fig. 24, the point representing the stress necessary to initiate a crack at 0·002 in. radius[13] is plotted, it lies on a feasible continuation (as shown by the dotted line) of the curve to the right of the critical radius back to the origin. The difference between this dotted line and the full line to the left of the critical radius is the increase in nominal stress required to propagate the crack formed at the stress represented by the dotted line.

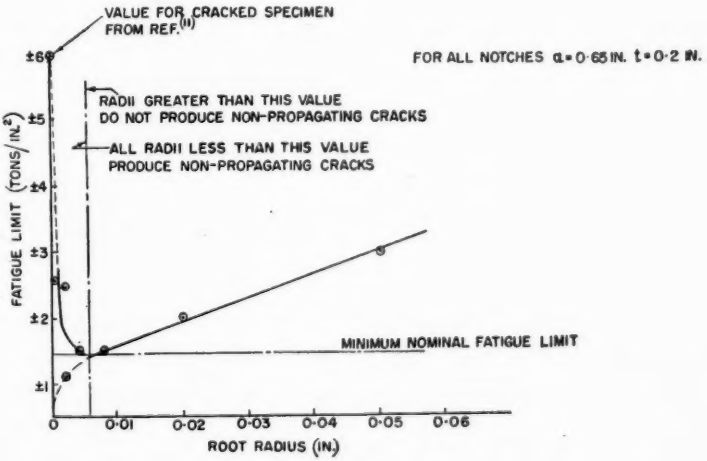

Fig. 24.
Fatigue limit of aluminium alloy Vee-notched specimens in reversed direct stress plotted against root radius. For all notches $a=0{\cdot}65$ in., $t=0{\cdot}2$ in.

All the experimental data obtained for the aluminium alloy are plotted on Fig. 25, which shows the geometric factor K_t plotted against the strength reduction factor K_f. Consider first the direct stress tests only; it can be seen that the points lie on the $K_t = K_f$ line up to a certain value of K_t, reach a maximum value of K_f, and then decrease. All unbroken specimens having a K_t value to the right of the vertical line drawn through the maximum K_f point were found to contain non-propagating cracks (Figs. 9, 10 and 11). No cracks could be detected in unbroken specimens with the K_t values lying to the left of the line (Figs. 6, 7, and 8). Hence it would appear from the direct stress tests that the value of K_f equals K_t up to a certain value of K_t; then there is a transition where K_f reaches a maximum at some critical value of K_t. Beyond this critical value of K_t non-propagating cracks form, and the value of K_f then decreases with increasing values of K_t.

Considering now the rotating bending tests, it can be seen that although the general shape of the curve is similar, the maximum K_f value is much smaller than for direct stress, although it occurs at about the same critical value of K_t. Again, unbroken specimens with K_t values to the right of the line were found to contain non-propagating cracks (*see* Figs. 14, 15) while no cracks could be detected in unbroken specimens with K_t values to the left of the line (*see* Figs. 12, 13). Also included in the curve are numerous points which are taken from the literature, the numbers adjacent to the points indicating the reference. It appears that all the points lie reasonably about the one curve, despite the fact that the tests relate to various specimen and notch sizes. It is not unreasonable to assume that the two curves tend to become asymptotic to the K_f value for a cracked specimen[11]. Although it is not suggested that the dotted horizontal line representing the cracked specimen result is strictly comparable, it can almost certainly be regarded as a lower limiting value.

It is not meant to imply that the shapes of the two curves on Fig. 25, especially to the right of the vertical line through the critical K_t value, have been precisely

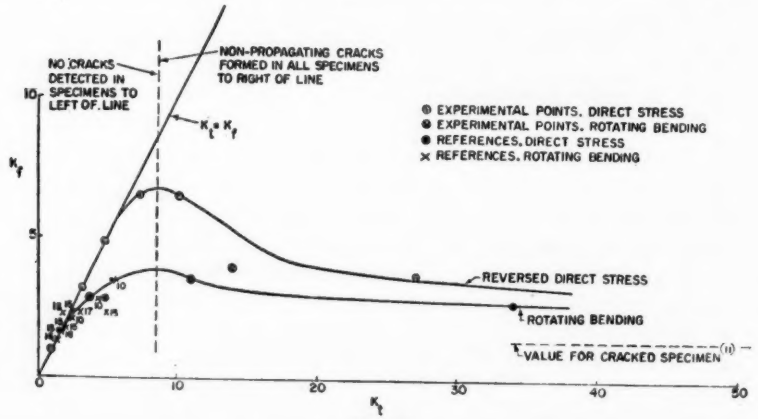

Fig. 25.
Relation between K_t and K_f for aluminium alloy.

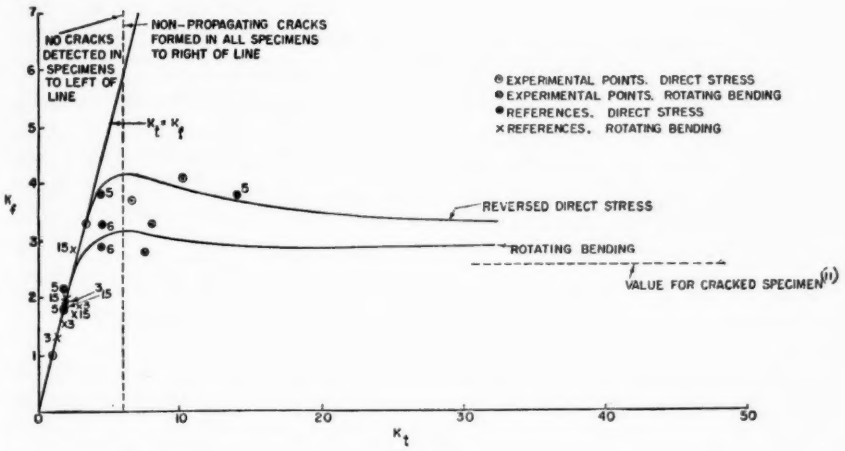
NON-PROPAGATING CRACKS FORMED IN ALL SPECIMENS TO RIGHT OF LINE
NO CRACKS DETECTED IN SPECIMENS TO LEFT OF LINE
EXPERIMENTAL POINTS. DIRECT STRESS
EXPERIMENTAL POINTS. ROTATING BENDING
REFERENCES. DIRECT STRESS
REFERENCES. ROTATING BENDING
REVERSED DIRECT STRESS
ROTATING BENDING
VALUE FOR CRACKED SPECIMEN(11)
K_f
K_t

Fig. 26.
Relation between K_t and K_f for mild steel.

determined. The position of the vertical line in Fig. 25 is reasonably well defined, but to the right of this the curves as drawn must be regarded merely as indicative of general trends. Investigation of this portion of the curve in detail would involve considerable difficulties in specimen preparation, because of the small root radii required.

Figure 26 shows K_f plotted against K_t for the mild steel specimens. Again two separate curves are obtained, one for reversed direct stress and one for rotating bending. The value of K_t corresponding to the maximum K_f values appears to be the same for both methods of test. As for the aluminium alloy, all unbroken specimens with a K_t value greater than the critical value were found to contain non-propagating cracks, whether tested in reversed direct stress (Figs. 19, 20 and Ref. 12), or rotating bending (Figs. 21 and 22), and no cracks could be found in unbroken specimens with a K_t value less than the critical value (Fig. 18).

Again the curves to the right of the critical K_t value can only be considered as showing general trends. For the mild steel it appears that, above the critical value of K_t, the value of K_f may remain constant. It certainly does not decrease as markedly as was found with the aluminium alloy. The horizontal line representing the K_f of the cracked specimen[11] relates to the direct stress value, and again can only be regarded as a lower limiting value.

Table V gives the critical values of K_t obtained for the three materials and the corresponding maximum K_f values, together with the limiting $K_f = K_t$ values.

Although insufficient experimental results are available to plot K_t against K_f for the nickel chromium steel, the results obtained when supplemented by data from Refs. 3 and 5 make it possible to give the approximate values included in Table V. These values show the differences between the two types of steel; for

TABLE V

CRITICAL VALUE OF K_t AND CORRESPONDING VALUES OF K_f

	Aluminium alloy	*Mild steel*	*Nickel chromium steel*	*Type of loading*
Critical value of K_t	8·5	6	11	Direct stress and rotating bending
Maximum value of K_f corresponding to above K_t value	6·5	4·25	9	Direct stress
	4	3·25	6·5	Rotating bending
Limiting value of $K_t = K_f$*	5·5	3·5	8	Direct stress
	2	2·5	5	Rotating bending

instance, with the nickel chromium steel in reversed direct stress the limiting $K_t = K_f$ value is 8, which is more than twice the corresponding value for the mild steel.

Hence it can be concluded that within the range of experimental conditions:—

(*a*) The strength reduction factor K_f equals the geometric factor K_t up to some limiting value of K_t. This limiting value of K_t ($= K_f$) varies with the material and the type of fatigue stressing employed (direct stress or rotating bending).

(*b*) The value of K_f reaches a maximum at some critical value of K_t. This is again different for different materials, but the critical value of K_t appears to be the same for direct stress and for rotating bending, although the corresponding maximum value of K_f is greater for reversed direct stress than for rotating bending.

(*c*) Below the critical value of K_t, non-propagating cracks could not be detected. However, for notches with a K_t value above the critical value, non-propagating cracks were always formed in all materials and for both methods of testing. Although photographs in this paper are only given for cracks formed at stresses just below the fatigue limit, non-propagating cracks can be formed at much lower stresses, as mentioned in Refs. 12 and 13.

(*d*) Experimental points taken from other published work show general agreement with the present results.

5. Discussion on the Relation Between K_t and K_f

It has been shown that at a certain critical value of K_t a non-propagating crack can form at the bottom of the notch. The shape of the curves in Figs. 25 and 26 suggests that the relationship between K_t and K_f to the left of the line marking the critical K_t value is completely different from that existing to the right of the line.

* Above this value $K_f < K_t$

The possibility that there may be two separate parts to this relationship has been overlooked by many investigators.

It is suggested that this discontinuity is due to the formation of non-propagating cracks. Below the critical K_t value, the relation between K_t and K_f depends on the stress necessary to initiate a fatigue crack; the nominal stress at the fatigue limit is that necessary to initiate the crack, the propagation being automatic. Above the critical value, a crack will form at a nominal stress below the fatigue limit; and the nominal stress at the fatigue limit of the specimen is that which is necessary to propagate the crack.

It is therefore improbable that a universal relationship between K_t and K_f exists.

Although in Table V a limiting $K_t = K_f$ value is given, it is not implied that below this value K_f always equals K_t. Size effect and invalidity of the maximum principal stress criterion of failure will tend to make K_f less than K_t. The accuracy of the fatigue limit determinations due to testing only a few specimens at each K_t value is insufficient to resolve these points in the present work.

6. Conclusions

The following conclusions apply only in the case of completely reversed loading, *i.e.* zero mean load.

(*i*) Non-propagating cracks can form at the root of notched fatigue specimens when a critical value of the geometric stress concentration factor K_t is exceeded This value varies for different materials.

(*ii*) Because of the formation of these cracks it is suggested that there are two distinct parts to the relationship between K_t and K_f. Below the critical K_t value, the nominal stress at the fatigue limit is that necessary to initiate the crack, propagation then being automatic; above the critical K_t value, a crack will form at a nominal stress below the fatigue limit, the applied nominal stress at the fatigue limit being that necessary to propagate the crack.

(*iii*) At the critical value of K_t the strength reduction factor K_f reaches a maximum value. While the critical value of K_t is the same for both rotating bending and reversed direct stress, the corresponding values of K_f may be different.

(*iv*) For values of K_t above the critical value, the value of K_f does not increase and may tend to decrease with further increase in K_t.

(*v*) In practice, the increase in strength of specimens containing sharp notches which occurs when a non-propagating crack is present may not be realised, because the component will be subject to additional loadings, such as superimposed mean tensile loads, impact effects, and so on.

ACKNOWLEDGMENTS

The author acknowledges the assistance of Mr. J. Tait with the metallurgical work and also the interest and help of Mr. C. E. Phillips, Head of the Mechanics

and Materials Division. The work described has been done as part of the research programme of the Mechanical Engineering Research Board of the Department of Scientific and Industrial Research. The paper is published by permission of the Director of Mechanical Engineering Research.

REFERENCES

1. PETERSON, R. E. *Stress Concentration Design Factors.* John Wiley, New York, 1954.
2. YEN, C. S. and DOLAN, T. J. A Critical Review of the Criteria for Notch Sensitivity in Fatigue of Metals. University of Illinois Engineering Experimental Station Bulletin Series No. 398, 1952.
3. KUHN, P. and HARDRATH, H. F. An Engineering Method for Estimating Notch Size Effect on Steel. N.A.C.A. T.N. 2805, October 1952.
4. NEUBER, H. *Theory of Notch Stresses.* Published by J. S. Edwards, Ann Arbor, Michigan, 1946.
5. PHILLIPS, C. E. and HEYWOOD, R. B. The Size Effect in Fatigue of Plain and Notched Steel Specimens Loaded under Reversed Direct Stress. *Proceedings of the Institution of Mechanical Enginers,* Vol. 165, p. 113, 1951.
6. HIKATA, A. The Size Effect in Fatigue of Notch Steel Specimens Loaded under Reversed Direct Stress. Government Mechanical Laboratory Bulletin No. 2, Tokio, 1954.
7. DOLAN, T. J. and HANLEY, B. C. The Effect of Size of Specimen on the Fatigue Strength of S.A.E. 4340 Steel. University of Illinois Engineering Experimental Station, May 1948.
8. HYLER, W. S., LEWIS, R. A. and GROVER, H. J. Experimental Investigation of Notch Size Effects on Rotating Beam Fatigue Behaviour of 75S-T6 Aluminium Alloy. N.A.C.A. T.N. 3291, November 1954.
9. ROS, M. and EICHINGER, A. The Fracture Danger of Solid Bodies under Repeated Stress Fatigue. (In German). Report No. 173, Eidgenössische Material Prüfungs-Industrie und Versuchsanstalt, Zürich, September 1950.
10. MANN, J. Y. Effect of Stress Concentrations on the Fatigue Resistance of 24 ST Aluminium Alloy. Aeronautical Research Laboratory Report S.M.217. Department of Supply, Australia, November 1953.
11. FROST, N. E. and PHILLIPS, C. E. The Fatigue Strength of Specimens containing Cracks. *Proceedings of the Institution of Mechanical Engineers,* Vol. 170, No. 21, 1956.
12. FENNER, A. J., OWEN, N. B. and PHILLIPS, C. E. A Note on the Fatigue Crack regarded as a Stress Raiser. *Engineering,* Vol. 171, p. 637, 1951.
13. FROST, N. E. Crack Formation and Stress Concentration Effects in Direct Stress Fatigue. *Engineer,* Vol. 200, pp. 464 and 501, 1955.
14. FORREST, P. G. and TAPSELL, H. J. Correlation of Fatigue Strength in Bending and Direct Stress. *Engineering,* Vol. 173, p. 757, 1952.
15. GROVER, H. J. Fatigue Notch-Sensitivities of some Aircraft Materials. *Proceedings of the American Society for Testing Materials,* Vol. 50, p. 717, 1950.
16. BENNETT, J. A. and WEINBERG, J. G. Fatigue Notch Sensitivity of Some Aluminium Alloys. *Journal of Research,* National Bureau of Standards, Vol. 52, No. 5, p. 235, 1954.
17. SPRETNAK, J. W., FONTANA, M. G. and BROOKS, H. E. Notched and Unnotched Tensile and Fatigue Properties of Ten Engineering Alloys at 25°C. and −196°C. *Transactions of the American Society of Metals,* Vol. 43 p. 547, 1951.
18. FROST, N. E. Mechanical Engineering Laboratory Report PM 184, October 1955.

Some Exploratory Three-Dimensional Jet-Flap Experiments

J. WILLIAMS and A. J. ALEXANDER

(*National Physical Laboratory, Teddington*)

SUMMARY: This paper describes a first attempt to establish the order of magnitude of finite aspect ratio effects for jet-flap wings. Lift, pitching moment, and drag results are presented from pressure-plotting measurements on a jet-flap model of aspect ratio slightly less than three. These experiments were complementary to two-dimensional tests carried out at the National Gas Turbine Establishment.

1. Introduction

The development of the jet-flap scheme at the National Gas Turbine Establishment has already been discussed by Davidson[1]. The basic theoretical concepts and the early two-dimensional experiments have been described by Stratford[2] and Dimmock[3] respectively. In association with these researches, three-dimensional wind-tunnel tests were carried out at the N.P.L., to obtain quickly a first idea of the magnitude of finite aspect ratio effects for jet-flap wings.

A small pressure-plotting model of rectangular plan form, with a 12½ per cent thick elliptic section and a jet angle of 31·3°, was mounted with a plate at one end to give an effective aspect ratio slightly less than three. The lift, pitching moment and thrust forces were evaluated from measurements of the surface static pressures and the jet reaction. These tests were directly complementary to the N.G.T.E. two-dimensional tests[3], in that the models were essentially of the same shape, size and general construction.

The present paper, after outlining the experimental arrangement used in the N.P.L. three-dimensional tests, mainly describes the force results obtained on the wing. Details of the wing-section pressure distributions and of the general flow characteristics are described elsewhere[4].

NOTATION

a_0 slope of two-dimensional lift-incidence curve

A wing aspect ratio

c wing chord

Received November 1956.

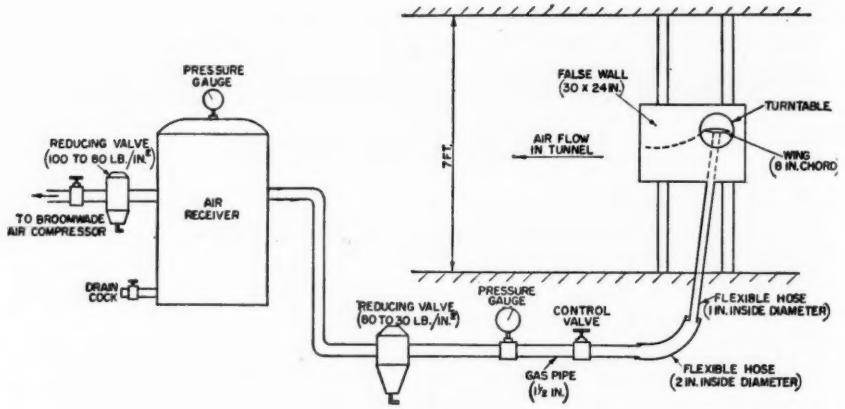

Fig. 1.

Arrangement of the jet flap model and external ducting.

C_{Lp}, C_{mp}, C_{Dp} pressure lift, pitching moment and drag coefficients, (about mid-chord); derived by integration of pressure forces on wing surface

C_L, C_m, C_T total lift, pitching moment and thrust coefficients, (about mid-chord); derived by adding direct jet reaction components and pressure forces on wing. (*See* Section 2.3)

C_J jet reaction coefficient $= J/(\frac{1}{2}\rho_0 U_0^2 S)$

e aspect ratio efficiency factor

J jet reaction at nozzle

p_0, ρ_0, U_0 main stream pressure, density and speed

p_D duct stagnation pressure

R main stream Reynolds number based on wing chord

s span of wing (excluding small ellipsoidal tip)

S area of wing plan form (excluding small ellipsoidal tip)

w width of jet nozzle

α wing incidence relative to main stream

θ jet exit angle relative to wing chord line.

2. Experimental Method

2.1. Model and Test Set-up

The model was of 8 in. chord and 12 in. span, with a small ellipsoidal tip fairing which added a further 0·25 in. to the span and 1½ per cent to the wing area. It was mounted centrally in a near-circular tunnel of 7 ft. diameter so that tunnel interference effects were negligible. The general arrangement of the model in the tunnel, and of the external ducting to the compressor unit, is illustrated in Fig. 1;

a turn-table attached to the model root rotated in a fixed end-plate as shown. Mainly because of structural and accessibility considerations, the end-plate size was limited to one chord height vertically above the zero incidence chord line and two chords below, to 0·8 chord upstream of the wing leading edge and two chords downstream of the trailing edge (jet exit). According to Mangler's end-plate theory[5], the effective aspect ratio of the wing was then about 2·75, for the ratio (aerofoil span)/(end-plate height) equal to $\frac{1}{2}$. This effective aspect ratio is only slightly less than the value 3 which would have been obtained with an infinite end-plate.

The chordwise pressure distribution was measured at each of the four spanwise stations, 0·2s, 0·5s, 0·8s and 0·95s from the wing root, by about 26 static pressure tappings—most closely spaced near the leading edge and the trailing edge. The blowing slot was located at the trailing edge, and had a mean width $w=0{\cdot}025$ in. ($w/c=0{\cdot}003$), with a spanwise variation of less than 0·0025 in.

At zero main stream speed, the jet emerged at an angle of 31·3° to the chord line for the whole range of jet total pressures p_D measured in the model duct (up to two atmospheres absolute). The jet reaction J was determined by the N.G.T.E., in terms of p_D, from thrust balance measurements at zero main stream speed; a correction was applied to allow for the surface pressure drag arising on the model as a result of the flow induced by the jet efflux.

2.2. Range of Experiments

Experiments covering the incidence range $-5°$ to 20° were mostly at a wind speed of 100 ft./sec. ($R=0{\cdot}4\times10^6$), when the available air supply permitted values of the jet reaction coefficient C_J ($=J/(\frac{1}{2}\rho_0 U_0^2 S)$) up to 0·5. Higher C_J-values were obtained by reducing the wind speed to 50 ft./sec. ($C_J<2{\cdot}1$). For a few tests, at zero incidence only, the speed was reduced still further to 30 ft./sec. giving C_J-values up to 4·8. Transition wires were located on the upper and lower surfaces of the model at 0·2c behind the leading edge, as far forward as possible without causing interference at the closely spaced static holes in the wing nose. Except at very low C_J-values, the results were not significantly altered by removal of the transition wires.

2.3. Determination of Force Coefficients

The sectional "pressure-force" coefficients were evaluated by chordwise integration of the surface static pressures at each spanwise station. Some simplifying assumptions were necessary close to the trailing edge, since there were no static holes inside the slot throat. The resulting error in lift is negligible, but this may not be so for the pitching moment and drag under all conditions. The wing pressure-force coefficients C_{Lp}, C_{mp} and C_{Dp} were finally determined by spanwise integration of the sectional pressure forces.

The total force on the wing was derived by adding the jet reaction at the nozzle to the pressure force on the wing arising from the main stream flow over the aerofoil surface.

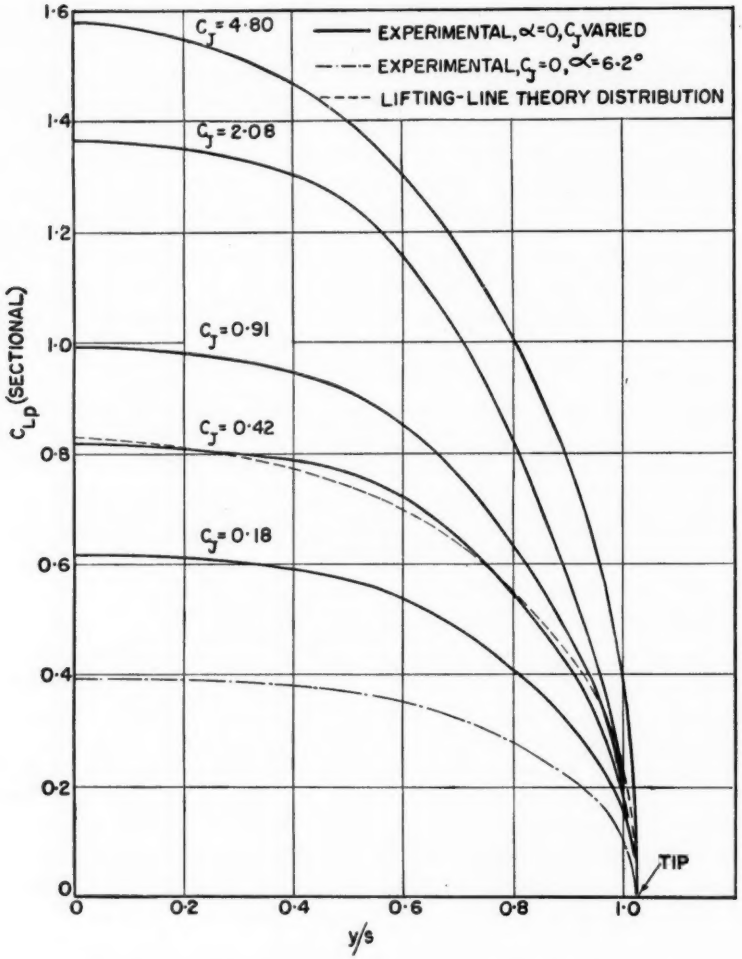

Fig. 2.
Spanwise distribution of pressure lift at zero incidence. Variation with C_J.

Thus, the overall lift, pitching moment, and thrust coefficients are written as

$$\left.\begin{aligned} C_L &= C_J \sin(\theta+\alpha) + C_{Lp} \\ C_m &= -\frac{n}{c} C_J + C_{mp} \\ C_T &= C_J \cos(\theta+\alpha) - C_{Dp} \end{aligned}\right\} \quad . \quad . \quad . \quad . \quad . \quad (1)$$

The symbol n here denotes the perpendicular distance, from the point about which moments are taken, on to the extended centre line of the jet exit; for moments about mid-chord, as in the present tests, $n/c = \frac{1}{2}\sin\theta$.

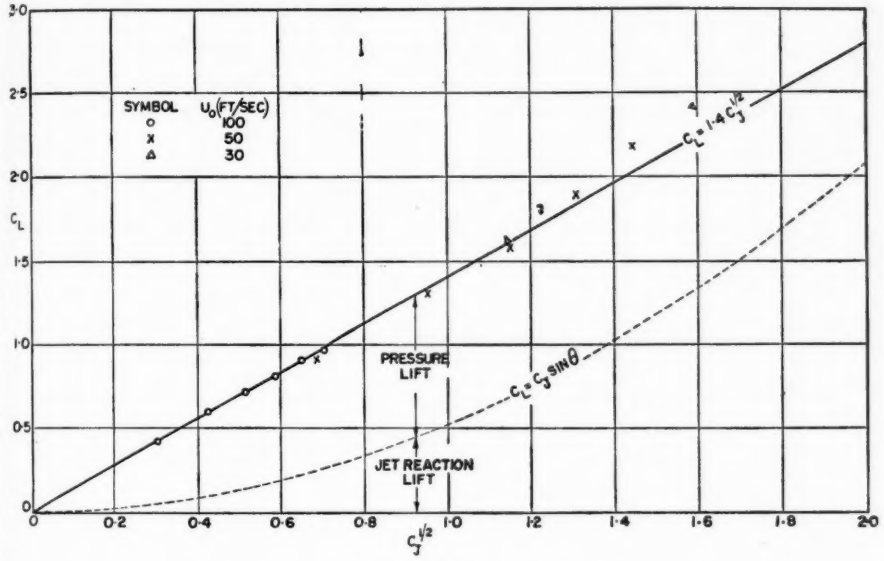

Fig. 3.
Variation of total lift C_L with $C_J^{\frac{1}{2}}$ at zero incidence.

3. Experimental Results

In order to assess quickly the importance of finite aspect ratio effects on jet-flap wings, the experimental results on the present wing, of aspect ratio 2·75, are discussed in terms of simple aspect ratio considerations for conventional wings (without blowing) at incidence.

3.1. Lift

The spanwise distribution of the pressure-lift loading induced by blowing from the trailing edge, with the wing at zero incidence, is little different from that given by simple lifting-line theory for the plan form, or by experimental distributions for the wing at incidence without blowing (*see* Fig. 2).

The total lift coefficient C_L at zero incidence is plotted in Fig. 3 against $C_J^{\frac{1}{2}}$. At C_J-values below unity, the experimental results satisfy approximately the relation

$$C_L = 1{\cdot}4\,C_J^{\frac{1}{2}} \quad . \quad . \quad . \quad . \quad . \quad . \quad (2)$$

and are about 0·6 of the corresponding N.G.T.E. two-dimensional values. The appropriate value of the aspect-ratio correction factor $[1+(a_0/(\pi Ae))]^{-1}$ for lift on conventional wings is 0·58, assuming ideal elliptic loading ($e=1$) and a sectional lift-curve slope a_0 of 2π. At higher C_J-values and incidences (below the stall), the rate of increase of C_L with $C_J^{\frac{1}{2}}$ tends to rise slightly. When $C_J > 2$, the jet reaction contribution to the total lift exceeds the pressure-lift contribution.

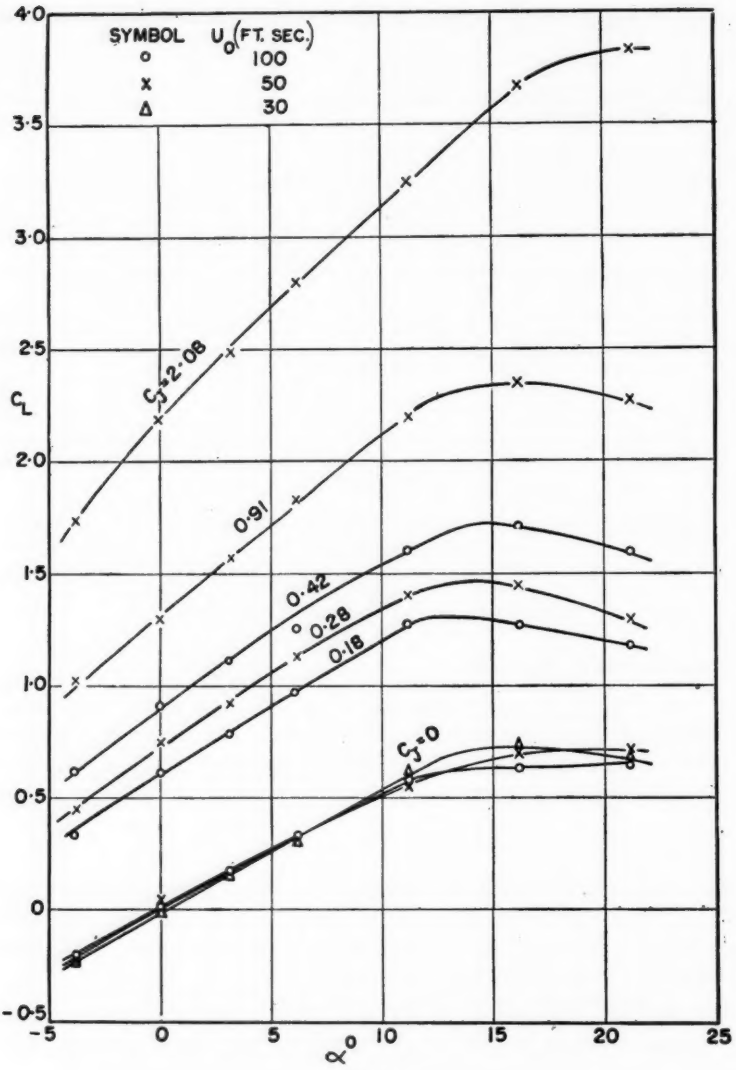

Fig. 4.
Variation of total lift with incidence at constant C_J.

Lift-incidence curves for a range of C_J-values up to 2·1 are shown in Fig. 4. The measured $dC_L/d\alpha$, at constant C_J and small incidences, increases from 0·055/degree without blowing to about 0·1/degree when $C_J=2$. The increase is roughly proportional to $C_J^{\frac{1}{2}}$ and comprises contributions from both the jet reaction and pressure-force components. If α is small and measured in degrees, equation (1) with $\theta=31·3°$ gives $dC_L/d\alpha \simeq 0·015\,C_J + dC_{L_p}/d\alpha$.

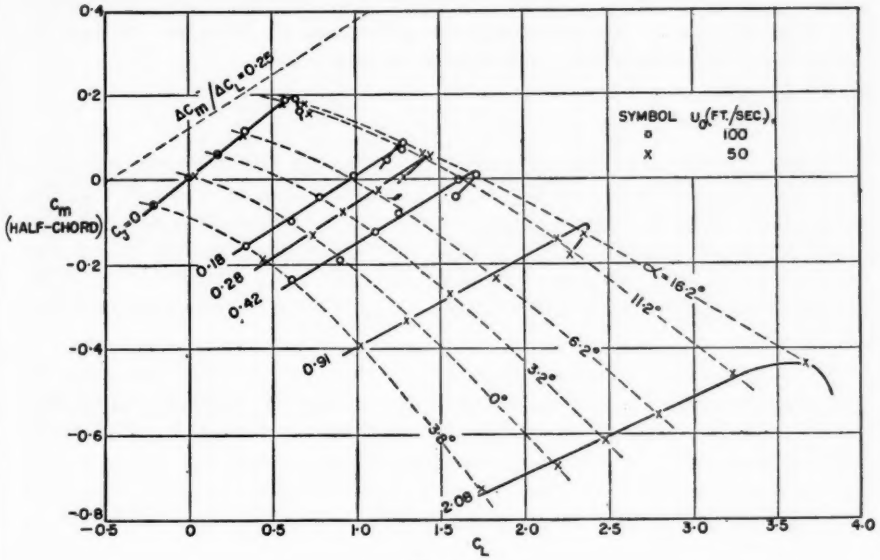

Fig. 5.
Variation of total pitching moment with total lift.

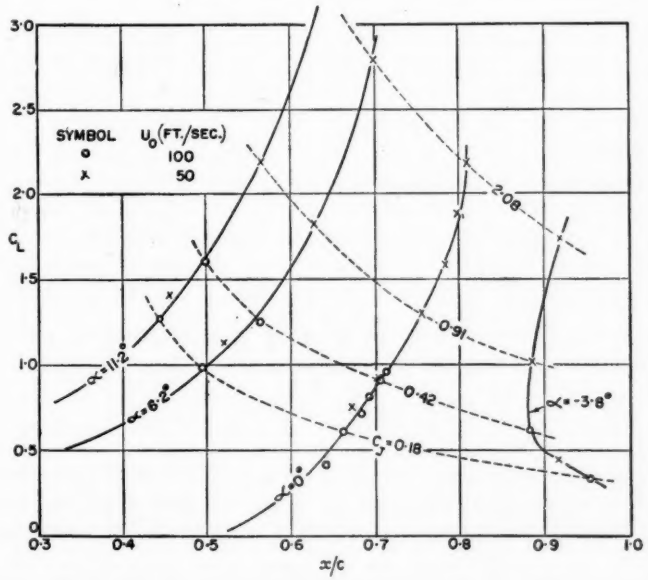

Fig. 6.
Variation in position of centre of total lift.

There is no significant loss in stalling incidence as C_J is increased from zero, and at C_J-values above unity there is even some improvement. However, this may be peculiar to the particular wing configuration of these tests.

3.2. Pitching Moments

The total pitching moment C_m about the mid-chord axis is plotted against the corresponding total lift C_L in Fig. 5, for prescribed values of α and of C_J. The mean slope (dC_m/dC_L) of the curves for constant C_J (α varied) is about 0·25 at low but non-zero values of C_J*, so that the aerodynamic centre is then located close to the quarter-chord position. The slope decreases as C_J increases, so that the aerodynamic centre tends to move further aft, by about $0{\cdot}04c$ as C_J is raised from 0·2 to unity.

As C_J is increased with α constant, or α is decreased with C_J constant, the nose-down value of C_m becomes steadily larger, so that the centre of total lift then moves rearward. Fig. 6 shows that this chordwise movement, away from the mid-chord position for $\alpha=0$ and C_J small, is quite appreciable.

3.3. Total Thrust and Pressure Drag

Values for the total thrust coefficient C_T on the wing can be determined, as in Fig. 7, by subtracting the measured pressure drag C_{Dp} on the aerofoil surface from the corresponding component $C_J \cos(\theta+\alpha)$ of the jet reaction. This does not, of course, include the skin-friction drag.

Now, for two-dimensional inviscid flow in the main stream and the jet, $C_T=C_J$; thus, in addition to the direct jet reaction component $C_J \cos(\theta+\alpha)$, a recovery of thrust $C_J\{1-\cos(\theta+\alpha)\}$ should theoretically be manifest in the pressure distribution over the aerofoil surface. The pressure drag measured in these three-dimensional experiments may therefore be regarded as comprising a section form drag, and an induced drag resulting from downwash effects at the wing less any thrust recovery which might arise. Because of the low aspect ratio and jet angle, the combined form and induced-drag contributions completely outweigh any thrust recovery (*see* Fig. 7). Moreover, with the present simple wing section and jet nozzle shapes, the recovery of thrust is probably small in practice[3].

The measured pressure drag on the wing at zero incidence, with $C_J < 0{\cdot}5$, satisfies approximately the relation

$$C_{Dp}=0{\cdot}013+0{\cdot}14\,C_{Lp}^2, \quad . \quad . \quad . \quad . \quad . \quad (3)$$

while for C_J-values up to 2, C_{Dp} does not exceed $0{\cdot}013+0{\cdot}16\,C_{Lp}^2$ (*see* Fig. 8). An analysis of data for higher incidences up to the stall gives much the same result. The corresponding induced (pressure) drag $C_{Lp}^2/(\pi Ae)$ for a conventional wing

*The unusual slope obtained for dC_m/dC_L without blowing is ascribed to the unconventional trailing-edge shape and low Reynolds numbers of the tests. With a small amount of blowing, sufficient to clean up the flow near the trailing edge, the more usual value of 0·25 was found.

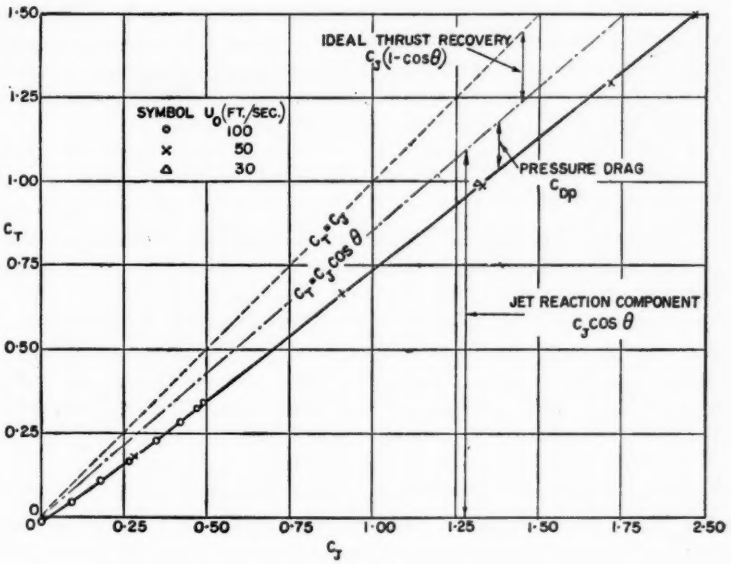

Fig. 7.

Variation of total thrust C_T with C_J at zero incidence.

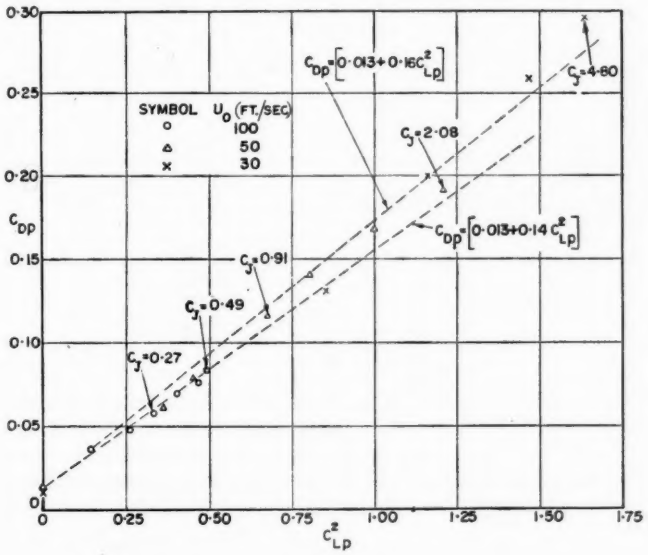

Fig. 8.

Variation of pressure drag C_{Dp} with C_{Lp}^2 at zero incidence.

producing the lift C_{L_P} is $0{\cdot}116\ C_{L_P}{}^2$, assuming elliptic loading ($e=1$). The difference $0{\cdot}013+0{\cdot}02\ C_{L_P}{}^2$ from the value given by equation (3) could reasonably be accounted for as sectional form drag in the experiments. In any case, it seems that the pressure drag on a jet-flap wing is closer to that of a conventional wing producing the same *pressure lift* rather than the same *total lift*.

4. Concluding Remarks

The experimental results for this wing of aspect ratio 2·75 demonstrate the order of magnitude of finite aspect ratio effects on jet-flap wings and can usefully be reviewed in the light of simple aspect ratio correction factors for conventional wings at incidence (without blowing). Some supplementary experiments[4], with the aspect ratio of the jet-flap wing increased to nearly 7, also lend support to the comparisons made in Section 3. However, the present tunnel tests were not designed to establish basic principles for a three-dimensional jet-flap theory, nor to resolve fundamental downwash considerations*. For this reason, and to provide more comprehensive data for project work, further experiments are to be made at the N.P.L. on a larger-scale model with variable aspect ratio and jet angle. The forces will be determined both by three-component balance measurements and by pressure-plotting. The three-dimensional nature of the flow over the wing and in the wake will also be explored.

Acknowledgments

The work described in this paper was done in the Aerodynamics Division of the National Physical Laboratory, and is published on the recommendation of the Aeronautical Research Council and by permission of the Director of the Laboratory.

References

1. Davidson, I. M. The Jet Flap. *Journal of the Royal Aeronautical Society*, January 1956.
2. Stratford, B. S. Early Thoughts on the Jet Flap. *The Aeronautical Quarterly*, Vol. VII, pp. 45-59, February 1956.
3. Dimmock, N. A. An Experimental Introduction to the Jet Flap. National Gas Turbine Establishment Report R.175, July 1955. (To be published in the A.R.C. Current Paper Series.)
4. Williams, J. and Alexander, A. J. Three-Dimensional Wind-Tunnel Tests of a 30° Jet Flap Model. A.R.C. Current Paper 304, November 1955.
5. Mangler, W. Die Auftriebsverteilung am Tragflügel mit Endscheiben. *Luftfahrtforschung*, Vol. 14, p. 564, 1937.

*Some preliminary remarks on possible fundamental postulates are made in Ref. 4, but these are largely superseded by more recent theoretical studies at the Royal Aircraft Establishment, Farnborough.

The Aiming Problem in Aerial Gunnery

M. HANCOCK, A.R.C.S., B.Sc.

(*Royal Aircraft Establishment*)

SUMMARY: The aiming problem in aerial gunnery has formerly been analysed by approximate methods which allow results of sufficient accuracy for practical requirements to be obtained from a very simple mathematical treatment. There has therefore been no practical demand for any more elaborate analysis, although the development of a more exact treatment of the problem is not without interest from the academic point of view. In this paper a more complete analysis is developed in a form which is generally applicable to a broader class of aiming problems. The relevant parts of the standard external ballistic analysis for projectiles fired from guns are also included for the sake of completeness, and the earlier simplified analysis of the aiming problem is also presented to allow comparison of the results with those of the more complete analysis. Finally, a section on the gunner's view of the aiming problem is included, to provide an explanation of certain difficulties which frequently arise through neglect of the important differences between the points of view of an observer moving with the gun and an observer at rest in the air.

1. Introduction

It is well known that in aerial gunnery the gun must generally be pointed slightly away from the line joining it directly to the target to obtain a hit, the angle by which it is turned away being called the "lead angle". The exact calculation of the lead angle in the great variety of circumstances which can arise in air combat is a matter of considerable complexity, and no complete analytical treatment of the problem has been published previously. From the point of view of those concerned with the design or use of aircraft gunsighting systems this is not a serious matter, as analytical results of adequate accuracy for all practical requirements can readily be obtained by treating the problem in a number of separate parts which are regarded as independent, although they are in fact interdependent to some extent.

It is of some interest, however, to examine the problem analytically as a single entity instead of in separate supposedly independent parts, and this paper presents the results of such an analysis. In this new analysis simplifying assumptions equivalent to supposing the action to take place over a flat earth in an atmosphere of uniform density free from velocity gradients are still retained, but these conditions are so nearly satisfied in actual combat that their introduction introduces errors of extremely small significance.

Received August 1955.

NOTATION*

V_G speed of the gunner's aircraft along G_0V at the moment the shot is fired

(l_G, m_G, n_G) direction cosines of G_0V

V_M muzzle velocity of the projectile

R target range G_0T_0 at the moment the shot is fired

$\dot{R}$ rate of change of R

(l_R, m_R, n_R) direction cosines of the sight line G_0T_0

θ the angle T_0G_0V between the line of sight and the gunner's line of motion

ω angular velocity of the line of sight. Orthogonal components of ω denoted by ω_1, ω_2, and ω_1', ω_2', are also required

(l_M, m_M, n_M) direction cosines of the gun line G_0G_1

ψ the angle G_1G_0V between the gun line G_0G_1 and the gunner's line of motion G_0V

α the lead angle $T_0G_0G_1$. Orthogonal components of α denoted by α_1, α_2 and α_1', α_2' are also required

V_0 initial velocity of the shot along G_0N

t time of flight of the projectile from G_0 to T_1

d_1, d_2, d_3 the distances G_0N, NM and MT, respectively

$\delta x, \delta y, \delta z$ the projections of $T_1'T_1$ on OX, OY and OZ respectively

δ magnitude of yaw angle

ϕ orientation of the plane of yaw relative to an arbitrary reference plane

δ_0, ϕ_0 initial values of δ and ϕ

σ a constant defined in Section 4.3

p_1, p_2, q_1, q_2 functions defined in Section 4.3

$i = \sqrt{(-1)}$.

2. General Description of the Analysis

The analytical treatment of the aiming problem falls into two parts which are examined separately initially, although the results of the two parts must ultimately be combined. These two parts are (*i*) the Kinematic part, in which the geometrical relationships are examined, and (*ii*) the Ballistic part, in which the dynamic aspects of the projectile motion are examined. The new analysis presented in this paper is confined to the kinematic part of the problem, and this is presented first. The ballistic part of the problem has already been fully discussed in several places[1, 2, 3, 4]

* Some duplication of symbols occurs between the notation used in the discussion of the kinematic aspects of the problem and that used in the discussion of the ballistic aspects of the problem, but no danger of confusion is introduced by this.

and the results, in so far as they are relevant to the present paper, are quoted with a minimum of discussion. The simplified analysis referred to in Section 1 is then presented for comparison with the new analysis, and finally a short description of the aiming problem as the gunner sees it is added.

3. The Kinematic Aspects of the Problem

3.1. The General Problem

The kinematic analysis is completely general, and is applicable to the release of projectiles of any type, including rockets and bombs from aircraft in flight, so long as the trajectory elements of the projectile can be expressed in the form required. The analysis is referred to the general air combat situation illustrated isometrically in Fig. 1, where GG_0G represents the path of the gunner's aircraft and T_0TT_1 that of the target. A correctly aimed shot fired by the gunner from G_0 when the target is at T_0 hits the target at T_1, the direction of the gun line required to achieve this being G_0G_1. The gunner's line of sight to the target at the moment the shot is fired is G_0T_0, and his direction of motion at the same instant is G_0V. The lead angle is thus $T_0G_0G_1$, and the initial direction of motion of the shot through the air resulting from its muzzle velocity along G_0G_1 and the gunner's own velocity along G_0V is along G_0N. The trajectory of the projectile is G_0ST_1 which lies close to, but generally not exactly in, the vertical plane through G_0N. The displacement of the shot between G_0 and T_1 can be resolved into the three rectilinear components, G_0N along its original direction of motion, NM at right angles to the vertical plane through G_0N, and MT_1 vertically. The direction of motion of the target at the moment the shot is fired along T_0T_1', tangential to T_0TT_1 at T_0, while the distance T_0T_1' represents the target displacement during the time of flight of the shot due to the velocity of the target at T_0. The distance $T_1'T_1$ represents the component of total target displacement due to changes in target velocity between T_0 and T_1.

The analysis is referred to non-rotating three-dimensional right-handed co-ordinate axes with G_0 at the origin, OZ vertical, and OX and OY horizontal.

3.2. The Kinematic Analysis. First Part

The kinematic analysis is carried out in two separate parts. In the first part three auxiliary construction lines are required in Fig. 1. The first of these, shown as G_0P, is located in the plane T_0G_0V in such a position that the plane G_1G_0P is

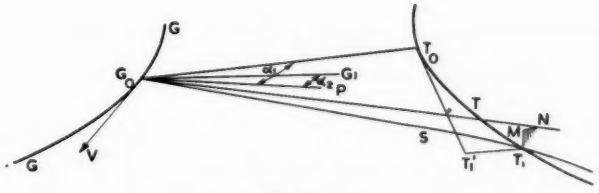

Fig. 1.
The general air combat situation.

perpendicular to T_0G_0V. The lead angle $T_0G_0G_1$ can thus be measured in terms of the two orthogonal components T_0G_0P and G_1G_0P denoted by α_1 and α_2 respectively. The second auxiliary line N_1 is normal to T_0G_0V and the third N_2 is normal to N_1 and to G_0T_0. These two normals are not shown in Fig. 1. They have direction cosines (l_1, m_1, n_1) and (l_2, m_2, n_2) respectively, defined as follows:—

$$\left.\begin{aligned} l_1 &= (m_G n_R - m_R n_G)\ \text{cosec}\ \theta \\ m_1 &= (n_G l_R - n_R l_G)\ \text{cosec}\ \theta \\ n_1 &= (l_G m_R - l_R m_G)\ \text{cosec}\ \theta \end{aligned}\right\} \quad . \quad . \quad . \quad . \quad (1)$$

$$\left.\begin{aligned} l_2 &= (l_G - l_R \cos\theta)\ \text{cosec}\ \theta \\ m_2 &= (m_G - m_R \cos\theta)\ \text{cosec}\ \theta \\ n_2 &= (n_G - n_R \cos\theta)\ \text{cosec}\ \theta \end{aligned}\right\} \quad . \quad . \quad . \quad . \quad (2)$$

The analysis is carried out by examining the conditions which must be satisfied for the shot and the target to arrive simultaneously at T_1. The algebraic manipulations involved in this are of some complexity, and have already been published elsewhere[5]. The results take the simplest form for the special case where the transverse component d_2 of the trajectory is small enough to be neglected, a condition which is very nearly satisfied in most ordinary circumstances. For this case the components of lead angle are given by

$$\tan\alpha_1 = \frac{V_G(V_0t - d_1)\sin\theta + V_0\{R\omega_1 t + l_2\delta x + m_2\delta y + n_2(\delta z + d_3)\}}{V_G(V_0t - d_1)\cos\theta + V_0\{R + \dot{R}t + l_R\delta x + m_R\delta y + n_R(\delta z + d_3)\}} \quad . \quad (3)$$

and $$\sin\alpha_2 = \frac{V_0}{d_1 V_M}[R\omega_2 t + l_1\delta x + m_1\delta y + n_1(\delta z + d_3)] \quad . \quad . \quad . \quad . \quad (4)$$

where ω_1 and ω_2 are the component angular velocities of the sight line about N_1 and N_2 respectively, and the quantities V_0, t, d_1 and d_3 are inter-related by the two equations

$$\begin{aligned} &V_G^2(V_0t - d_1)^2 + 2V_0V_G(V_0t - d_1)[(R + \dot{R}t)\cos\theta + R\omega_1 t\sin\theta + l_G\delta x + m_G\delta y + n_G(\delta z + d_3)] + \\ &+ V_0^2[(R + \dot{R}t)^2 + (R\omega_1 t)^2 + (R\omega_2 t)^2 + \delta x^2 + \delta y^2 + (\delta z + d_3)^2 + \\ &+ 2(R + \dot{R}t)\{l_R\delta x + m_R\delta y + n_R(\delta z + d_3)\} + 2R\omega_1 t\{l_2\delta x + m^2\delta y + n_2(\delta z + d_3)\} + \\ &+ 2R\omega_2 t\{l_1\delta x + m_1\delta y + n_1(\delta z + d_3)\}] = V_M^2 d_1^2 \quad . \quad . \quad . \quad . \quad (5) \end{aligned}$$

and $$\begin{aligned} &V_0^2 d_1 - 2V_0V_G[(R + \dot{R}t)\cos\theta + V_G t + R\omega_1 t\sin\theta + l_G\delta x + m_G\delta y + n_G(\delta z + d_3)] + \\ &+ (V_G^2 - V_M^2)d_1 = 0 \quad . \quad . \quad . \quad . \quad . \quad (6) \end{aligned}$$

and by two further equations derived from the ballistic analysis.

For the more general case where d_2 is not negligible, an approximate solution can be obtained by adding the quantities

$$-d_2(V_G m_G + V_M m_R)/[(V_G l_G + V_M l_R)^2 + (V_G m_G + V_M m_R)^2]^{\frac{1}{2}} \text{ to } \delta x$$

and

$$d_2(V_G l_G + V_M l_R)/[(V_G l_G + V_M l_R)^2 + (V_G m_G + V_M m_R)^2]^{\frac{1}{2}} \text{ to } \delta y$$

in equations (3), (4), (5) and (6), and by introducing a further relationship to define d_2 from ballistic considerations.

An exact solution for the case where d_2 is not negligible is given by

$$\alpha_1 = \sin^{-1}\frac{[1-\sin^2\alpha_2]^{\frac{1}{2}}}{[A^2+B^2]^{\frac{1}{2}}} - \tan^{-1}\frac{B}{A} \quad . \quad . \quad . \quad . \quad (7)$$

and

$$\sin\alpha_2 = \frac{V_0}{V_M d_1}\left[\frac{(X_1+vX_2)\{(m_G n_R - m_R n_G)+v\,(n_G l_R - n_R l_G)\}}{(1+v^2)} + X_3(l_G m_R - l_R m_G)\right]\operatorname{cosec}\theta \quad . \quad . \quad . \quad . \quad . \quad . \quad (8)$$

where

$$X_1 = [(R+\dot{R}t)l_R + V_G l_G t + Rt\{\omega_1(l_G - l_R\cos\theta) + \omega_2(m_G n_R - m_R n_G)\}\operatorname{cosec}\theta + \delta x]$$

$$X_2 = [(R+\dot{R}t)m_R + V_G m_G t + Rt\{\omega_1(m_G - m_R\cos\theta) + \omega_2(n_G l_R - n_R l_G)\}\operatorname{cosec}\theta + \delta y]$$

$$X_3 = [(R+\dot{R}t)n_R + V_G n_G t + Rt\{\omega_1(n_G - n_R\cos\theta) + \omega_2(l_G m_R - l_R m_G)\}\operatorname{cosec}\theta + \delta z + d_3]$$

$$A = \frac{1}{V_M}\left[\frac{V_0}{d_1}\left\{\frac{(X_1+vX_2)[(l_G - l_R\cos\theta)+v\,(m_G - m_R\cos\theta)]}{(1+v^2)} + X_3(n_G - n_R\cos\theta)\right\} - V_G\sin^2\theta\right]\operatorname{cosec}\theta$$

$$B = \frac{1}{V_M}\left[\frac{V_0(X_1+vX_2)\,(l_R+vm_R)}{d_1(1+v^2)} + \frac{V_0 X_3 n_R}{d_1} - V_G\cos\theta\right],$$

and v is defined by $\quad (X_1^2 - d_2^2)v^2 - 2X_1X_2v + (X_2^2 - d_2^2) = 0 \quad . \quad . \quad . \quad (9)$

and V_0, t, d_1, d_2 and d_3 are inter-related by the equations

$$V_0^2[(X_1+vX_2)^2 + (1+v^2)X_3^2] - 2d_1V_0V_G[(X_1+vX_2)\,(l_G+vm_G) + (1+v^2)\,n_G X_3] + d_1^2\,(1+v^2)\,(V_G^2 - V_M^2) = 0 \quad . \quad (10)$$

and $$V_0^2 - 2\frac{V_G V_0}{d_1}\left[\frac{(X_1+vX_2)\,(l_G+vm_G)}{(1+v^2)} + n_G X_3\right] + (V_G^2 - V_M^2) = 0 \quad . \quad (11)$$

and by three further equations from the ballistic analysis.

3.3 Discussion of the First Part of the Kinematic Analysis

The kinematic analysis outlined in Section 3.2 gives equations which, when combined with the results of the ballistic analysis, allow the required direction of the gun line to be determined from the primary independent variables to as close an accuracy as is consistent with the inherent uncertainties associated with the δ terms. Apart, therefore, from the extreme complexity, the equations defining the components of lead angle could be used for the design of a gun sighting system having the line of sight directly controlled by the gunner and the gun direction controlled automatically in accordance with the equations. Sighting systems of this type, known as "director systems," are in common use for the control of heavy guns in ship and land based installations, but their complexity and cost are too great to make them generally suitable for use in aircraft installations. In aircraft a simpler form of mechanism known as a lead-computing sight is almost universally employed. In this the gunner exercises direct control, not over the sight line but over the gun line, the sight line being linked to this and following its movements through a quasi-elastic coupling in which the computations of lead angle take place. In a typical lead-computing sight, the sight line is defined by purely optical means and has no tangible mechanical existence, with the result that the magnitude of the angle θ and the plane containing it cannot readily be determined, and there is therefore an important gap in the information required in the equations of Section 3.2.

The lead-computing sight does, however, allow information to be obtained about the angular velocity of the sight line, and it allows the angle ψ and the plane containing it to be determined, besides providing a measure of the lead angle. To obtain results which can be applied directly to the design problems of such a sight, the kinematic analysis must therefore be approached in a manner which treats ψ and the plane of ψ as independent variables, while θ and the plane of θ are treated as unknown quantities. The analysis must also make use of the known components of angular velocity of the sight line, and the results will then show the components of lead angle referred to the ψ-plane.

The relationship between the planes and angles associated with this argument is shown in Fig. 2 which shows the gunner's line of flight G_0V, the line of sight to the target G_0T_0 and the gun line G_0G_1. The line G_0P is located in the plane T_0G_0V (the plane of θ) in such a position that the lead angle components $T_0G_0P\,(\alpha_1)$ and $G_1G_0P\,(\alpha_2)$ are in mutually perpendicular planes. In the analysis of Section 3.2, G_0T_0 and G_0V are given, the angle θ between them and the plane of θ being known, while the required position of G_0G_1 is determined from equations which define the angles α_1 and α_2 in terms of the angular velocity of G_0T_0 and other measurable quantities. In the lead-computing sight, however, the angle θ and the plane containing it cannot be found, although the angle ψ between the gun line and flight line and the plane containing ψ can be found, while the angular velocity of the sight line can also be determined. In this situation the lead angle is defined by the orthogonal components α_1', α_2', located in and at right angles to the plane of ψ. For this purpose an additional construction line G_0Q in the ψ-plane must be

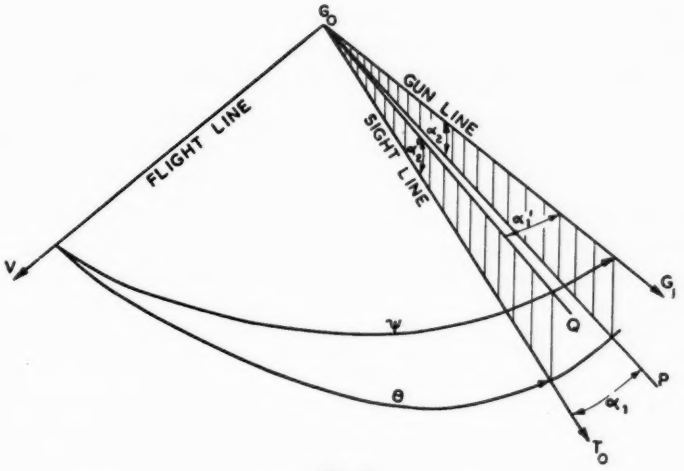

Fig. 2.
Relationship between details of first and second kinematic analyses.

introduced to make the component lead angles G_1G_0Q (α_1') and T_0G_0Q (α_2') mutually perpendicular. The kinematic analysis associated with the determination of α_1' and α_2' is outlined in the next section.

3.4 The Kinematic Analysis. Second Part

In the second part of the kinematic analysis, the angular velocity of the sight line is measured in terms of the components ω_1', which produces motion of the sight line at right angles to the plane T_0G_0Q, and ω_2', which produces motion of the sight line in the plane T_0G_0Q. Three auxiliary construction lines are required: N' perpendicular to the plane G_1G_0V; N_1' about which the component angular velocity ω_1' occurs; and N_2' about which the component angular velocity ω_2' occurs. The analysis is carried out as in the first part by examining the necessary conditions for the shot and target to arrive simultaneously at T_1. The results are as follows:—

$$\alpha_1' = \sin^{-1}\frac{R\omega_1' t}{(X^2+Y^2)^{\frac{1}{2}}} + \tan^{-1} Y/X \quad . \quad . \quad . \quad . \quad . \quad (12)$$

$$\alpha_2' = \tan^{-1}\frac{R\omega_2' t}{(R+\dot{R}t)} + \sin^{-1}\frac{Z}{[(R\omega_2' t)^2+(R+\dot{R}t)^2]^{\frac{1}{2}}} \quad . \quad . \quad (13)$$

where

$$X = \frac{1}{V_0}[(V_0 t - d_1)V_G \cos\psi - d_1 V_M] + [l_M\delta x + m_M\delta y + n_M(\delta z + d_3)] +$$

$$+ \frac{d_2 V_G(l_M m_G - l_G m_M)}{[(V_M l_M + V_G l_G)^2 + (V_M m_M + V_G m_G)^2]^{\frac{1}{2}}} \quad . \quad . \quad . \quad (14)$$

$$Y = \frac{1}{V_0}(V_0 t - d_1)V_G \sin\psi + \\ + [(l_G - l_M \cos\psi)\delta x + (m_G - m_M \cos\psi)\delta y + (n_G - n_M \cos\psi)(\delta z + d_3)] \operatorname{cosec}\psi + \\ + \frac{d_2(l_G m_M - l_M m_G)(V_M + V_G \cos\psi)\operatorname{cosec}\psi}{[(V_M l_M + V_G l_G)^2 + (V_M m_M + V_G m_G)^2]^{\frac{1}{2}}} \quad . \quad . \quad . \quad (15)$$

$$Z = [(m_M n_G - m_G n_M)\delta x + (n_M l_G - n_G l_M)\delta y + (l_M m_G - l_G m_M)(\delta z + d_3)] \operatorname{cosec}\psi + \\ + \frac{d_2[V_M(n_G - n_M \cos\psi) + V_G(n_G \cos\psi - n_M)] \operatorname{cosec}\psi}{[(V_M l_M + V_G l_G)^2 + (V_M m_M + V_G m_M)^2]^{\frac{1}{2}}} \quad . \quad . \quad . \quad (16)$$

and the relationships corresponding to equations (5) and (6) of the first analysis are provided by

$$V_0^2 = V_G^2 + V_M^2 + 2V_G V_M \cos\psi \quad . \quad . \quad . \quad . \quad (17)$$

and

$$(R + \dot{R}t)^2 + (R\omega_1' t)^2 + (R\omega_2' t)^2 = X^2 + Y^2 + Z^2 \quad . \quad . \quad . \quad (18)$$

It is of interest to note that the results of this analysis are not complicated by the presence of the d_2 term to the same extent as in the results of the first analysis.

3.5 Approximations Derived from the Kinematic Analysis

The results obtained in Sections 3.2 and 3.4 are too complex for practical applications, and it is of interest to examine the approximate results, which can be obtained by expressing these results as series in ascending powers of small terms. The following results are obtained from the first analysis:—

$$\alpha_1 = \frac{V_G}{R}(t - t_0)\sin\theta + \omega_1 t + \frac{1}{R}\left[l_2\delta x + m_2\delta y + n_2(\delta z + d_3)\right] + \text{higher terms} \quad (19)$$

and

$$\alpha_2 = \frac{R\omega_2 t}{V_M t_0} + \frac{1}{V_M t_0}\left[l_1\delta x + m_1\delta y + n_1(\delta z + d_3)\right] + \text{higher terms}. \quad . \quad . \quad (20)$$

where t_0 represents the ratio d_1/V_0, *i.e.* the time the projectile would take to travel the distance d_1 if it travelled without retardation.

The corresponding approximations from the second analysis are

$$\alpha_1' = \frac{R\omega_1' t}{V_M t_0} + \frac{V_G}{V_M}\left(\frac{t}{t_0} - 1\right)\sin\psi + \text{higher terms} \quad . \quad . \quad (21)$$

and

$$\alpha_2' = \omega_2' t + \text{higher terms}. \quad . \quad . \quad . \quad . \quad . \quad . \quad . \quad (22)$$

The results given in equations (19) to (22) will be found to bear a close resemblance to the results of the simplified analysis presented in Section 5. They illustrate by their form that the components of the lead angle can be treated, to a close

approximation, as the vector sums of independent parts, depending on the angular velocity of the line of sight and the retardation of the projectile due to air resistance. The gravity components of lead angle are represented by the terms in d_3.

4. The Ballistic Aspects of the Problem

4.1 The General Problem

The ballistic part of the aiming problem is concerned with the factors which influence the motion of the projectile along the trajectory, and with the development of expressions showing the relationship between the time of flight t, the trajectory projections d_1, d_2, d_3 and the initial conditions under which the projectile is fired. This subject is already covered by a considerable literature[1,2,3,4] and it is only necessary here to quote those results which are of most significance in aerial gunnery.

The whole pattern of the ballistic problem and its solution is set by the fact that the resistance of the air to projectile motion cannot be represented exactly by any mathematical expression, and therefore no exact solution of the equations of motion of the projectile can be obtained. A number of approximate procedures have been described, however, by which results of adequate accuracy can be obtained. The simplest of these which is suitable for all ordinary problems in aerial gunnery is based on an expression for air resistance of the form $(A\rho/c)\,v^{1.5}$, where A is a constant which can be adjusted to give the best approximate fit over the velocity range considered, ρ is the air density, c is a constant which takes account of the projectile size and shape, and v is the velocity of the projectile through the air.

In the most general trajectory analysis, account must be taken of the fact that the projectile may be yawed, *i.e.* its axis of figure may not point along its direction of motion, in which case the aerodynamic drag will be greater than it would be without yaw, and its direction may not be exactly in line with the direction of motion. The trajectory analysis with yaw is considerably more complex than without yaw, and it is preferable to consider the results for the simple case without yaw before examining the complications introduced by yaw.

4.2. The Trajectory Without Yaw

When yaw is absent the transverse displacement d_2 is zero, and the relationships between t_1, d_1, and d_3 derived from the simple drag law quoted in Section 4.1. are

$$d_1 \simeq \frac{V_0 t}{(1+Jt)} \quad . \quad . \quad . \quad . \quad . \quad . \quad . \quad (23)$$

$$d_3 \simeq \tfrac{1}{2} g t^2 \left(\frac{1+\frac{1}{3}Jt}{1+Jt}\right) \quad . \quad . \quad . \quad . \quad . \quad . \quad (24)$$

where $$J = \frac{A\rho\sqrt{V_0}}{2Mc} \quad . \quad . \quad . \quad . \quad . \quad . \quad . \quad (25)$$

and M denotes the mass of the projectile.

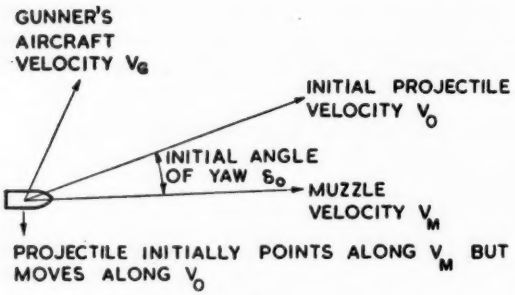

Fig. 3.
Initial yaw produced by firing into a cross wind.

4.3. Description of the Yawing Motion

In general there are a number of causes by which yaw can be introduced into projectile motion. The most important of these in aerial gunnery is that produced by firing into a cross wind when the initial direction of relative motion between the air and the projectile is at an angle to the axis of the projectile, as shown in Fig. 3.

The yawing motion produced by firing into a cross wind is described by the equation

$$\delta e^{i(\phi-\phi_0)} \simeq \frac{\delta_0}{2}\left[\left(1-\frac{1}{\sigma}\right)e^{\{-(q_1+q_2)+i(p_1+p_2)\}} + \left(1+\frac{1}{\sigma}\right)e^{\{-(q_1-q_2)+i(p_1-p_2)\}}\right] \quad (26)$$

where δ is the magnitude of the yaw angle

ϕ is the orientation of the plane of yaw relative to an arbitrary reference plane

δ_0, ϕ_0 are the initial values of δ and ϕ

σ is a constant associated with the dynamic stability of the projectile, having a value generally in the range $0{\cdot}5 \leqslant \sigma \leqslant 1$

p_1, p_2, q_1, q_2 are functions of the aerodynamic constants, and of the spin of the projectile, and of time. They increase monotonically, but not necessarily linearly with time from zero at the origin of the trajectory.

Equation (26) represents a motion which is the sum of two damped rotating vectors having in general different initial magnitudes, different rates of rotation, and different damping factors. An illustration of the characteristic rosette pattern obtained by plotting δ against ϕ in polar co-ordinates is shown in Fig. 4 for a typical set of circumstances. In this example the first two complete rotations of ϕ about the origin would occupy about the first 0·05 second from the start of the trajectory, and the magnitude of the yaw would be reduced to one tenth of its initial value after about 0·25 second.

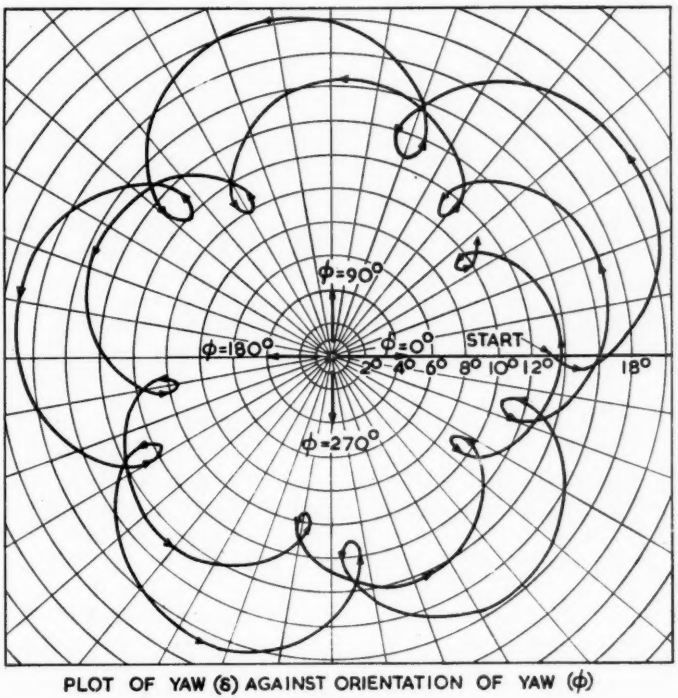

Fig. 4.
Typical example of yawing motion.

4.4. The Effects of Yaw on the Trajectory

From the practical point of view, the importance of the yawing motion which occurs when a projectile is fired into a cross wind is not in the yawing motion itself, but in the effects of the yaw on the forward and transverse motion. These effects may be considered under two separate headings which are discussed in decreasing order of practical importance.

4.4.1. *The Effects of Yaw on the Forward Motion*

When the projectile is yawed, the projected area it presents in the direction of motion is greater than in the unyawed condition and the aerodynamic drag is therefore increased. Investigations have shown that, up to yaw angles of about 16°, the increase of drag due to yaw is closely proportional to the square of the angle of yaw, so that the effect of yaw on forward motion can be taken into account by introducing a factor of the form $(1+K\delta^2)$ into the equations of motion before integration.

The solution of the trajectory equations when drag due to yaw is introduced is considerably complicated, but some simplification can be introduced by examining

the square of the yaw amplitude given by equation (26). This is

$$\delta^2 = \frac{\delta_0^2}{4}\left[\left(1-\frac{1}{\sigma}\right)^2 e^{-2(a_1+a_2)} + \left(1+\frac{1}{\sigma}\right)^2 e^{-2(a_1-a_2)} + 2\left(1-\frac{1}{\sigma^2}\right)^2 e^{-2a_1}\cos 2p_2\right] \quad (27)$$

The periodic term in this equation has an amplitude which is comparable with the non-periodic terms, but the variations in drag which it produces fluctuate so rapidly that its effect is of no significance in practical trajectory calculations. It is sufficient therefore for practical purposes to calculate the mean square of the yaw over the periodic time of the oscillatory term in equation (27) and to use this mean square value in the trajectory calculation.

The resulting expression for the effective mean square yaw at time t, denoted by $\overline{\delta^2}(t)$ is

$$\overline{\delta^2}(t) \simeq \frac{\delta_0^2}{4}\left[\left(1-\frac{1}{\sigma}\right)^2 e^{-2(a_1+a_2)} + \left(1+\frac{1}{\sigma}\right)^2 e^{-2(a_1-a_2)}\right]. \quad (28)$$

Even with this simplification, direct integration of the trajectory equations is not possible, and recourse must be had to numerical methods of integration.

4.4.2. *The Effects of Yaw on the Transverse Motion*

In addition to the increase in drag produced by yaw, another effect, generally of small practical importance, follows from the component of aerodynamic force acting at right angles to the direction of forward motion. This transverse force analogous to the lift on an aerofoil produces a transverse acceleration of the projectile, following the rotations of the yaw plane, with the result that the path of the centre of gravity is changed from the nearly straight line it would follow in the absence of yaw to a helical form lying close to this line. For analytical purposes the resulting departure from the no-yaw path is considered in two separate parts, the first being a rosette form of spiral motion similar in general appearance to the yaw rosette shown in Fig. 4, and the second a steady deviation from the no-yaw path.

The rosette component of the motion is described by the equation

$$re^{i\Psi} = \frac{2kU}{\Omega^2\sigma}\delta_0 e^{i\varphi_0}\left[\frac{(1-\sigma)}{(1+\sigma)^2} e^{\{-(a_1+a_2)+i(p_1+p_2)\}} - \frac{(1+\sigma)}{(1-\sigma)^2} e^{\{-(a_1-a_2)+i(p_1-p_2)\}}\right] \quad (29)$$

where r and Ψ denote the radius and orientation of the displacement in the spiral from the corresponding position in the equivalent plane trajectory. The similarity of this motion to the rosette yawing motion is apparent from a comparison between equations (26) and (29), but the first term in the square bracket of equation (29) is negligible in comparison with the second term, with the result that the motion takes the form of a simple damped spiral. In typical cases the initial radius of the spiral is only a small fraction of an inch so that this component of the motion is of no practical significance.

The second component of the transverse motion is a progressive displacement represented by the equation

$$H_2+iZ_2=-\frac{2ik}{\Omega}\frac{(1+\sigma^2)}{(1-\sigma^2)}\delta_0 e^{i\psi_0}\int U\,dt \quad . \quad . \quad . \quad (30)$$

where H_2 and Z_2 denote the Cartesian components of the displacement. In most practical cases this transverse motion represents a departure of only a small fraction of a degree from the equivalent trajectory without yaw.

5. The Simplified Analysis of the Aiming Problem

In the simplified analysis of the aiming problem mentioned in Section 1 the following approximations are made.

Firstly, it is assumed that the effects of gravity can be treated separately from the other factors which influence the lead angle. In making this simplification it is assumed that, when the position of the projectile has been calculated at any given time as though gravity were absent, its actual position will be at a vertical distance of $\frac{1}{2}gt^2$ below that point, where g is the acceleration of gravity and t the time of flight to the point in question. If air resistance were absent this assumption would be strictly accurate, and it is in fact sufficiently accurate for most ordinary conditions.

Secondly, it is assumed that the target flies at constant speed along a straight path. Under ordinary conditions it is not possible for an aircraft to change speed sufficiently during the time of flight of the projectile to have any appreciable effect on the lead angle calculated in this way, although the acceleration which can be applied across the line of flight can curve its path sufficiently to have a serious influence on the lead angle at longer ranges. The effects of such curvature can be calculated with ample accuracy by first treating the target motion as being at constant speed in a straight line and then finding its displacement from the point it would have reached under these conditions by virtue of its acceleration.

Thirdly, it is assumed that in the absence of gravity the projectile would travel through the air in a straight line whose direction is defined by the resultant of its muzzle velocity relative to the gun and the gun's velocity through the air. This assumption is very nearly true, but it neglects the fact that the projectile moves through the air along a spiral path of small and rapidly decreasing amplitude, the axis of which is slightly inclined to the assumed straight path.

The analysis is carried out by reference to Fig. 5 where G_0GG_1 represents the path of the gun and T_0T_1 that of the target. The shot is fired when the gun is at G and the target at T_0. The velocities are denoted by V_G for the gun, V_M for the muzzle velocity of the shot and V_T for the target. The initial velocity of the shot resulting from V_M and V_G is denoted by V_0 and the average velocity from G to T_1 by V_A. The ratio of V_0 to V_A is denoted by p and the time of flight of the shot from G to T_1 by t. The line of sight GT_0 makes angles θ and ϕ with G_0GG_1 and

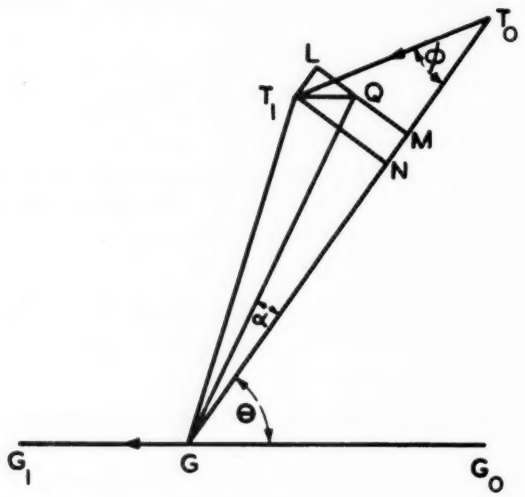

Fig. 5.
Construction for the simplified analysis of the aiming problem.

T_0T_1 respectively and GQ represents the gun line. The lead angle T_0GQ is denoted by α. Initially it is necessary to restrict consideration to the special case where G_0GG_1 and T_0T_1 are coplanar, but it is shown later how the treatment can be extended to meet the more general case where this condition is not satisfied.

To determine the lead angle, the point Q is found by drawing through T_1 parallel to G_0GG_1 to meet the gun line in Q. It is also necessary to draw T_1N and MQL perpendicular to GT_0 and T_1L parallel to GT_0. The time which the shot would take to reach T_1 in the absence of retardation, *i.e.* the vacuum time, is t_0. The following relationships hold:—

$$MQ=NT_1-QL \qquad . \quad . \quad . \quad . \quad (31)$$

where $MQ=GQ\sin\alpha$

$$NT_1=T_0T_1\sin\phi$$

$$QL=T_1Q\sin QT_1L.$$

Since $\dfrac{GQ}{GT_1}=\dfrac{V_M}{V_0}$ and $GT_1=tV_A=t_0V_0$,

$$GQ=t_0V_M.$$

Also $T_0T_1=tV_T$.

$$\text{Since} \quad \frac{T_1Q}{GQ} = \frac{V_G}{V_M},$$

$$T_1Q = \frac{V_G}{V_M} GQ = t_0 V_G.$$

$$\text{Also} \quad QT_1L = \theta.$$

Thus equation (31) is equivalent to

$$t_0 V_M \sin \alpha = tV_T \sin \phi - t_0 V_G \sin \theta$$

which, on replacing sin α by α and dividing throughout by $t_0 V_M$, becomes

$$\alpha = p \frac{V_T}{V_M} \sin \phi - \frac{V_G}{V_M} \sin \theta \quad . \quad . \quad . \quad (32)$$

The angular velocity of the line of sight to the target at the moment the shot is fired is given by $\omega R = V_T \sin \phi - V_G \sin \theta$, and this, in combination with (32), leads to

$$\alpha = p \frac{\omega R}{V_M} + (p-1) \frac{V_G}{V_M} \sin \theta \quad . \quad . \quad . \quad (33)$$

In the more general case, where G_0GG_1 and T_0T_1 are not coplanar, the result of equation (33) still applies, provided that α, ω and V_G are regarded as vector quantities and are compounded accordingly. Alternatively, equation (33) may be regarded as applying only to components of ω and α lying in the plane defined by the gunner's path G_0GG_1 and the sight line GT_0. A second equation from which the V_G term is absent is then required to relate the components of α and ω in a plane at right angles to this.

In practical cases of aerial gunnery a further component of lead angle must also be introduced to allow for the gravity drop of the shot, which has been neglected in the foregoing treatment. This component lies in a vertical plane and must be calculated to compensate for the vertical distance which the shot falls under the influence of gravity during its time of flight to the target.

The similarity between the result expressed by equation (33) and the approximations derived from the full kinematic analysis in Section 3.5 will be immediately apparent.

6 The Aiming Problem as the Gunner Sees It

6.1. The Gunner's Viewpoint

In the foregoing discussion the aiming problem has been examined from the point of view of an observer at rest in the air through which the gunner and target are moving. This treatment provides all that is strictly necessary to obtain a

solution of the problem, although it is useful in conclusion to examine the situation from the gunner's point of view as well, because the gunner always feels himself to be at rest and may find some difficulty in reconciling what he sees with the results of the foregoing treatment, unless the matter is correctly explained to him.

When tracer ammunition is used, the gunner can often see his bullets as they travel towards the target. For the first few yards they appear as streaks of light, but for the remainder of their flight he sees them as spots of light which generally seem to be moving on strongly curved paths. To the gunner who knows that, apart from the effect of gravity, they travel through the air in straight lines, their appearance may be very surprising, because the observed curvature is often much greater than that due to gravity and may be in any direction.

The apparent curvature of the bullet paths as seen by the gunner arises partly from the effect of gravity, but is also influenced strongly by the deceleration due to air resistance acting in combination with the gunner's motion through the air, and by any angular motion of the sight line which may be present.

6.2. Curvature due to Gravity

The influence of gravity is to curve the flight path of the bullet downwards slightly below the straight path which it would otherwise follow. This effect can be observed alone when a gun is fixed on the ground. The curvature which is produced is much smaller than that due to the other two causes.

6.3. Apparent Curvature due to Deceleration of the Projectile

To understand the second cause of apparent curvature it is useful to consider the special situation in which the gunner and target are travelling on parallel courses at the same speed. In the absence of air resistance the target would be hit if the gun pointed directly towards it, and the bullet would be seen by the gunner as moving directly towards the target. This ideal situation is shown in Fig. 6 where $G_1G_2G_3$ represents the gunner's path through the air, and $T_1T_2T_3$ represents the target's path.

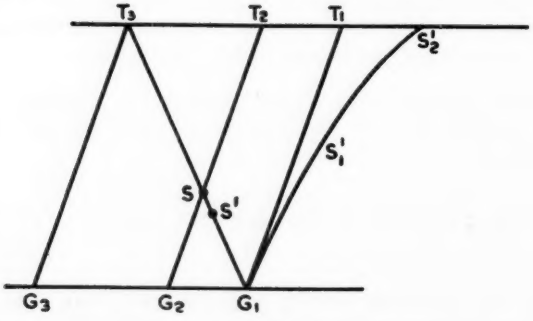

Fig. 6.
Apparent curvature due to projectile deceleration.

The gun is fired at G_1, while pointing towards the target at T_1, and the shot travels along G_1T_3 to meet the target at T_3. The point G_2 represents the position of the gunner at any arbitrarily chosen instant during the interval between the firing and impact of the shot, and T_2 represents the position of the target at the same instant. The postion of the gunner at the moment of impact is represented by G_3. In the absence of air resistance and gravity, the shot travels with constant velocity along G_1T_3 and thus remains at the point S, where G_1T_3 intersects G_2T_2, throughout its flight. The direction in which the gunner sees the shot thus remains constant along the gun line at the instant of firing.

When air resistance is present the shot loses velocity as it travels along G_1T_3, and will thus only have reached some position such as S' when the gunner and target are at the ends of the line G_2T_2. The gunner's line of sight to the shot will therefore lag behind the direction of the gun barrel by the angle $S'G_2S$, and this angle will increase as the shot travels away from the gunner, because the distance SS' by which the shot lags behind its "no-resistance" position increases more rapidly than the distance G_2S. The apparent path of the shot as seen by the gunner thus takes the form of a curve represented by $G_1S_1'S_2'$ which trails behind the gun line, and the gun must therefore be aimed ahead of the target by the angle which this curve subtends for a hit to be obtained. This angle is known as the trail angle, and the distance T_1S_2' is known as the trail distance.

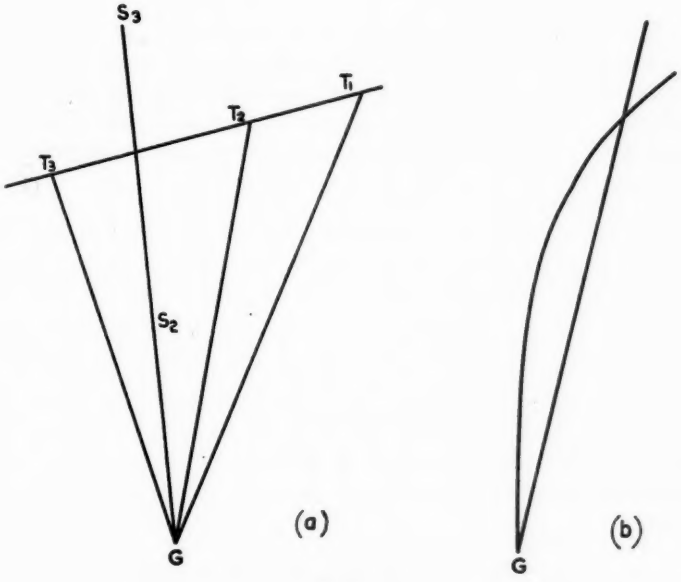

Fig. 7.
Apparent curvature due to sight line rotation.

6.4. Apparent Curvature due to Sight Line Rotation

The third cause of apparent curvature, rotation of the sight line, is most easily understood by considering what would happen in the absence of gravity and air resistance with the gun at rest and the sight line rotating.

Fig. 7 (*a*) shows what actually occurs. The shot is fired from G when the target is at T_1 and travels along the straight line GS_2S_3. The shot positions S_2 and S_3 correspond to the same instants as the target positions T_2 and T_3, and the shot is supposed, for the sake of the present argument, to pass as close as possible to the target without actually hitting it. When the shot first leaves the gun, the angle between the line of sight to the target and that to the shot, as seen by the gunner is T_1GS_2, but when it reaches S_2 this angle is reduced to T_2GS_2 and, as it passes the target, the angle is reduced substantially to zero. Afterwards, when the shot has passed the target and reached S_3, the angle has changed sign and become S_2GT_3.

This situation as it appears to the gunner is shown in Fig. 7 (*b*). With his attention fixed on the target, the path of the bullet appears to him to curve in towards the apparently stationary line of sight to the target, and eventually to cross it. The angle through which the gunner's line of sight must be turned to follow this curvature is given by the product of the angular velocity and the time of flight. In the general case it arises from the relative speed between the gunner and target, and it is therefore known as the relative speed component of the lead angle.

6.5. The General Case

In the general case the three causes of curvature will act simultaneously to produce the resulting curvature seen by the gunner, and the total lead angle will therefore be composed of a trail component in the plane defined by the sight line and the gunner's line of motion, a relative speed component in the plane defined by the relative motion between the target and gunner, and a gravity component in the vertical plane.

References

1. Cranz, C. and Becker, K. *Handbook of Ballistics.* H.M.S.O. London (Translated from the Second German Edition), 1921.

2. Fowler, R. H., Gallop, E. G., Lock, C. N. H. and Richmond, H. W. The Aerodynamics of a Spinning Shell. *Transactions of the Royal Society* A. Vol. 221, pp. 295-387, 1920, and Vol. 222, pp. 227-247, 1922.

3. Unpublished National Physical Laboratory reports.

4. Unpublished Ordnance Board report.

5. Unpublished Ministry of Supply report.

A Finite Series Solution for Grillages under Normal Loading

D. F. HOLMAN

(Naval Construction Research Establishment)

SUMMARY: A method has been given by Klitchieff[1, 2] for analysis of grillages of intersecting beams under lateral loading. Klitchieff's solution was in the form of infinite Fourier series and the expressions for bending moments converged approximately as Σn^{-2}, making numerical computation difficult. This paper shows that, for grillages in which one set of beams are evenly spaced, Klitchieff's solution can be adapted to give finite series for deflections and bending moments at the intersections of the beams. The number of terms in the series is not greater than the number of beams in the equally spaced set (referred to in this paper as set "A"). A numerical example is given and an accurate solution is obtained with appreciably less computation than other known methods would entail.

1. Introduction

The two orthogonal sets of beams may be called sets "A" and "B." In the procedure given by Klitchieff the deflection of the s^{th} beam of set B is expressed as a Fourier series with unknown coefficients C_{ks}, $(s=1, 2, \ldots\ldots, q)$. Bending moments in the same beam can then be expressed in two ways, firstly in terms of the second derivative of deflection, and secondly in terms of the forces on the beam. By beam theory for the r^{th} beam of set A, we can find the unknown reactions R_{rs} in this second expression in terms of deflections at the intersections of this beam with those of set B. These deflections can then be replaced by their Fourier expansions. Equating the two expressions for bending moment and applying a finite Fourier transformation, a set of algebraic equations involving the q infinite sets of unknown coefficients is obtained; and, in cases where the beams of a set are uniform, equal and evenly spaced, by taking advantage of the periodic properties of these coefficients the equations can be reduced to a finite set with q unknowns. (If there is symmetry in the A-direction the number of unknowns is $\frac{1}{2}q$ or $\frac{1}{2}(q+1)$). When these have been solved, the deflections and bending moments may be found as the sums of infinite series. However, the bending moment expansion is of the form $\Sigma n^{-2} w(n)$, where $w(n)$ is a trigonometrical function, so that computation presents considerable difficulties. The following adaptation of the method is intended to overcome these.

Received April 1956

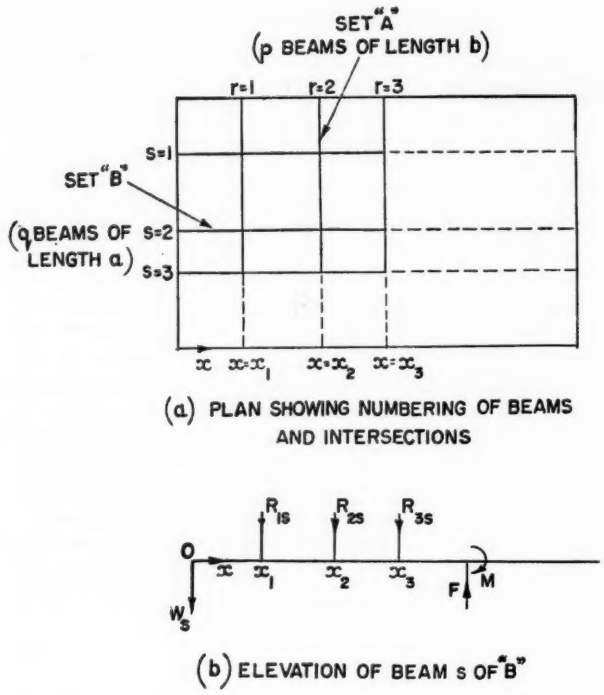

Fig. 1.
The general grillage problem.

NOTATION

A, B	the two sets of intersecting beams
p, q	numbers of beams in sets A, B, respectively
w	deflection
F	shear force
M	bending moment
R_{rs}	reaction between the r^{th} beam of set A and s^{th} beam of set B
$h = p+1$	
a, b	lengths of B-beams and of A-beams respectively
I_r, I_s	moments of inertia of A-beams and B-beams respectively
c, d	spans between consecutive A-beams and B-beams respectively
x	distance from end of B-beams
x_r	distance of r^{th} A-beam from end of B-beams

C_{ks}, C_{ms}, C_{vs} coefficients of the deflection expansion

$Z_{ms} = (m\pi)^4 C_{ms}$

$V = |\, m+2jh \,|$, where j is any integer.

Suffixes

r, s refer to the r^{th} beam of set A and the s^{th} beam of set B.

2. Conversion of Solution to Finite Series

2.1. First Case: Simply-Supported Ends

The deflection of the s^{th} beam of B can be represented by

$$w_s = \sum_{k=1}^{\infty} C_{ks} \sin \frac{k\pi x}{a}, \qquad (1)$$

and the bending moment is then

$$M_s = EI_s \frac{d^2w}{dx^2} = -EI_s \sum_{k=1}^{\infty} \left(\frac{k\pi}{a}\right)^2 C_{ks} \sin \frac{k\pi x}{a}. \qquad (2)$$

R_{rs} is defined as the downward reaction on the s^{th} beam at its intersection with the r^{th} beam of set A, so that, taking moments (if there is no other load on the B-beam),

$$M_s = -\sum_{r=1}^{p} x R_{rs}\left(1-\frac{x_r}{a}\right) + \sum_{r=1}^{p} R_{rs}(x-x_r)\,U(x-x_r), \qquad (3)$$

$$\text{where} \quad \left.\begin{aligned} U(t) &= 0, \quad t<0 \\ &= 1, \quad t>0. \end{aligned}\right\} \qquad (4)$$

Equating these two expressions, multiplying by $\sin(m\pi x/a)$ and integrating over $(0, a)$ with respect to x, (m is any positive integer),

$$-EI_s C_{ms}\left(\frac{m\pi}{a}\right)^2\left(\frac{a}{2}\right) = -\sum_{r=1}^{p} R_{rs}\left(\frac{a}{m\pi}\right)^2 \sin\frac{m\pi x_r}{a}. \qquad (5)$$

If the beams of set A are equally spaced, then $hx_r = ar$, where $h = p+1$, so that equation (5) becomes, writing Z_{ms} for $(m\pi)^4 C_{ms}$,

$$EI_s a^{-3} Z_{ms} = 2\sum_{r=1}^{p} R_{rs} \sin\frac{m\pi r}{h}; \quad m = 1, 2, \ldots, \qquad (6)$$

Now, for integral values of n and k which are less than h, we have

$$2\sum_{r=1}^{h-1} \sin\frac{n\pi r}{h}\sin\frac{k\pi r}{h} = \left\{\begin{aligned} &h, && \text{if } n=k \\ &0, && \text{if } n\neq k. \end{aligned}\right. \qquad (7)$$

Then, from (6), we obtain

$$EI_s a^{-3} \sum_{m=1}^{p} Z_{ms} \sin \frac{m\pi r}{h} = 2 \sum_{m=1}^{p} \sum_{t=1}^{p} R_{ts} \sin \frac{m\pi t}{h} \sin \frac{m\pi r}{h}$$
$$= hR_{rs} \quad . \quad . \quad . \quad . \quad . \quad . \quad (8)$$

This shows that if the $Z_{ms} = (m\pi)^4 C_{ms}$ are found in the manner outlined in Ref. 1, then the reactions R_{rs} at the joints can be found as the sum of a finite series of trigonometrical functions, and hence bending moments may be found by taking moments. It may be observed that, for relation (8) to hold, the only conditions apart from those of the ordinary theory of uniform beams are that one set of beams (B) be simply-supported and the other set (A) equally spaced.

To obtain an expression for direct calculation of deflections or bending moments in beams B at the intersections, the procedure is as follows.

The right hand side of equation (6) is a periodic function of m which is unaltered if m be replaced by $v = |\, m+2jh \,|$, (j is any integer positive or negative), except for a change of sign if $m+2jh < 0$.

Hence
$$Z_{vs} = Z_{ms} \operatorname{sgn}(m+2jh) \quad . \quad . \quad . \quad . \quad (9)$$

where
$$\left.\begin{aligned} \operatorname{sgn}(t) &= +1, \quad t > 0 \\ &= -1, \quad t < 0 \end{aligned}\right\} \quad . \quad . \quad . \quad . \quad (10)$$

Then for $x = ra/h$, equation (1) becomes

$$w_{rs} = \sum_{k=1}^{\infty} C_{ks} \sin \frac{k\pi r}{h}.$$

Rearranging the terms in this series,

$$w_{rs} = \sum_{m=1}^{p} \sum_{j=-\infty}^{\infty} C_{vs} \sin \frac{m\pi r}{h} \operatorname{sgn}(m+2jh).$$

Using equation (9),

$$w_{rs} = \sum_{m=1}^{p} \sum_{j=-\infty}^{\infty} m^4 C_{ms} (m+2jh)^{-4} \sin \frac{m\pi r}{h}.$$

Now by the known result

$$\left.\begin{aligned} \sum_{j=-\infty}^{\infty} (m+2jh)^{-4} &= \frac{\pi^4}{48h^4}\left(1 + 3\cot^2 \frac{m\pi}{2h}\right) \operatorname{cosec}^2 \frac{m\pi}{2h} \\ &= \pi^4 K_m, \text{ say,} \end{aligned}\right\} \quad . \quad . \quad . \quad (11)$$

we obtain
$$w_{rs} = \sum_{m=1}^{p} K_m Z_{ms} \sin \frac{m\pi r}{h}. \quad . \quad . \quad . \quad (12)$$

Similarly, for bending moment in the B-beam at the joint (r, s),

$$M_{rs} = -EI_s \sum_{k=1}^{\infty} (k\pi/a)^2 C_{ks} \sin(k\pi r/h)$$

$$= -\frac{EI_s}{a^2} \sum_{m=1}^{p} \sum_{j=-\infty}^{\infty} v^2\pi^2 C_{vs} \sin(m\pi r/h) \operatorname{sgn}(m+2jh)$$

$$= -\frac{EI_s}{a^2} \sum_{m=1}^{p} \sum_{j=-\infty}^{\infty} m^4\pi^2 C_{ms} (m+2jh)^{-2} \sin(m\pi r/h)$$

$$= -\frac{EI_s}{4a^2h^2} \sum_{m=1}^{p} Z_{ms} \operatorname{cosec}^2(m\pi/2h) \sin(m\pi r/h) \quad . \quad . \quad . \quad (13)$$

using the summation $$\sum_{j=-\infty}^{\infty} (m+2jh)^{-2} = \frac{\pi^2}{4h^2} \operatorname{cosec}^2(m\pi/2h) \quad . \quad . \quad . \quad (14)$$

2.2. Second Case: Clamped Ends (Symmetrical in B-Direction)

In this case the appropriate series for deflection of the s^{th} beam of B, assuming symmetry about its centre, is

$$w_s = \sum_{k=1}^{\infty} C_{ks} [1 - \cos(2k\pi x/a)] \quad . \quad . \quad . \quad . \quad (15)$$

and, if no external load acts, the bending moment is given by

$$M_s = \tfrac{1}{2} \sum_{r=1}^{p} \left[-\frac{x_r^2}{a} - (x - x_r) + (x - x_r)\, U(x - x_r) + (x - a + x_r)\, U(x - a + x_r) \right] R_{rs} \quad (16)$$

Equating this to $EI_s d^2w/dx^2$, multiplying by $\cos(2m\pi x/a)$, and integrating with respect to x over $(0, a)$,

$$EI_s C_{ms} \left(\frac{2m\pi}{a}\right)^2 \frac{a}{2} = \sum_{r=1}^{p} R_{rs} \left(\frac{a}{2m\pi}\right)^2 \left(1 - \cos\frac{2m\pi x_r}{a}\right),$$

or for equally spaced A-beams,

$$EI_s Z_{ms} = \tfrac{1}{8} a^3 \sum_{r=1}^{p} R_{rs} \left(1 - \cos\frac{2m\pi r}{h}\right). \quad . \quad . \quad . \quad (17)$$

This shows that $Z_{ms} = 0$ if m is any multiple of h, and also that Z_{ms} remains the same if m be replaced by $(h-m)$.

Moreover, for $0 < m < h$ and $0 < n < h$,

$$2 \sum_{r=1}^{h-1} \left(1 - \cos\frac{2m\pi r}{h}\right) \cos\frac{2n\pi r}{h} \begin{cases} = -h \text{ if } m = n \text{ or } m + n = h \\ = -2h \text{ if } m = n = \tfrac{1}{2}h \\ = 0 \text{ for other values of } m \text{ and } n \end{cases} \quad (18)$$

Hence, from (17),

$$EI_s \sum_{m=1}^{p} Z_{ms} \cos \frac{2m\pi r}{h} = \tfrac{1}{8}a^3 \sum_{m=1}^{p} \sum_{t=1}^{p} R_{ts} \left(1 - \cos \frac{2m\pi t}{h}\right) \cos \frac{2m\pi r}{h}$$
$$= -\tfrac{1}{8}ha^3 R_{rs}, \quad . \quad . \quad . \quad . \quad . \quad . \quad (19)$$

using the property of symmetry, which implies that R_{rs} is unaltered when r is replaced by $h-r$.

The recurrence relation corresponding to equation (9) is

$$Z_{us} = Z_{ms},$$

where $u = |\, m + jh \,|$, and j is any integer, positive or negative. Thus, proceeding as before, the series for deflections at the intersections reduces to

$$w_{rs} = \sum_{m} L_m Z_{ms} \left(1 - \cos \frac{2m\pi r}{h}\right) \quad . \quad . \quad . \quad . \quad (20)$$

$$\text{where } L_m = \tfrac{1}{3}h^{-4} \left(1 + 3 \cot^2 \frac{m\pi}{h}\right) \operatorname{cosec}^2 \frac{m\pi}{h},$$

and the summation is from 1 to $\frac{1}{2}p$, if p is even, or from 1 to $\frac{1}{2}(p+1)$, with the final term halved, if p is odd. In either case the expression could be written

$$w_{rs} = \tfrac{1}{2} \sum_{m=1}^{p} L_m Z_{ms} \left(1 - \cos \frac{2m\pi r}{h}\right).$$

Similarly, for bending moments in the B-beams,

$$M_{rs} = \frac{2EI_s}{a^2h^2} \sum_{m=1}^{p} Z_{ms} \cos \frac{2m\pi r}{h} \operatorname{cosec}^2 \frac{m\pi}{h} \quad . \quad . \quad . \quad (21)$$

3. Solutions for a Particular Grillage

As an illustration of the method, consider a grillage of three equal uniform girders (B-beams) evenly spaced and of length a, supported by nine equal uniform stiffeners (A-beams) of length $b = \frac{1}{3}a$ and moment of inertia one quarter of that of the girders (*i.e.* $4I_r = I_s$). Then $p = 9$ and $q = 3$. We assume a central concentrated load P, and consider first all beams simply-supported, and, secondly, all beams clamped at the ends.

With simple-support, we have for the A-beams, by beam theory,

$$7b^3 R_{r1} = 6 \times 4^3 EI_r \,(-16w_{r1} + 11w_{r2})$$

$$7b^3 \,(R_{r2} - p\lambda_r) = 6 \times 4^3 EI_r \,(22w_{r1} - 16w_{r2}),$$

where $\lambda_5 = 1$ and $\lambda_r = 0$ for $r \neq 5$.

Substituting into equation (6), and replacing w_{r1} and w_{r2} by their series (12),

$$7b^3EI_sa^{-3}Z_{m1}=2\sum_{r=1}^{9}6\times4^3EI_r\sin\frac{m\pi r}{10}\sum_{n=1}^{9}K_n\sin\frac{n\pi r}{10}(-16Z_{n1}+11Z_{n2})$$

$$=6\times4^3EI_rK_m(-16Z_{m1}+11Z_{m2})\times10,$$

$$7b^3EI_sa^{-3}Z_{m2}=2\sum_{r=1}^{9}6\times4^3EI_r\sin\frac{m\pi r}{10}\sum_{n=1}^{9}K_n\sin\frac{n\pi r}{10}(22Z_{n1}-16Z_{n2})+7b^3\left(2P\sin\frac{m\pi}{2}\right)$$

$$=6\times4^3EI_rK_m(22Z_{m1}-16Z_{m2})\times10+14b^3P\sin\frac{m\pi}{2}.$$

Solving these two equations, putting $C=60\times4^3\ (I_ra^3)/(I_sb^3)=60\times4^2\times3^3$,

$$\frac{EI_s}{a^3}Z_{m1}=\frac{22PK_mC\sin(m\pi/2)}{7+32K_mC+2K_m^2C^2}$$

$$\frac{EI_s}{a^3}Z_{m2}=\frac{2(1+16K_mC)P\sin(m\pi/2)}{7+32K_mC+2K_m^2C^2}.$$

After evaluating these expressions for the appropriate values of m, one can determine R_{rs} and w_{rs} from (8) and (12), and M_{rs} from (3) for A-beams or from (13) for B-beams. Table I gives numerical values for deflection, bending moments and shearing forces at the centre of the grillage. The corresponding values obtained from a solution by relaxation (taken from an unpublished Admiralty report) are also given, for comparison.

TABLE I

NUMERICAL SOLUTIONS FOR THE PARTICULAR GRILLAGE. SIMPLY-SUPPORTED ENDS

Method of solution	*Finite series*	*Relaxation*
Central deflection	$7{\cdot}300\times10^{-4}\ Pa^3/(EI_s)$	$7{\cdot}308\times10^{-4}\ Pa^3/(EI_s)$
Central bending moment:		
(*i*) Girder (B-beam)	$-33{\cdot}22\times10^{-3}Pa$	$-33{\cdot}02\times10^{-3}Pa$
(*ii*) Stiffener (A-beam)	$-24{\cdot}12\times10^{-3}Pa$	$-24{\cdot}18\times10^{-3}Pa$
Central shearing force:		
(*i*) Girder	$-28{\cdot}46\times10^{-2}P$	$28{\cdot}54\times10^{-2}P$
(*ii*) Stiffener	$-21{\cdot}54\times10^{-2}P$	$-21{\cdot}62\times10^{-2}P$

The analysis for the same grillage with all beams clamped at the ends is as follows:—

Applying beam theory to the A-beams,

$$b^3R_{r1}=3\times4^3EI_r(-8w_{r1}+4w_{r2})$$

$$b^3(R_{r2}-\lambda_rP)=3\times4^3EI_r(8w_{r1}-5w_{r2}).$$

When substituted into (17), w_{rs} being replaced by means of (20), these two equations give

$$8EI_s t^{-3} b^3 Z_{m1} = 3 \times 4^3 EI_r \sum_{r=1}^{9} \tfrac{1}{2} \left(1 - \cos \frac{2m\pi r}{10}\right) \sum_{n=1}^{9} L_n \left(1 - \cos \frac{2n\pi r}{10}\right) (-8Z_{n1} + 4Z_{n2})$$

$$= 3 \times 4^3 EI_r \left[5 \sum_{n=1}^{9} L_n (-8Z_{n1} + 4Z_{n2}) + 5L_m (-8Z_{m1} + 4Z_{m2}) \right]$$

$$8EI_s a^{-3} b^3 Z_{m2} - b^3 P (1 - \cos m\pi)$$

$$= 3 \times 4^3 EI_r \sum_{r=1}^{9} \tfrac{1}{2} \left(1 - \cos \frac{2m\pi r}{10}\right) \sum_{n=1}^{9} L_n \left(1 - \cos \frac{2n\pi r}{10}\right) (8Z_{n1} - 5Z_{n2})$$

$$= 3 \times 4^3 EI_r \left[5 \sum_{n=1}^{9} L_n (8Z_{n1} - 5Z_{n2}) + 5L_m (8Z_{m1} - 5Z_{m2}) \right],$$

which may be written

$$\left.\begin{aligned} (1 + 8N_m) Z_{m1} - 4N_m Z_{m2} &= -8S_1 + 4S_2 \\ -8N_m Z_{m1} + (1 + 5N_m) Z_{m2} &= \frac{a^3 P}{8EI_s} (1 - \cos m\pi) + 8S_1 - 5S_2) \end{aligned}\right\} \quad . \qquad (22)$$

where $N_m = 120\, a^3 b^{-3} (I_r / I_s) L_m = 810\, I_{.m}$,

$$P_m = \frac{a^3 P}{8EI_s} (1 - \cos m\pi),$$

and $$S_s = \sum_{n=1}^{9} N_n Z_{ns}.$$

From equations (22),

$$\left.\begin{aligned} \Delta_m Z_{m1} &= 4N_m P_m - 8 (1 + N_m) S_1 + 4S_2 \\ \Delta_m Z_{m2} &= (1 + 8N_m) P_m + 8S_1 - (5 + 8L_m) S_2 \end{aligned}\right\} \quad . \quad . \quad . \qquad (23)$$

where $\Delta_m = 1 + 13N_m + 8N_m^2$.

Multiplying these equations by $N_m \Delta_m^{-1}$ and summing with respect to m from 1 to 9 gives

$$S_1 = \sum_{m=1}^{9} [4N_m P_m - 8 (1 + N_m) S_1 + 4S_2] \Delta_m^{-1} N_m$$

$$S_2 = \sum_{m=1}^{9} [(1 + 8N_m) P_m + 8S_1 - (5 + 8L_m) S_2] \Delta_m^{-1} N_m.$$

The solution of these equations is given by

$$\left.\begin{aligned} AS_1 &= 4A_1A_3 + 4(1 + 13A_1 + 8A_2)A_4 \\ AS_2 &= (1 + 8A_1 + 8A_2)A_3 + 8(1 + 12A_1 + 8A_2)A_4 \end{aligned}\right\} \qquad (24)$$

where $A_1 = \sum_{m=1}^{9} N_m \Delta_m^{-1}$; $A_2 = \sum_{m=1}^{9} N_m^2 \Delta_m^{-1}$;

$A_3 = \sum_{m=1}^{9} P_m N_m \Delta_m^{-1}$; $A_4 = \sum_{m=1}^{9} P_m N_m^2 \Delta_m^{-1}$;

$$A = 1 + 13A_1 + 16A_2 + 8A_1^2 + 104A_1A_2 + 64A_2^2.$$

It is then necessary to substitute from (24) into (23) and thence into equation (19), (20), or (21) to obtain respectively forces, deflections or bending moments in B-beams at the intersections. Numerical results for this case are included in Table II.

TABLE II

NUMERICAL SOLUTIONS. CLAMPED ENDS

Method of solution	*Finite series*	*Relaxation*
Central deflection	$2{\cdot}674 \times 10^{-4}\, Pa^3/(EI_s)$	$2{\cdot}678 \times 10^{-4}\, Pa^3/(EI_s)$
Central bending moment:		
(*i*) Girder	$-25{\cdot}54 \times 10^{-3} Pa$	$-25{\cdot}52 \times 10^{-3} Pa$
(*ii*) Stiffener	$-16{\cdot}84 \times 10^{-3} Pa$	$-16{\cdot}87 \times 10^{-3} Pa$
Central shearing force:		
(*i*) Girder	$-26{\cdot}91 \times 10^{-2} P$	$-26{\cdot}891 \times 10^{-2} P$
(*ii*) Stiffener	$-23{\cdot}09 \times 10^{-2} P$	$-23{\cdot}127 \times 10^{-2} P$

4. Conclusion

As originally presented by Klitchieff, the solution was obtained in the form of infinite Fourier series and, for bending moments, direct numerical evaluation was tedious if not impossible, owing to the slow convergence of the series. It may be seen that computation is made shorter by the modification in the present paper; for instance, the example requires the determining of the coefficients Z_{ms} as far as the first five only.

Acknowledgment

This paper is published with the approval of the Lords Commissioners of the Admiralty, but the responsibility for any statements of fact or opinions expressed rests solely with the author.

References

1. Klitchieff, J. M. Beams on Elastic Supports and on Cross Girders. *The Aeronautical Quarterly*, Vol. II, pp. 157-66, November 1950.

2. Klitchieff, J. M. Beams on Cross Girders with Clamped Ends. *The Aeronautical Quarterly*, Vol. III, pp. 230-7, November 1951.

An Approximate Method for the Calculation of Turbulent Boundary Layers in Diffusers

J. F. NORBURY, M.Eng., A.F.R.Ae.S.

(Department of Fluid Mechanics, University of Liverpool)

SUMMARY: An approximate method is described for the calculation of turbulent boundary layers in which the turbulence is developed before the commencement of the adverse pressure gradient, as in most diffuser layers. It is based on a method due to Spence[2] which has been modified and also extended to the calculation of three-dimensional diverging layers such as occur in ducts whose breadth is increasing. The velocity profiles occurring in a diverging layer are examined and it is shown that the inner part obeys the universal logarithmic law, as in two-dimensional layers. This result is used to obtain an equation for the form parameter $\gamma=(u/U)_{y=\theta}$ in diverging layers, by substitution in the equation of motion and incorporation of the equations of momentum and continuity for diverging flow. The form parameter equation contains a term involving the gradient of shear stress at $y=\theta$ and values of this term are obtained by the analysis of experimental data and the substitution of known values for all the other terms in the form parameter equation. Values of the term involving shear stress gradient are then correlated in terms of known boundary layer quantities, and the resulting correlation allows the formulation of a step-by-step method for the solution of the form parameter equation. This may be used in conjunction with the momentum equation to predict the boundary layer growth. It was not found possible to effect a satisfactory correlation for boundary layers on lifting aerofoils, in which the turbulence develops within the adverse pressure gradient, and the method cannot be used for the prediction of such layers. The results of a number of calculations are given.

1. Introduction

In recent years a number of investigators have considered the problem of calculating the growth of turbulent boundary layers. The mechanism of such a layer is very complex and is not by any means fully understood. Thus a completely theoretical treatment is not at present possible, and the semi-empirical approach is difficult.

The problem is complicated by the variety of conditions which may occur at the beginning of the turbulent layer. In boundary layers on aerofoils, the transition to turbulence may follow an instability of the laminar layer or a bubble of separated flow. The development of the turbulence is presumably dependent on the severity of the adverse pressure gradient in the transition region, and it seems

Originally received February 1955.

possible that the nature of the transition influences the subsequent growth of the layer for a considerable distance. In diffuser flows the boundary layer is usually turbulent at the throat, but its thickness and velocity profile, and the state of the turbulent motion, depend on upstream conditions and may vary considerably.

Usually the object of a boundary layer calculation is the determination of the momentum thickness θ and the velocity profile form parameter H, the product $H\theta$ giving the displacement thickness δ^*. The principal difficulty lies in the determination of H. For typical applications this is not required to a high degree of accuracy, and any method which would unfailingly predict H within five per cent would probably be adequate. Such an accuracy cannot yet be attained.

The present work arose from a desire to analyse boundary layers occurring in a diffuser of rectangular section and to assess the possibility of calculating the growth of the boundary layers along the centre line of each wall. The roof and floor of the diffuser were plane and parallel, and the side walls were flexible and could be moved to vary the pressure gradient. Thus the boundary layers on the side walls might be expected to be two-dimensional over the early part of the diffuser, where all the layers were relatively thin, and the flow in the boundary layers on the roof and the floor was divergent.

Two recent methods for the calculation of turbulent boundary layers were considered. That due to Rubert and Persh[1] depends on the kinetic energy equation and the assumption of power law velocity profiles for the formulation of an equation for H. It was applied in the original paper to the calculation of both two-dimensional layers and three-dimensional layers occurring in conical diffusers. However, calculations by this method did not correspond very well with the experimental measurements in the present case, the disparity being especially marked in the case of the three-dimensional layers. The method due to Spence[2] is based on the proposition that the velocity profiles can be expressed by means of the logarithmic law over the inner part and a power law over the outer part. This appears to be fairly satisfactory and the method is convenient to use, but in its original form there are features which render it unsuitable for calculations of diffuser boundary layers. Modifications are here presented to avoid these difficulties, and the method has been extended to the calculation of the three-dimensional diverging boundary layers occurring in the diffuser.

NOTATION

x, y	co-ordinates parallel and normal to bounding plane of flow
u, v	mean velocity components in x, y, -directions
U	free stream velocity at edge of boundary layer
μ, ρ, ν	viscosity, density, kinematic viscosity
τ, τ_w	shear stress, shear stress at wall
c_f	local skin friction coefficient $= \tau_w/(\frac{1}{2}\rho U^2)$
u_τ	friction velocity $= (\tau_w/\rho)^{\frac{1}{2}} = U\,(c_f/2)^{\frac{1}{2}}$

δ thickness of boundary layer

$\delta^* = \int_0^\delta \left(1 - \frac{u}{U}\right) dy$, displacement thickness of boundary layer

$\theta = \int_0^\delta \frac{u}{U}\left(1 - \frac{u}{U}\right) dy$, momentum thickness of boundary layer

$\theta^* = \theta u_\tau / \nu$

$H = \delta^* / \theta$

$\gamma = (u/U)_{y=\theta}$ } form parameters for velocity profile

$R_\theta = U\theta/\nu$, Reynolds number based on momentum thickness

$y^* = yu_\tau/\nu$

α_s, k_s constants occurring in Spence's method

$\chi(\gamma)$ function occurring in Spence's method

X distance expressing the divergence rate of a three-dimensional diverging layer

f function for inner part of velocity profile

F, g, G_1, G_2 functions occurring in form parameter equation and defined in equations (12), (14), and (16)

k quantity defined in equation (11)

$\overline{U} = U/U_0$

Suffixes

0 refers to initial values

d refers to three-dimensional diverging layer

2. Outline of Spence's Method

It is required to calculate the variation of θ, H, δ^* and τ_w along the length of the boundary layer. The four equations used are

(*i*) the boundary layer momentum equation,

(*ii*) the relationship $H = \delta^*/\theta$,

(*iii*) an empirical equation for $\tau_w/(\frac{1}{2}\rho U^2)$,

(*iv*) an equation for the variation of the form parameter H derived from the equation of motion.

To obtain the fourth equation, Spence[2] introduced as basic form parameter the quantity γ defined as the ratio of velocity at distance θ from the wall to the main stream velocity U.

For a power law profile

$$\gamma = \left[\frac{H-1}{H(H+1)}\right]^{\frac{H-1}{2}} \quad . \quad . \quad . \quad . \quad . \quad (1)$$

and, as this relation is nearly correct for experimentally measured layers, it is used in the subsequent work. A differential equation for the variation of γ along the layer was obtained by substitution in the equation of motion of the logarithmic law for velocity distribution near the wall,

$$\frac{u}{U} = \frac{u_\tau}{U}\left[2{\cdot}5 \log_e\left(\frac{u_\tau}{U}\frac{U_y}{\nu}\right) + 5{\cdot}5\right] \quad . \quad . \quad . \quad . \quad (2)$$

This differential equation involved the gradient of the shear stress at a distance θ from the wall, $(\partial\tau/\partial y)_{y=\theta}$. No theory exists by which this quantity might be predicted and it is difficult to determine experimentally. Spence introduced the relation

$$\frac{\partial}{\partial y}\left(\frac{\tau}{\rho U^2}\right)_{y=\theta} = -\alpha_s(1 - 2k_s\gamma - \gamma^2)\frac{U'}{U} \quad . \quad . \quad . \quad (3)$$

and then determined the constants α_s and k_s so that his form parameter equation gave a good fit with experimental results. He then reduced the form parameter equation to a more convenient form in which it may be used in conjunction with the momentum equation to calculate the boundary layer growth by an iterative process.

In attempting to apply the method to the calculation of boundary layers in diffusers, difficulties arise on two points, namely the assumptions regarding the shear stress gradient and the choice of the initial value of H. In the throat of a diffuser $U'/U = 0$ and, in general,

$$\frac{\partial}{\partial y}\left(\frac{\tau}{\rho U^2}\right)_{y=\theta} \neq 0.$$

Thus α_s becomes infinite and, in the neighbourhood of the throat, where U'/U is small, α_s will still be considerably different from any constant value which may be suitable over the greater part of the layer. The choice of a suitable initial value for H is important for satisfactory calculations. For aerofoils, Spence indicated that a constant initial value, actually 1·4, gave good results in the calculation of layers having free transition. For a diffuser, the initial value of H may vary between wide limits, and it is not possible to assume a fixed value. If the initial value of H is very low the Spence method is inapplicable. The function

$$\chi(\gamma) = 1{\cdot}797\,(1{\cdot}22 + \gamma)^{1{\cdot}017}\,(0{\cdot}82 - \gamma)^{0{\cdot}683}. \quad . \quad . \quad . \quad (4)$$

which appears in the final form of Spence's form parameter equation actually has no real values for $\gamma > 0{\cdot}82$, corresponding to $H < 1{\cdot}14$. In fact values of H less than 1·14 may occur at diffuser throats and such cases could not be dealt with.

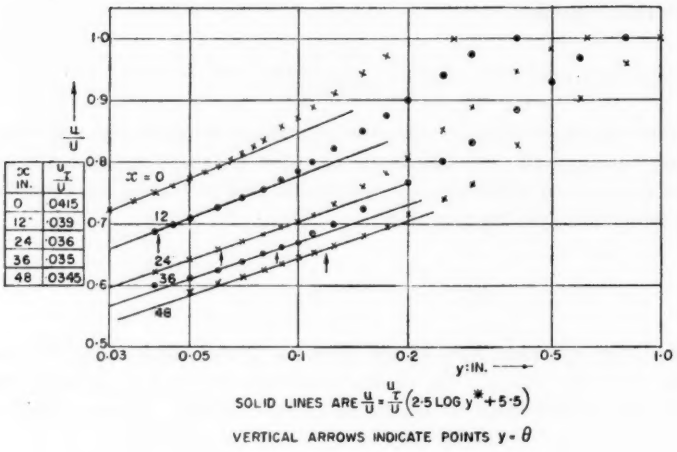

Fig. 1.
Velocity profiles in diverging flow plotted logarithmically.

3. Velocity Profiles in Diverging Boundary Layers

For two-dimensional layers, Spence showed that in an adverse gradient the inner part of the velocity profiles could be expressed by the logarithmic law, equation (2), and further that the values of the parameter (u_τ/U) required for correspondence were approximately equal to the values of $(c_f/2)^{\frac{1}{2}}$ $(=u_\tau/U$ by definition) given by the skin friction relations of Ludwieg and Tillmann[3] and, for low values of H, of Squire and Young[4]. These relations are, respectively,

$$c_f = 0{\cdot}246 \times 10^{-0{\cdot}678H} \times R_\theta^{-0{\cdot}268} \quad . \quad . \quad . \quad . \quad (5)$$

$$\text{and } c_f = 2\,(3{\cdot}59 + 2{\cdot}56 \log_e R_\theta)^{-2} \quad . \quad . \quad . \quad . \quad (6)$$

A similar investigation has been made for a three-dimensional diverging layer occurring in a diffuser, the velocity profiles having been measured along the axis of symmetry of the layer. The validity of the logarithmic law over the inner part, approximately one-fifth of the layer, is shown by the results plotted in Fig. 1. No reliable measurements of the skin friction coefficients for the layer were made, so that it was not possible to make a direct check of the accuracy of equation (2). The course adopted was to assume that equation (2) was valid for the three-dimensional flow, and then to compare the resulting values of (u_τ/U) with $(c_f/2)^{\frac{1}{2}}$ given by the skin friction relations for two-dimensional flows with equal values of R_θ and H. In fact the results showed a close resemblance to those obtained for the two-dimensional layers. The values of u_τ/U indicated by the velocity profiles fell slightly below those given by the Squire-Young relation (Fig. 2). For the

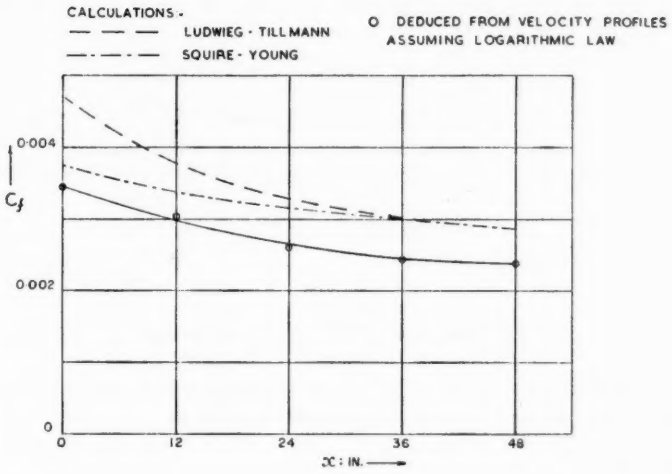

Fig. 2.
Variation of skin friction in diverging flow.

Ludwieg-Tillmann relation the disparity was greater over the early part of the layer, where the values of H were rather low, being about 1·25.

In addition the relation between γ and H for the diverging layers corresponded closely with that given by the power law, the order of disparity being the same as that for two-dimensional layers.

4. Form Parameter Equation for Three-Dimensional Diverging Flow

We are considering flow over a plane boundary in which the streamlines diverge away from some central axis of symmetry, and we require an equation expressing the variation of the form parameter equation along the axis of symmetry. This is taken to be the x-axis, the y-axis being at right angles to the plane boundary. u and v are the corresponding velocity components. The streamline divergence rate is conveniently expressed by the distance, X, from the section considered to the point of intersection of the x-axis and a tangent to the streamline at the section (Fig. 3). In general the streamlines are curved, so that X will vary along the length of the layer, and at any particular section it may also have different values for streamlines at different distances from the axis of symmetry. The required value of X is the value which is approached for streamlines approaching the axis of symmetry.

In the laminar sub-layer,

$$\frac{u}{u_\tau} = \frac{yu_\tau}{\nu},$$

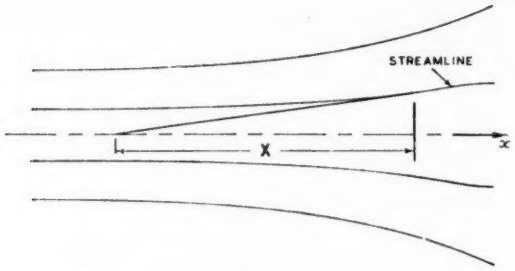

Fig. 3.
Determination of X from streamline pattern.

and just outside this is a region in which the logarithmic law, equation (2), is valid. The momentum thickness θ lies within this region (Fig. 1).

Thus near the wall,

$$\frac{u}{u_\tau} = f(y^*) \qquad \text{where} \qquad y^* = \frac{yu_\tau}{\nu}.$$

The continuity equation for the type of flow considered is

$$\frac{\partial u}{\partial x} + \frac{\partial v}{\partial y} + \frac{u}{X} = 0, \qquad . \quad . \quad . \quad . \quad (7)$$

while the equation of motion in the direction of the x-axis for steady flow is the same as for two-dimensional flow,

$$u\frac{\partial u}{\partial x} + v\frac{\partial u}{\partial y} = U\frac{dU}{dx} + \frac{1}{\rho}\frac{\partial \tau}{\partial y} \qquad . \quad . \quad . \quad . \quad (8)$$

The momentum equation becomes

$$\frac{\theta'}{\theta} + (H+2)\frac{U'}{U} = \frac{1}{\theta}\left(\frac{u_\tau}{U}\right)^2 - \frac{1}{X} \qquad . \quad . \quad . \quad . \quad (9)$$

Writing out the equation of motion at $y=\theta$, and using equations (2), (7), and (9), we obtain

$$\gamma'\gamma - \frac{U'}{U}[1 - 2k\gamma - \gamma^2] = \frac{2{\cdot}5\gamma}{\theta}\left(\frac{u_\tau}{U}\right)^3 - 2{\cdot}5\ \frac{u_\tau}{U}\frac{\gamma}{X} + \left(\frac{u_\tau}{U}\right)^2 \frac{F(\theta^*)}{X}, \qquad . \quad (10)$$

$$\text{where} \qquad 2k\gamma = \frac{-\dfrac{\partial}{\partial y}\left(\dfrac{\tau}{\rho}\right)_{y=\theta}}{UU'} + 2{\cdot}5\frac{u_\tau}{U}(H+2)\gamma, \qquad . \quad . \quad . \quad (11)$$

$$\text{and} \qquad F(\theta^*) = f'(\theta^*)\int_0^{\theta^*} f\, dy^* \qquad . \quad . \quad . \quad . \quad . \quad . \quad (12)$$

Regarding $y^* = 11{\cdot}7$ as the outer limit of the laminar sub-layer, we find

$$F(\theta^*) = 2{\cdot}5\left(\frac{U\gamma}{u_\tau}\right) - 6{\cdot}25 - \frac{96}{R_\theta \frac{u_\tau}{U}} \quad . \quad . \quad . \quad . \quad (13)$$

Introducing also the function

$$g(k, \gamma) = (1-k-\gamma)^{1-k}(1+k+\gamma)^{1+k}, \quad . \quad . \quad . \quad . \quad (14)$$

equation (10) becomes

$$\frac{d}{dx}(\overline{U}^2 g) = \overline{U}^2\left[-G_1\frac{1}{\theta}\left(\frac{u_\tau}{U}\right)^3 - G_2\frac{U'}{U} + \frac{G_2}{k^2}\frac{1}{X}\left(\frac{u_\tau}{U}\right)^2\left\{6{\cdot}25 + \frac{96}{R_\theta \frac{u_\tau}{U}}\right\}\right] \quad (15)$$

where $$G_1 = 5\gamma\left(\frac{1+k+\gamma}{1-k-\gamma}\right)^k \quad \text{and} \quad G_2 = 2k^2\left(\frac{1+k+\gamma}{1-k-\gamma}\right)^k \quad . \quad . \quad (16)$$

For two-dimensional layers $X = \infty$ and the form parameter equation becomes

$$\frac{d}{dx}(\overline{U}^2 g) = \overline{U}^2\left[-G_1\frac{1}{\theta}\left(\frac{u_\tau}{U}\right)^3 - G_2\frac{U'}{U}\right] \quad . \quad . \quad . \quad (17)$$

Curves of the functions g, G_1 and G_2 for various values of H and k are given in Figs, 6, 7, and 8. Tables of values have been calculated but are not presented here.

5. Calculation of Two-Dimensional Layers

5.1. Introduction and Correlation of Experimental Data

Since the product $(u_\tau/U)(H+2)$ changes little over most of the layer, the variation of the quantity k, defined in equation (11), depends largely on the shear stress gradient at $y = \theta$. The variation of k for a number of experimental layers was found by the substitution of experimental data in the two-dimensional form of equation (10), the Squire-Young relation being used for the calculation of u_τ/U. The following series of layers was analysed:—

(*a*) Schubauer and Klebanoff[5],

(*b*) McCullough and Gault[6]. Boundary layers on N.A.C.A. 63_3-018 at 0°, 6°, 12° incidence, and on N.A.C.A. 63_1-012 at 12·8°,

(*c*) Altman and Hayter[7]. Unswept wing at $C_L = 0$, 0·32 and 1·0.

(*d*) von Doenhoff and Tetervin[8]. Nose-opening aerofoil, shape 13, 9·1° incidence, and N.A.C.A. 65 (216)-222 at 10·1°.

(*e*) Measurements made by the author in a diffuser of rectangular section.

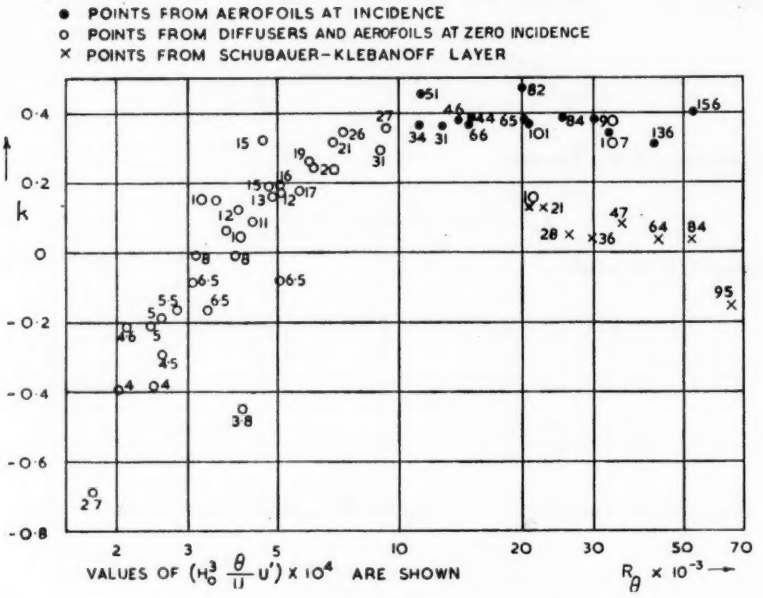

Fig 4.
Values of k from experimental data.

An attempt was made to correlate the values of k which were obtained, in terms of known boundary layer quantities. After preliminary trials the two parameters chosen for the correlation were R_θ and $H_0^3\,\theta U'/U$.

(H_0 is the initial value of H. For those layers in which transition was complete before the adverse pressure gradient began, the initial value was taken to be that at the minimum pressure point. For the layers on aerofoils at incidence, where the end of the transition region was not clearly defined, the initial value was taken to be that value for which $dH/dx=0$). Values of k were plotted against R_θ, and the resulting distribution of points is shown in Fig. 4, where also the value of $H_0^3\,(\theta U'/U)$ for each point is given. Negative values of k were obtained in some cases from points near the start of the adverse pressure gradient. It may be supposed that at such sections the maximum shear stress lies closer to the wall than the distance $y=\theta$, so that $(\partial\tau/\partial y)_{y=\theta}$ is negative.

It appeared that the manner in which k varied was different for two distinct groups of layers; namely, those in which transition was probably complete before the commencement of the adverse pressure gradient (the Schubauer-Klebanoff layer, the diffuser layers, and those on aerofoils at zero incidence), and those in which transition occurred within the adverse pressure gradient, as on the aerofoils at incidence. Points obtained from the latter group could not be correlated by the

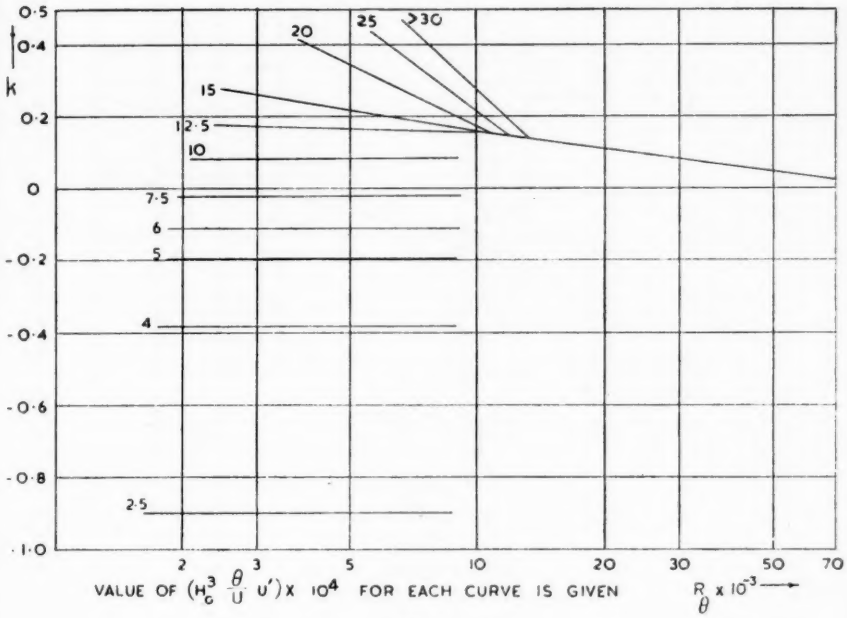

Fig. 5.
k—correlation chart.

parameters used and this applied to points derived from the downstream parts of the layers as well as to those from the parts nearer to the minimum pressure position. It is possible that the lack of correlation of the values of k from such layers reflects the complex nature of events in the transition region, and it suggests that the nature of the transition influences the whole subsequent behaviour of the turbulent layer.

For the diffuser layers, on the other hand, the values of k were correlated reasonably well. It was possible to draw lines of constant $H_0^3 (\theta U'/U)$ on the diagram of k against R_θ, and the resulting chart (Fig. 5) could then be used to determine k for boundary layer calculations. It is difficult to understand the physical significance of the parameter $H_0^3 (\theta U'/U)$, and the correlation of k values must be regarded as purely empirical.

5.2. Method of Calculation

Before calculating the variation of the form parameter the momentum equation must first be solved, using $H =$ constant, H_0, to obtain a first approximation for θ. This may conveniently be carried out by the method described by Spence[2]. The quantities θ, $\overline{U}^2$, U'/U, R_θ, $(1/\theta)(u_\tau/U)^3$ and $\theta U'/U$ are then obtained for all points of the layer. The terms R_θ, $H_0^3 (\theta U'/U)$, $(1/\theta)(u_\tau/U)^3$, and U'/U may then be plotted and equation (17) may be solved step by step. The term

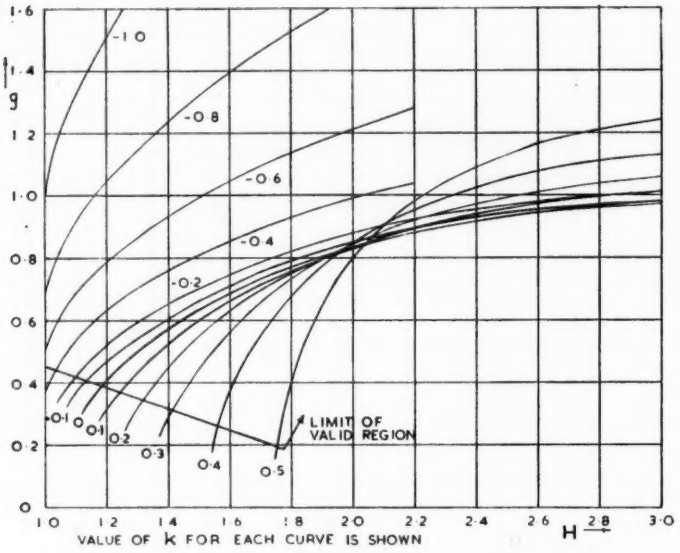

Fig. 6.
Curves of function $g(k, H)$.

on the right of the equation is small by comparison with $\overline{U}^2 g$, and over the greater part of the boundary layer large steps may be taken. The size of the step allowable may be determined by the rate at which k varies, if this is rapid. Over most of the layer k varies only slowly.

The procedure to be followed for each step is:—

(*i*) Choose size of step, Δx. Determine mid-step values of R_θ and $H_0^3(\theta U'/U)$.

(*ii*) Select k from chart (Fig. 5).

(*iii*) Knowing k and H, find g from curves (Fig. 6) and hence $\overline{U}^2 g$ at beginning of step.

(*iv*) Find mid-step values of $(1/\theta)(u_\tau/U)^3$ and U'/U. Find G_1 and G_2 from curves (Figs. 7 and 8). Hence find $\dfrac{d}{dx}(\overline{U}^2 g)$ for the step.

(*v*) $\Delta\overline{U}^2 g = \dfrac{d}{dx}(\overline{U}^2 g)\,\Delta x$.

(*vi*) Find $\overline{U}^2 g$ and hence g and H at end of step.

When the form parameter equation has been solved, a second solution of the momentum equation, using the known variation of H, may be obtained, again using Spence's method[2]. This will usually complete the boundary layer calculation to a sufficient degree of accuracy, but further solutions for H and θ may be obtained if necessary.

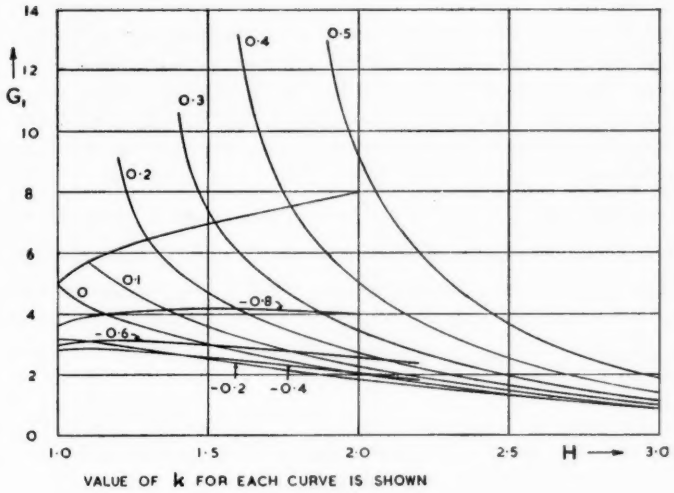

Fig. 7.
Curves of function $G_1(k, H)$.

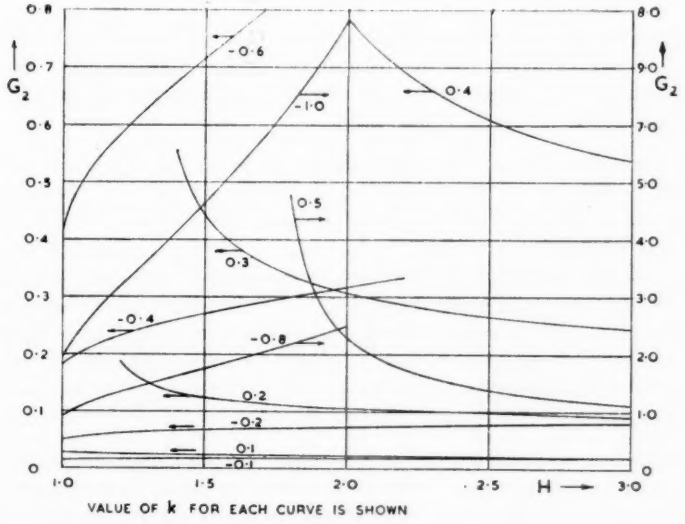

Fig. 8
Curves of function $G_2(k, H)$.

Throughout the calculation it is convenient to use the Squire and Young expression for skin friction, rather than that of Ludwieg and Tillmann. For the solution of the momentum equation the difference between the two relations is small, except near separation, when the skin friction term is no longer very important. In any case the higher value given by Squire and Young helps to offset the omission, in the usual form of the momentum equation, of terms arising from the boundary layer turbulence.

Two further points arising in the derivation and use of the method remain to be dealt with. In obtaining the derivative $\frac{d}{dx}(\bar{U}^2 g)$ it was assumed that k was independent of x. This condition is satisfied for each individual step.

The function $$g(k, \gamma) = (1 - k - \gamma)^{1-k}(1 + k + \gamma)^{1+k} \quad . \quad . \quad . \quad . \quad (14)$$

becomes zero when $\gamma = 1 - k$, and for $\gamma > 1 - k$ it has no real values. In practice it was found that the use of values of g in the neighbourhood of zero gave unreliable results, and on the g, H-chart (Fig. 6) a line was drawn to indicate the boundary of this region. If the k-correlation chart indicates the use of a (g, H) point falling below the line, the procedure is to choose the next lower value of k for which a curve is available, and for which the initial value of g for the step falls above the line. This procedure is not often necessary and must be regarded as a secondary correlation for k which over-rides the normal one for low values of H.

5.3. Discussion of Calculations and Results

The results of some typical calculations of H are shown in Figs. 9-14. The several quantities required in the calculation were taken directly from experimental data and not from a first solution of the momentum equation. Not more than ten steps were used for any of the calculations.

The layer on a symmetrical aerofoil at zero incidence was calculated by the methods of Spence and of Rubert and Persh, as well as by the present method, and the results are compared in Fig. 9. There is considerable scatter of the experimental points and it is not easy to choose a starting point. Curves from $H_0 = 1{\cdot}34$ and $1{\cdot}35$ calculated by the present method enclose a mean path through the points, and indicate the influence of a small variation in H_0. The Rubert and Persh result lies appreciably below the experimental points although it was begun at a higher initial value. The negative slope of the Spence result over the early part of the layer is indicative of the difficulty occurring in this method in a region of low pressure gradient.

Figure 10 shows a calculation for a layer on one wall of a rectangular section diffuser. Over the early part, where the boundary layer is thin and may be expected to be two-dimensional, the correspondence is good. At about half the distance along the layer the effect of interference of the boundary layers on the adjacent walls is apparent and this influence increases steadily. In Fig. 11 is shown

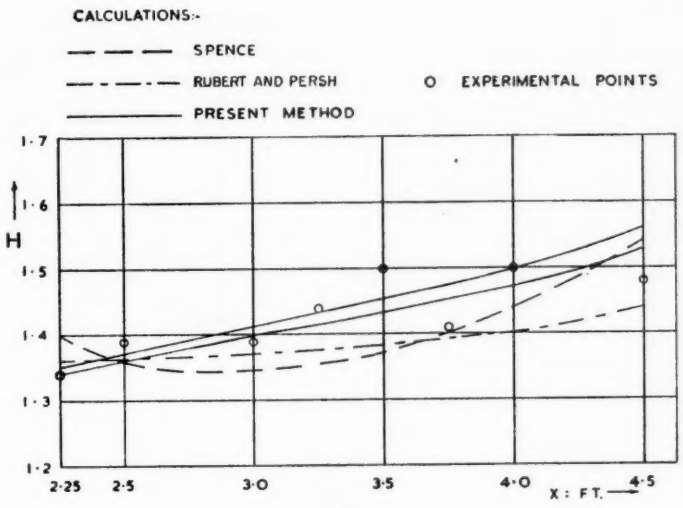

Fig. 9.
Growth of H on N.A.C.A. 63_3-018 at 0° (Ref. 6).

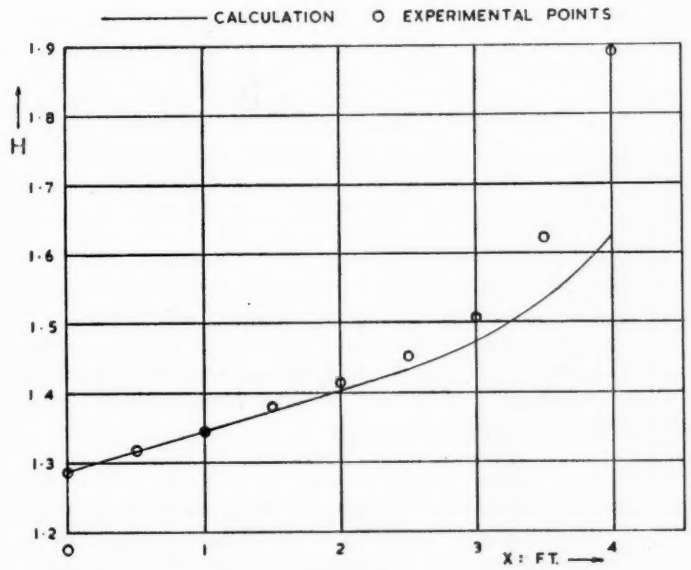

Fig. 10.
Growth of H on wall of rectangular section diffuser.

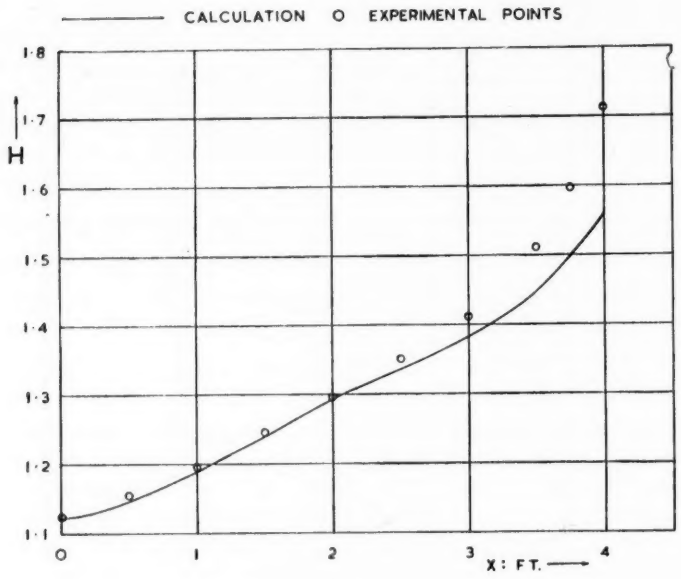

Fig. 11.
Growth of H on wall of rectangular section diffuser. Layer artificially thickened upstream of throat.

the result of a calculation of a similar layer which was artificially thickened upstream of the diffuser throat so that it had a very low initial value of H. In calculating this layer the k value had to be modified for several steps to avoid the invalid region of the g, H-chart (Fig. 6). However, the calculation is successful up to the point at which three-dimensional effects become apparent.

The result for the Schubauer-Klebanoff layer is shown in Fig. 12. Since this experimental layer completely determined the form of the k-correlation chart for $R_\theta > 20{,}000$, the calculation must be expected to yield a good result. Calculations were made from two starting points, $H_0 = 1{\cdot}30$ and $1{\cdot}35$, to illustrate the influence of the initial H value on the result for a separating layer. Clearly an initial point can be chosen somewhere between these limits to give very good correspondence between calculated and experimental results.

The result of a calculation for a layer on a plane wall investigated by Sandborn[9] is shown in Fig. 13 and compared with a calculation by the method of Maskell[10]. It is interesting that the two calculations correspond so closely, although the correspondence with the experimental results is not so close. Actually the boundary layer occupied a large part of the depth of the duct, and there is reason to doubt whether it was truly two-dimensional.

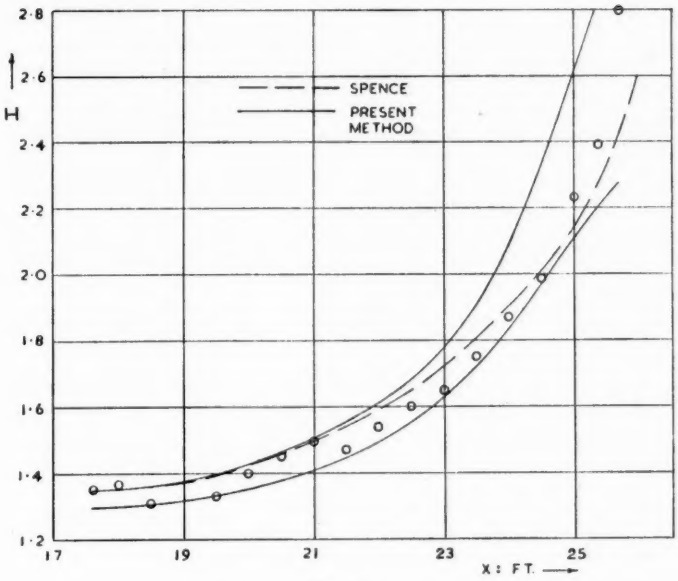

Fig. 12.
Growth of H for Schubauer-Klebanoff layer.

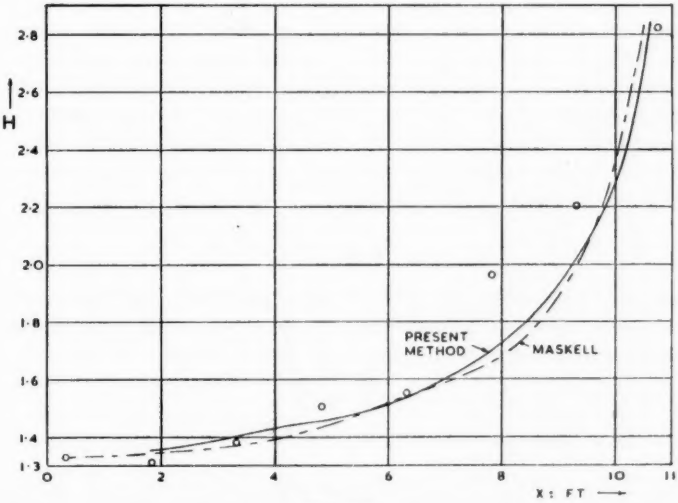

Fig. 13.
Growth of H for Sandborn layer (25 in. suction).

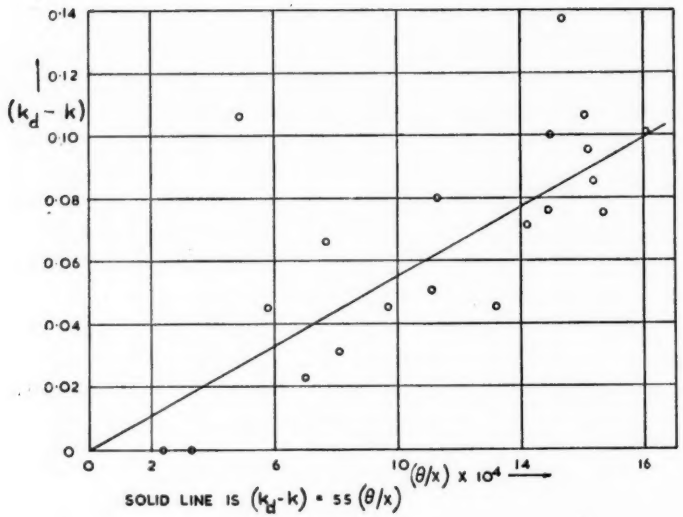

Fig. 14.
$(k_d - k)$ plotted against θ/X.

6. Calculation of Three-Dimensional Diverging Boundary Layers

6.1. Correlation of Experimental Data

For the purpose of analysing the diverging boundary layers occurring in the rectangular diffuser, the divergence rate, expressed by the distance X, was found by plotting the streamline pattern for potential flow using an electrical method. Values of k_d for the layers were then worked out from equation (10). (The suffix "d" distinguishes values of k relating to diverging layers). These values were slightly but systematically higher than the values indicated by the k-chart for two-dimensional layers having the same values of R_θ and $H_0^3\,(\theta U'/U)$. The differences $(k_d - k)$, were plotted against corresponding values of θ/X (Fig. 14). A roughly linear relationship was indicated, points being scattered about the line

$$k_d - k = 55\,\theta/X \qquad . \quad . \quad . \quad . \quad . \quad (18)$$

Since the maximum difference was only 0·1, this line was quite adequate to determine the correction to be applied to the two-dimensional value for the purpose of calculating three-dimensional layers.

6.2. Method of Calculation and Results

The form parameter equation to be solved is

$$\frac{d}{dx}(\overline{U}^2 g) = \overline{U}^2 \left[-G_1 \frac{1}{\theta}\left(\frac{u_\tau}{U}\right)^3 - G_2 \frac{U'}{U} + \frac{G_2}{k_d^2}\frac{1}{X}\left(\frac{u_\tau}{U}\right)^2 \left\{ 6{\cdot}25 + \frac{96}{R_\theta \dfrac{u_\tau}{U}} \right\} \right] \qquad (15)$$

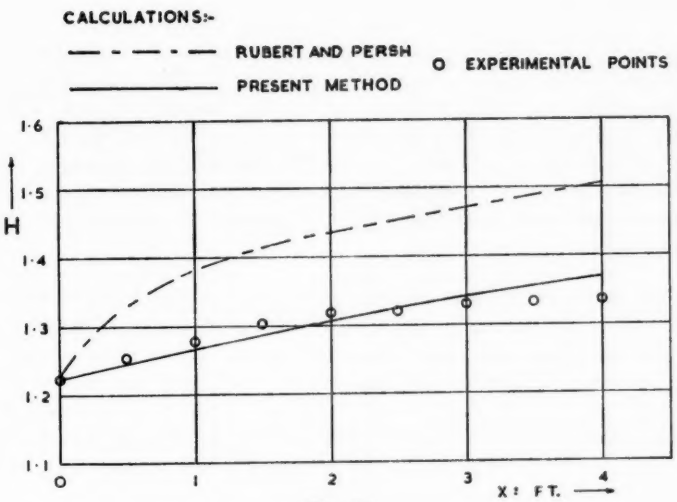

Fig. 15.
Growth of H for diverging layer in rectangular section diffuser.

For all but small values of θ, $96/(R_\theta u_\tau/U)$ is much smaller than 6·25, and when θ is small the third term on the right hand side is much less important than the first, which itself is small compared with $\overline{U}^2 g$. Thus the calculation may be simplified without loss of accuracy by writing the third term

$$6{\cdot}25\,\frac{G_2}{k_d^2}\,\frac{1}{X}\left(\frac{u_\tau}{\overline{U}}\right)^2 .$$

G_2/k_d^2 can be determined from the curves for G_2 and the known value of k_d. It must be noted, however, that as k_d approaches zero, G_2 approaches zero, while G_2/k_d^2 approaches 2.

Apart from taking account of this third term, the calculation differs from that for two-dimensional layers, described in Section 5.2, in only one feature. In step (*ii*), after selecting k from the k-chart (Fig. 5), the correction for divergence, $+55\,\theta/X$, must be applied. Since the primary correlation of k is slightly different for the two-dimensional and divergent boundary layers, it may be expected that the secondary correlation, represented by the limitation on the valid region of the g, H-chart (Fig. 6), will also differ slightly. However the use of the two-dimensional limit line gives satisfactory results, provided that the variation in k which it dictates is less than 0·1.

The result of a calculation, using experimental data directly, for one of the diffuser boundary layers is shown in Fig. 15, together with that of a calculation for the same layer by the method of Rubert and Persh.

7. Conclusions

The analysis of data for the determination of values of k indicated a considerable difference between turbulent boundary layers on lifting aerofoils and those occurring in diffusers. No correlation of data for boundary layers of the former type could be obtained by the method used. This may indicate the influence of the complex mechanism of transition, and may suggest that the uncertainty surrounding the transition region of aerofoil layers is to some extent responsible for the formidable difficulties encountered in attempting to predict the growth of such layers.

For the diffuser boundary layers, a correlation of data was possible and from this a method of calculating the growth of the form parameter H has been evolved. This has given reasonable results for experimental layers from several different sources. Although a step-by-step calculation is required, this is not particularly laborious and it appears that as much numerical accuracy as the method justifies can be attained by the use of a relatively small number of steps, perhaps about ten. The application of the methods to diverging layers is only slightly more complicated than the application to two-dimensional layers.

The formulation of the method required the introduction of experimental evidence concerning the distribution of shear stress across the layer, this being embodied in the correlation of values of k. This correlation was purely empirical and cannot be regarded as completely satisfactory. An important requirement in the field of turbulent boundary layer calculation is a theory for the prediction of the distribution of turbulent shear stress.

Acknowledgments

The author wishes to thank Professor W. J. Kearton for his kind permission to carry out experimental work in the Mechanical Engineering Department, University of Liverpool, and the workshop staff of the Department for their assistance.

References

1. Rubert, K. F. and Persh, J. A procedure for Calculating the Development of Turbulent Boundary Layers under the Influence of Adverse Pressure Gradients. N.A.C.A. T.N. 2478, 1950.

2. Spence, D. A. The Development of Turbulent Boundary Layers. *Journal of the Aeronautical Sciences*, Vol. 23, p. 3, January 1956.

3. Ludwieg, H. and Tillmann, W. Investigation of the Wall Shearing Stress in Turbulent Boundary Layers. Untersuchungen uber die Wandschubspannung in turbulenten Reibungsschichten. N.A.C.A. T.M. 1285, A.R.C. 14,800, 1950.

4. Squire, H. B. and Young, A. D. The Calculation of the Profile Drag of Aerofoils. R. & M. 1838, 1937.

5. SCHUBAUER, G. B. and KLEBANOFF, P. S. Investigation of Separation of the Turbulent Boundary Layer. N.A.C.A. Report 1030, 1950.

6. MCCULLOUGH, G. B. and GAULT, D. E. Examples of Three Representative Types of Airfoil-Section Stall at Low Speeds. N.A.C.A. T.N. 2502, 1951.

7. ALTMAN, J. M. and HAYTER, NORA-LEE F. A Comparison of the Turbulent Boundary Layer on an Unswept and a Swept Wing. N.A.C.A. T.N. 2500, 1951.

8. VON DOENHOFF, A. E. and TETERVIN, N. Determination of General Relations for the Behaviour of Turbulent Boundary Layers. N.A.C.A. Report 772, 1943.

9. SANDBORN, V. A. Preliminary Experimental Investigation of Low-speed Turbulent Boundary Layers in Adverse Pressure Gradients. N.A.C.A. T.N. 3031, 1953.

10. MASKELL, E. C. Approximate Calculation of the Turbulent Boundary Layer in Two-dimensional Incompressible Flow. A.R.C. 14, 654, 1951.

Stability and Response of Systems Satisfying a Second-Order Linear Differential Equation with Time-Dependent Coefficients

A. W. BABISTER

(The University, Glasgow)

SUMMARY: The differential equation considered is

$$(a_2+b_2\tau)\frac{d^2x}{d\tau^2}+(a_1+b_1\tau)\frac{dx}{d\tau}+(a_0+b_0\tau)\,x=0,$$

where all the a's and b's are real constants.

The nature of the solution is investigated in the neighbourhood of the singular point ($\tau=-a_2/b_2$), and the conditions are found for logarithmic terms to be absent.

The conditions for stability for large values of τ are determined; the system is stable if

$$(a_0+b_0\tau),\quad (a_1+b_1\tau)\quad \text{and}\quad (a_2+b_2\tau)$$

are all positive for large values of τ.

The form of the response is considered and its oscillatory (or non-oscillatory) nature investigated. The Sonin-Pólya theorem is used to determine simple inequalities which must hold between the coefficients of the differential equation in any interval for the relative maxima of $|x|$ to form an increasing or decreasing sequence in that interval.

I. Introduction

A system is considered which satisfies the linear equation

$$(a_2+b_2\tau)\frac{d^2x}{d\tau^2}\frac{dx}{d\tau}+(a_1+b_1\tau)+(a_0+b_0\tau)\,x=0 \quad . \quad . \quad . \quad (1)$$

where all the a's and b's are real constants and $b_2\neq 0$. An equation of this type can arise (*i*) where a linear system is operated over a sufficiently wide range, (*ii*) for mechanical systems in which mass, damping or stiffness varies with time and (*iii*) for electrical systems operating while warming up in which inertia, damping or gain varies with time (*see* also Ref. 1).

Received November 1955

The initial conditions are given by

$$x=x_0, \quad \dot{x}=\dot{x}_0 \quad \text{at } \tau=0. \qquad . \quad . \quad . \quad . \quad . \quad (2)$$

The general solution of (1) is

$$x=C_1x_1+C_2x_2 \qquad . \quad . \quad . \quad . \quad . \quad (3)$$

where C_1 and C_2 are constants satisfying the initial conditions (2) and x_1 and x_2 are any two independent solutions of (1). In general x_1 and x_2 can be expressed in terms of confluent hypergeometric functions (*see* Refs. 1 and 2). Some general properties of solutions of (1) are now considered.

In general, b_2 can be taken to be positive without loss of generality. We are only interested in values of x for positive values of τ.

2. Singular Points

Equation (1) has one regular singularity at $\tau=-a_2/b_2$. We write

$$\tau_0=-\frac{a_2}{b_2} \qquad . \quad . \quad . \quad . \quad . \quad . \quad (4)$$

If b_2 is zero there is no singularity at a finite time. If a_2 and b_2 have the same sign (positive), the singularity will occur for a negative value of τ and is thus not of physical importance. If a_2 and b_2 have opposite signs it is found that, in the neighbourhood of this singular point, the solution of (1) can be put in the form

$$x=\sum_{r=1}^{2}A_r\,x_r\,(\tau),$$

where $x_r\,(\tau)$ is given by

$$(\tau-\tau_0)^{\alpha_r}\left[C_0+\sum_1^{\infty}C_n\,(\tau-\tau_0)^n\right].$$

The indicial equation for α_r is

$$\alpha^2+\left[\frac{a_1b_2-a_2b_1}{b_2^{\,2}}-1\right]\alpha=0. \qquad . \quad . \quad . \quad . \quad (5)$$

Let $$c=\frac{a_1b_2-a_2b_1}{b_2^{\,2}} \qquad . \quad . \quad . \quad . \quad . \quad . \quad . \quad (6)$$

The roots of the indicial equation (5) are 0 and $1-c$. Thus the solution of the differential equation corresponding to the zero root of the indicial equation is always finite at the singular point.

If $c \geqslant 1$, one solution of the differential equation will tend to infinity at τ_0. If $c<1$, both solutions of the differential equation are finite at τ_0, one solution tending to zero as τ approaches τ_0. If $\tau_0>0$, this solution is in general indeterminate for $\tau>\tau_0$.

If c is an integer, one solution of the differential equation in general contains terms such as

$$(\tau - \tau_0)^p \log (\tau - \tau_0),$$

and there is a logarithmic singularity at τ_0. For $c < 1$, the exceptional cases in which the logarithmic terms are absent (and both solutions are finite at τ_0) can be found as in Ref. 3.

For simplicity we put $$s = \tau + \frac{a_2}{b_2} = \tau - \tau_0.$$

Then (1) becomes

$$s\frac{d^2x}{ds^2} + (A_1 + B_1 s)\frac{dx}{ds} + (A_0 + B_0 s)\,x = 0 \qquad (7)$$

where
$$\left.\begin{aligned} A_1 &= \frac{a_1 b_2 - a_2 b_1}{b_2^2} = c \\ B_1 &= \frac{b_1}{b_2} \\ A_0 &= \frac{a_0 b_2 - a_2 b_0}{b_2^2} \\ B_0 &= \frac{b_0}{b_2} \end{aligned}\right\} \qquad (8)$$

Let $$x = \sum_{\nu=0}^{\infty} C_\nu \tau^{\sigma+\nu} \qquad (9)$$

Substituting in (7) and equating coefficients, we have

Coefficient of

$\tau^{\sigma-1}$: $$c_0\,[\sigma(\sigma-1) + A_1\sigma] = 0 \qquad (10)$$

τ^{σ} : $$c_1\,[(\sigma+1)\sigma + A_1(\sigma+1)] + c_0\,[B_1\sigma + A_0] = 0 \qquad (11)$$

$\tau^{\sigma+1}$: $$c_2\,[(\sigma+2)(\sigma+1) + A_1(\sigma+2)] + c_1\,[B_1(\sigma+1) + A_0] + c_0 B_0 = 0 \qquad (12)$$

$\tau^{\sigma+2}$: $$c_3\,[(\sigma+3)(\sigma+2) + A_1((\sigma+3)] + c_2\,[B_1(\sigma+2) + A_0] + c_1 B_0 = 0. \qquad (13)$$

As shown, the roots of the indicial equation (10) are 0 and $1 - A_1$. Consider negative integer values of A_1; the two solutions of the differential equation will contain no logarithmic terms if C_{1-A_1} is indeterminate when we put $\sigma = 0$ in equations (10)-(13).

Putting $\sigma=0$, equations (11)-(13) become

$$c_1A_1+c_0A_0=0$$
$$c_2(2+2A_1)+c_1(B_1+A_0)+c_0B_0=0$$
$$c_3(6+3A_1)+c_2(2B_1+A_0)+c_1B_0=0.$$

If $A_1<1$, from these equations it is found that the following relations must hold between the coefficients for logarithmic terms to be absent.

$$\left.\begin{array}{ll} c=A_1=0, & A_0=0. \\ c=A_1=-1, & \begin{vmatrix} A_0 & -1 \\ B_0 & B_1+A_0 \end{vmatrix}=0 \\ c=A_1=-2, & \begin{vmatrix} A_0 & -2 & 0 \\ B_0 & B_1+A_0 & -2 \\ 0 & B_0 & 2B_1+A_0 \end{vmatrix}=0 \end{array}\right\} \quad . \quad . \quad (14)$$

3. Singular Point at the Origin

When a_2 is zero, the singular point occurs at $\tau=0$. From (9) and (10), it is seen that one solution of the differential equation will make $\dot{x}_0$ infinite if $c>0$ and $\ddot{x}_0$ infinite if $c>-1$. Similarly a solution containing logarithmic terms will make $\ddot{x}_0$ and $\dot{x}_0$ infinite.

If $c<-1$ and is not an integer, both solutions of the differential equation make $\ddot{x}_0$ finite. Then, from (1) with $a_2=0$,

$$a_1\dot{x}_0+a_0x_0=0. \quad . \quad . \quad . \quad . \quad . \quad (15)$$

In this case we are not free to choose both x_0 and $\dot{x}_0$. Two independent solutions can be obtained by specifying, for example, the values of x at the origin and at one subsequent time. Equation (15) also holds when c is a negative integer if the particular relations given by (14) are satisfied.

As already stated, whatever the value of c, there is always one solution of the differential equation which is finite with finite derivatives at the singular point. However, when we are restricted to this one solution, x_0 and $\dot{x}_0$ are related by (15).

4. Stability

The system satisfying equation (1) is said to be stable if, following any initial arbitrary disturbance in position x_0 or in velocity $\dot{x}_0$, the system ultimately returns to its equilibrium position in which both x and $\dot{x}$ are zero. If the system only returns to its original position for particular sets of values of $(x_0, \dot{x}_0)$ the stability is said to be conditional.

Consider the motion at any finite time; x may diverge to infinity only at the singular point $\tau=\tau_0$. As already shown, this occurs if $c\geqslant 1$. We are concerned only with those motions which persist at times subsequent to τ_0.

As shown in Ref. 3, the solution of (1) for large τ is given by

$$x=\sum_{r=1}^{2} e^{\lambda_r \tau} \tau^{\sigma_r} \left(\alpha_0+\frac{\alpha_1}{\tau}+\frac{\alpha_2}{\tau^2}+\ldots\right) \quad . \quad . \quad . \quad (16)$$

where λ_r is a root of the equation

$$B(\lambda)=b_2\lambda^2+b_1\lambda+b_0=0 \quad . \quad . \quad . \quad . \quad . \quad (17)$$

and

$$\sigma_r=-\left[\frac{A(\lambda)}{B'(\lambda)}\right]_{\lambda=\lambda_r} \quad . \quad . \quad . \quad . \quad . \quad (18)$$

where

$$A(\lambda)=a_2\lambda^2+a_1\lambda+a_0. \quad . \quad . \quad . \quad . \quad . \quad (19)$$

If all the roots of (17) are negative or have negative real parts, *i.e.* if with $b_2>0$, we also have $b_1>0$ and $b_0>0$, the system is stable for large values of τ. It is seen that, as would be expected, if neither b_1 nor b_2 vanishes, the conditions for stability for large τ are identical with those for the motion defined by the equation

$$b_2\frac{d^2x}{d\tau^2}+b_1\frac{dx}{d\tau}+b_0=0. \quad . \quad . \quad . \quad . \quad (20)$$

If b_0 is zero, one root of (17) is zero and the corresponding value of σ_r is

$$\sigma_r=-\frac{a_0}{b_1}.$$

For stability for large τ, with $b_2>0$ and $b_0=0$, we must have $b_1>0$ and $a_0>0$.

If b_1 is zero and b_2 and b_0 have the same sign, the roots of (17) are of the form $\pm i\omega$, where

$$\omega^2=\frac{b_0}{b_2}.$$

The corresponding values of σ_r are

$$\sigma_r=-\frac{a_1}{2b_2}\pm\frac{i}{2b_2\omega}(a_0-a_2\omega^2).$$

For stability for large τ, with $b_2>0$ and $b_1=0$, we must have $b_0>0$ and $a_1>0$.

If b_2 is zero, equation (1) is

$$a_2\frac{d^2x}{d\tau^2}+(a_1+b_1\tau)\frac{dx}{d\tau}+(a_0+b_0\tau)x=0. \quad . \quad . \quad . \quad (21)$$

The stability of this system can be deduced from its exact solution.

On substituting $$x = e^{-\frac{a_1\tau}{2a_2} - \frac{b_1\tau^2}{4a_2}} u,$$

the differential equation for u is of the form

$$\frac{d^2u}{d\tau^2} + (A + B\tau + C\tau^2)\, u = 0.$$

This can be solved in terms of the parabolic cylinder functions[4, 5]. It is found that for stability with large τ, with $a_2 > 0$ and b_1 and b_0 not zero, we must have $b_1 > 0$ and $b_0 > 0$.

If both b_1 and b_2 are zero, but b_0 is not zero, we find that for stability with large τ with $a_2 > 0$ we must have $a_1 > 0$ and $b_0 > 0$.

If both b_0 and b_2 are zero but b_1 is not zero, we find that for stability with large τ with $a_2 > 0$ we must have $b_1 > 0$ and $a_0 > 0$.

Finally if $b_0 = b_1 = b_2 = 0$, the system is stable if $a_2 > 0$, $a_1 > 0$ and $a_0 > 0$.

All the above conditions for stability for large values of τ can be expressed by the inequalities

$$(a_0 + b_0\tau) > 0,\ (a_1 + b_1\tau) > 0 \text{ and } (a_2 + b_2\tau) > 0 \quad . \quad . \quad (22)$$

for large values of τ.

5. Oscillatory or Non-Oscillatory Response

Using the Sturmian theory[3] we shall derive some general properties of the response of a system satisfying the equation (1) following some initial disturbance in position or velocity.

As before, for simplicity we put

$$s = \tau + \frac{a_2}{b_2} = \tau - \tau_0.$$

Then (1) becomes

$$s\frac{d^2x}{ds^2} + (A_1 + B_1 s)\frac{dx}{ds} + (A_0 + B_0 s)\, x = 0 \quad . \quad . \quad (23)$$

where A_0, B_0, A_1 and B_1 are given by (8).

Equation (23) can be put in the form

$$\frac{d}{ds}\left(e^{B_1 s} s^{A_1}\frac{dx}{ds}\right) + e^{B_1 s} s^{A_1 - 1}(A_0 + B_0 s)\, x = 0 \quad . \quad . \quad (24)$$

Only positive values of s are considered.

Using Rolle's theorem[6] it is seen from equation (24) that between two consecutive positive zeros of dx/ds there lies at least one real zero of $(A_0+B_0s)\,x$. But between consecutive real zeros of x, by Rolle's theorem, there lies at least one real zero of dx/ds.

Thus, in any positive interval in s which does not include $s=-A_0/B_0$ (*i.e.* $\tau=-a_0/b_0$), between successive maxima and minima of x there is always one real zero.

$$\left.\begin{aligned} &\text{Let} \qquad P=e^{B_1 s}\,s^{A_1} \\ &\qquad\quad Q=e^{B_1 s}\,s^{A_1-1}(A_0+B_0s) \end{aligned}\right\} \qquad . \quad . \quad . \quad . \quad (25)$$

Then for any finite interval (a, b) such that $0<a\leqslant s\leqslant b$, P and Q are continuous real functions of the real variable s. P is positive and dP/ds is continuous throughout this interval.

Using Sturm's fundamental theorem, it is found that if the solutions of (23) oscillate in the interval (a, b) they will oscillate more rapidly if P is decreased or Q is increased. Thus the response is made less oscillatory by decreasing A_0 or B_0 (for $s>0$).

Let P_U and P_L, Q_U and Q_L be the upper and lower bounds of P and Q in the interval (a, b) already defined. Comparing (24) with

$$\frac{d}{ds}\left(P_L\frac{dx}{ds}\right)+Q_U x=0 \qquad . \quad . \quad . \quad . \quad . \quad (26)$$

it is seen that the solutions of (23) do not oscillate more rapidly than those of (26). If Q_U is negative, both solutions of (26) are non-oscillatory. Thus if Q is negative, *i.e.* if (A_0+B_0s) is negative throughout the interval (a, b), the solutions of (23) are non-oscillatory in that interval.

Comparing (24) with

$$\frac{d}{ds}\left(P_U\frac{dx}{ds}\right)+Q_L x=0 \qquad . \quad . \quad . \quad . \quad (27)$$

the solutions of (23) oscillate at least as rapidly as those of (27). If Q_L is negative, the solutions of (27) have a period $2\pi\sqrt{(P_U/Q_L)}$.

If A_0, B_0 and B_1 are positive and $A_1\geqslant 1$, both P and Q increase monotonically for all positive s, and thus the upper and lower bounds of P and Q will occur at the ends of the interval (a, b).

If $b_2=0$, equation (1) becomes

$$a_2\frac{d^2x}{d\tau^2}+(a_1+b_1\tau)\frac{dx}{d\tau}+(a_0+b_0\tau)\,x=0 \qquad . \quad . \quad . \quad (28)$$

Equation (28) can be put in the form

$$\frac{d}{d\tau}\left(e^{\frac{a_1}{a_2}\tau+\frac{b_1}{2a_2}\tau^2}\frac{dx}{d\tau}\right)+e^{\frac{a_1}{a_2}+\frac{b_1}{2a_2}\tau^2}\left(\frac{a_0}{a_2}+\frac{b_0\tau}{a_2}\right)x=0. \qquad (29)$$

This can be analysed as before. It is found that the response is made less oscillatory by decreasing a_0/a_2 or b_0/a_2. If $(a_0+b_0\tau)$ is negative throughout the interval (a, b) the solutions of (28) are non-oscillatory in that interval.

6. Damping of the Response

The Sonin-Pólya theorem[7] can be used to determine whether the successive maxima and minima of any solution of (1) form an increasing or decreasing sequence.

Expressing (1) in the form (24), it is seen from (25) that if (A_0+B_0s) is positive through the interval (a, b) defined in Section 5, both P and Q will be positive and have continuous derivatives. From the Sonin-Pólya theorem, the relative maxima of x form an increasing or decreasing sequence according to whether PQ is decreasing or increasing.

Now
$$PQ=e^{2B_1s}s^{2A_1-1}(A_0+B_0s)$$

$$\frac{d}{ds}(PQ)=e^{2B_1s}s^{2A_1-2}[2(A_0+B_0s)(A_1+B_1s)-A_0].$$

Thus if (A_0+B_0s) is positive throughout the interval (a, b), the relative maxima of $|x|$ will form an increasing or decreasing sequence according to whether

$$(A_0+B_0s)(A_1+B_1s) \quad < \text{ or } > \quad \tfrac{1}{2}A_0 \qquad (30)$$

throughout the same interval.

Certain particular cases are of interest. If A_0, A_1, B_0 and B_1 are all positive, the relative maxima of $|x|$ will decrease for all positive s if $A_1>\frac{1}{2}$. If B_0 is zero and A_0 is positive, from (30) the relative maxima of $|x|$ will form an increasing or decreasing sequence according to whether

$$B_1s \quad < \text{ or } > \quad \tfrac{1}{2}-A_1 \qquad (31)$$

If B_1 is zero and (A_0+B_0s) positive, from (30) the relative maxima of $|x|$ will form an increasing or decreasing sequence according to whether

$$A_1B_0s \quad < \text{ or } > \quad A_0(\tfrac{1}{2}-A_1) \qquad (32)$$

If $b_2=0$, equation (1) can be put in the form (29). This can be analysed as before. It is found that with $a_2>0$, if $(a_0+b_0\tau)$ is positive throughout the interval (a, b) the relative maxima of $|x|$ will form an increasing or decreasing sequence according to whether

$$(a_0+b_0\tau)(a_1+b_1\tau)+\tfrac{1}{2}a_2b_0 \quad < \text{ or } > \quad 0 \quad . \quad . \quad . \quad (33)$$

throughout the same interval. Thus if $b_2=0$ and a_0, a_1, a_2, b_0 and b_1 are all positive, the relative maxima of $|x|$ will decrease for all positive τ.

If both b_1 and b_2 are zero, from (33) with $a_2>0$ and $(a_0+b_0\tau)$ positive, the relative maxima of $|x|$ will form an increasing or decreasing sequence according to whether

$$a_1b_0\tau \quad < \text{ or } > \quad -(a_0a_1+\tfrac{1}{2}a_2b_0) \quad . \quad . \quad . \quad (34)$$

If both b_0 and b_2 are zero, from (33) with $a_2>0$ and $a_0>0$, the relative maxima of $|x|$ will form an increasing or decreasing sequence according to whether

$$b_1\tau \quad < \text{ or } > \quad -a_1. \quad . \quad . \quad . \quad . \quad (35)$$

Finally if $b_0=b_1=b_2=0$, $a_2>0$ and $a_0>0$, the relative maxima will increase or decrease according to whether

$$a_1 \quad < \text{ or } > \quad 0.$$

References

1. Webb, H. A. and Airey, J. R. The Practical Importance of the Confluent Hypergeometric Function. *Phil.Mag.* Series 6, Vol. 36, pp. 129, 1918.
2. Erdélyi, A., Magnus, W., Oberhettinger, F. and Tricomi, F. G. *Higher Transcendental Functions.* Vol. I. Bateman Manuscript Project. McGraw-Hill, 1953.
3. Ince, E. L. *Ordinary Differential Equations.* Longmans, 1926.
4. Whittaker, E. T. and Watson, G. N. *Modern Analysis,* Cambridge, 1935.
5. Erdélyi, A., Magnus, W., Oberhettinger, F. and Tricomi, F. G. *Higher Transcendental Functions.* Vol. II. Bateman Manuscript Project. McGraw-Hill, 1953.
6. Burnside, W. S. and Panton, A. W. *Theory of Equations.* Vol. I. Longmans, 1904.
7. Szegö, G. *Orthogonal Polynomials.* American Mathematical Society. Colloquium Publications. Vol. XXIII, 1939.

Note on the Extension of Evvard's Method to Wings with Subsonic Leading Edges Moving at Supersonic Speeds

G. J. HANCOCK

(*Queen Mary College, University of London*)

SUMMARY: Evvard's technique is applied to the problem of a thin finite wing moving at a supersonic speed when the leading edge is subsonic. It is developed in two methods:—

(*i*) in which the relationship between the pressure loading and the integrals of the downwash over the wing surface is extended as far as possible, and which has to be computed numerically;

(*ii*) in which approximations are made for the upwash velocities in the neighbourhood of the leading edge, resulting in a series of standard integrals for the estimation of the pressure loading.

Method (*ii*) is applied to the pressure loading on a flat plate triangular wing and cropped delta wing, and the application to more general shapes is discussed.

1. Introduction

The general problem of the determination of the pressure loading on a thin wing moving at supersonic speeds when the leading edge is supersonic can usually be solved, within the framework of the linearised theory, by Evvard's method[1]. In this method the pressure at a point on the wing is given as an integral of the downwash over certain regions of the wing surface upstream of the reference point. However, the problem for a thin wing with a subsonic leading edge has not been investigated fully from this point of view, although particular cases, such as triangular wings and cropped delta wings, have been investigated by alternative techniques (*e.g.* harmonic transformation theory[2], operational methods[3], doublet line considerations[4] and the superposition of conical fields[5]).

It seems worthwhile therefore to determine the possibility of extending Evvard's method to this problem of thin wing with a subsonic leading edge because:—

(*i*) Its generality covers plan form and camber, and is particularly useful in aeroelastic problems.

Received November 1955.

(*ii*) It is generally recognised that the transonic region is a region in which oscillatory troubles are apparently concentrated (*e.g.* flutter, negative aerodynamic damping) so that oscillatory derivatives are needed. At present these are mainly derived from slender-body theory, which is inadequate for a full investigation. However, since it has finally been shown that Evvard's method can be applied to the problem of an oscillatory rectangular wing[6, 7], a path is indicated for obtaining similar derivatives of subsonic leading edge wings once the steady case has been investigated.

The first attempt on this problem was made by Evvard[8] where, as a first approximation to a perturbation velocity potential at a point P on the wing, he integrates the downwash over the Mach reflection " diamond " S formed upstream of the reference point P, shown in Fig. 1. This method can only be applied with assurance when the wing leading edge is only slightly subsonic. The error, as compared to the exact linearised solution, increases as the Mach number approaches unity, to the order of 30 per cent at $M=1$ for a triangular plate aerofoil. A second investigation has recently been published by Etkin and Woodward[9], where they state that a second approximation to the problem is the inclusion of a further area of integration with Evvard's area S, namely S_1, indicated in Fig. 1.

This approximation is shown to be nearer to the accurate linearised pressure distribution over a triangular plate than Evvard's, with a maximum error of 12 per cent at $M=1$; however, no attempt is made apparently to show that this approximation is valid for all wings or to indicate the way to the determination of a more accurate solution.

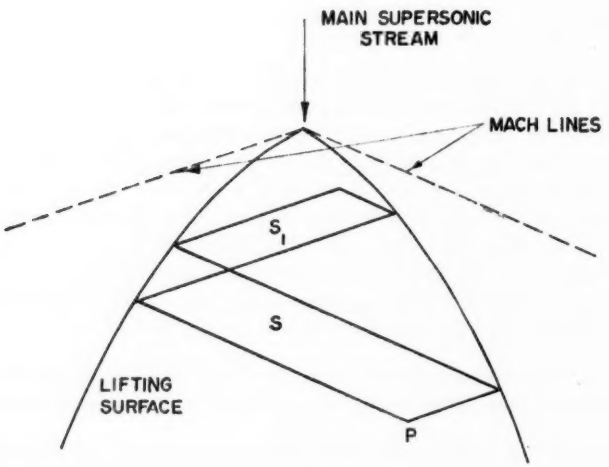

Fig. 1.
Regions of integration suggested by Evvard, and by Etkin and Woodward.

In this paper, a complete solution is not derived for the general problem of establishing a relationship between the pressure loading and integrals of the downwash over regions of the wing surface. Therefore, two courses are open for investigation, as in subsonic incompressible finite wing theory. Either, integral formulae must be developed which can be dealt with numerically, so that the accuracy can be assessed as the computation is carried out, or, some approximate formulae must be developed which are valid within as wide a range of the parameters as possible. In the application to a specific example, the latter method would be used, while the former method could be resorted to as a check in cases of doubt, if alternative exact theories are not available.

One point of interest may be noted. It is that for wings with subsonic leading edges the accuracy of any results at Mach numbers very near to unity, obtained by an Evvard technique, is questionable. However, since it is known that the exact linearised solution at $M=1$ is given by the slender-body theory, it should be possible to interpolate between $M=1$ and the Mach number range in which Evvard's method can be applied. It should be emphasised that the validity of any results obtained by this method are bounded by the conditions and assumptions on which the linearised equations are based. Although the linearised equations do not represent the physical flow conditions at $M=1$, the procedure affords a necessary mathematical check of results in this transonic range.

NOTATION

x, y ξ, η	Cartesian co-ordinates
u, v	characteristic co-ordinates
$p(x, y)$	pressure distribution
M	Mach number
a	speed of sound
$\begin{pmatrix} u \\ v \end{pmatrix} = f \begin{pmatrix} v \\ u \end{pmatrix}$	symmetric equations of wing leading edge
S_{wn}, S_{Dn}	areas of integration
$\alpha(u, v)$	incidence
$\lambda(u, v)$	upwash velocities
$\phi(u, v)$	velocity potential
$\beta = (M^2 - 1)^{\frac{1}{2}}$	
θ	angle of sweep.

2. Mathematical Formulation

On the application of the linearised theory to problems of supersonic flow around finite thin wings, it is known that the value of the perturbation velocity potential $\phi(x, y, z)$ on the upper surface of the lifting discontinuity, taken on the

plane $z=+0$ (defining the supersonic flow of velocity V to be in the positive x-direction), is given by

$$\phi(x, y, +0)=\frac{-1}{\pi}\int_S\int \frac{\lambda(\xi, \eta)\, d\xi d\eta}{[(x-\xi)^2-\beta^2(y-\eta)^2]^{\frac{1}{2}}}, \quad . \quad . \quad . \quad (1)$$

where

(*i*) S is the area enclosed by the intersection of the fore Mach cone from the point $(x, y, 0)$ with the xy-plane;

(*ii*) $\lambda(\xi, \eta)$ is the downwash velocity on the xy-plane and, in particular, on the wing surface itself $\lambda(\xi, \eta)$ is given directly by the local angle of incidence.

On transformation of the Cartesian co-ordinates (ξ, η) to characteristic co-ordinates (u, v), defined by

$$\left.\begin{aligned} u&=\frac{M}{2\beta}(\xi-\beta\eta), \qquad v=\frac{M}{2\beta}(\xi+\beta\eta) \\ \text{or} \quad \xi&=\frac{\beta}{M}(u+v), \qquad \eta=\frac{1}{M}(v-u), \end{aligned}\right\} \quad . \quad . \quad . \quad (2)$$

equation (1) reduces to

$$\phi(\bar{u}, \bar{v})=-\frac{1}{\pi M}\int_S\int \frac{\lambda(u, v)\, du dv}{[(\bar{u}-u)(\bar{v}-v)]^{\frac{1}{2}}}, \quad . \quad . \quad . \quad (3)$$

with the transformed reference point $(\bar{u}, \bar{v})$ corresponding to $(x, y, +0)$.

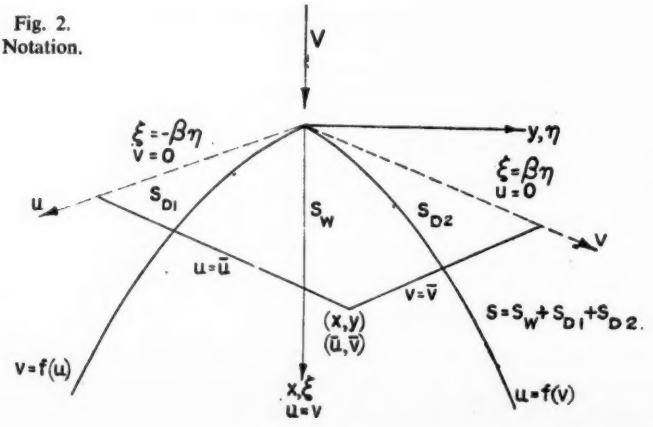

Fig. 2.
Notation.

This paper is concerned with thin aerofoils symmetric about the x-axis (*i.e.* zero yaw) with subsonic leading edges and pointed noses. Hence, the area of integration S is given by $0 \leqslant u \leqslant \bar{u}$, $0 \leqslant v \leqslant \bar{v}$, as shown in Fig. 2, and the equations of the leading edges are denoted by

$$\begin{pmatrix} u \\ v \end{pmatrix} = f\begin{pmatrix} v \\ u \end{pmatrix}.$$

Writing $$S = S_w + S_{D1} + S_{D2},$$

as shown in Fig. 2, where S_w is the contribution to S of the wing surface, S_{D1} and S_{D2} are the areas in the neighbourhood of the leading edges, equation (3) becomes

$$\phi(\bar{u}, \bar{v}) = -\frac{1}{\pi M}\left\{\int\int_{S_w} \frac{-V\alpha(u, v)\,du dv}{[(\bar{u}-u)(\bar{v}-v)]^{\frac{1}{2}}} + \int\int_{S_{D1}+S_{D2}} \frac{\lambda(u, v)\,du dv}{[(\bar{u}-u)(\bar{v}-v)]^{\frac{1}{2}}}\right\}, \qquad (4)$$

where $\alpha(u, v)$ is the local angle of incidence on the wing surface.

It is known, however, that this integral can be reduced further by Evvard's technique to the form

$$\phi(\bar{u}, \bar{v}) = \frac{1}{\pi M}\left\{\int\int_{S_{w1}} \frac{V\alpha(u, v)\,du dv}{[(\bar{u}-u)(\bar{v}-v)]^{\frac{1}{2}}} - \int\int_{S_{w2}} \frac{V\alpha(u, v)\,du dv}{[(\bar{u}-u)(\bar{v}-v)]^{\frac{1}{2}}} + \right.$$
$$\left. + \int\int_{S_{D1}} \frac{\lambda_1(u, v)\,du dv}{[(\bar{u}-u)(\bar{v}-v)]^{\frac{1}{2}}} + \int\int_{S_{D2}} \frac{\lambda_2(u, v)\,du dv}{[(\bar{u}-u)(\bar{v}-v)]^{\frac{1}{2}}}\right\}. \qquad (5)$$

where the areas S_{w1}, S_{w2}, S_{D1} and S_{D2} are shown in Fig. 3; and $\lambda_1(u, v)$, $\lambda_2(u, v)$ are the upwash velocities in the areas S_{D1}, S_{D2} respectively.

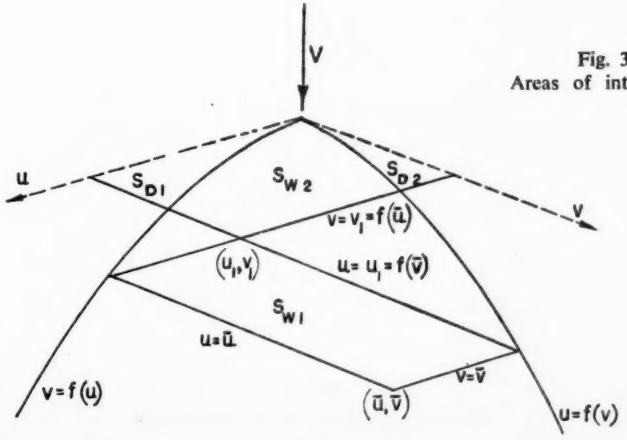

Fig. 3.
Areas of integration.

The development of equation (5) can be followed in two courses, as discussed in Section 1. First, one can attempt to carry Evvard's method to the next stage, reducing the integrals over the upwash regions to integrals over the wing surface, which in general will have to be integrated numerically. Alternatively, estimations can be made of the upwash velocities $\lambda_1(u, v)$ and $\lambda_2(u, v)$ for the direct integration of equation (5).

3. Estimation of Upwash Velocities

To determine the upwash velocities $\lambda_1(u, v)$ and $\lambda_2(u, v)$, equation (1) is applied to a point off the wing surface but within the bow Mach cone. This configuration is indicated in Fig. 4.

By reference to Fig. 4, equation (1) becomes

$$\phi(u_D, v_D) = -\frac{1}{\pi M}\left\{\int\int_{S_w} \frac{-V\alpha(u, v)\,du dv}{[(u_D - u)(v_D - v)]^{\frac{1}{2}}} + \int\int_{S_{D1}+S_{D2}} \frac{\lambda(u, v)\,du dv}{[(u_D - u)(v_D - v)]^{\frac{1}{2}}}\right\}. \quad (6)$$

For points (u_D, v_D) off the wing surface,

$$\phi(u_D, v_D) = 0 \quad . \quad . \quad . \quad . \quad . \quad (7)$$

since the velocity potential is continuous in this region and anti-symmetrical with respect to the uv-plane.

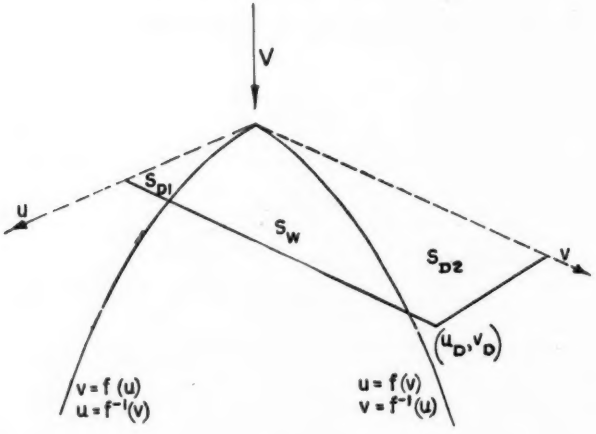

Fig. 4.
Notation for a point off the wing surface.

Therefore, combining equations (6) and (7),

$$\int_{u=0}^{u=u_D} \frac{du}{(u_D-u)^{\frac{1}{2}}} \int_{v=f(u)}^{v=f^{-1}(u)} \frac{V\alpha(u,v)\,dv}{(v_D-v)^{\frac{1}{2}}} = \int_{u=0}^{u=u_D} \frac{du}{(u_D-u)^{\frac{1}{2}}} \left\{ \int_{v=0}^{v=f(u)} \frac{\lambda_1(u,v)\,dv}{(v_D-v)^{\frac{1}{2}}} + \int_{v=f^{-1}(u)}^{v=v_D} \frac{\lambda_2(u,v)\,dv}{(v_D-v)^{\frac{1}{2}}} \right\} \quad (8)$$

in the notation previously introduced, using the idea of an operator f denoting the leading edge equation, so that $u=f(v)$ is equivalent to $v=f^{-1}(u)$.

Thus, since u_D is a general point on the upwash field S_{D2}, the integrand with respect to u in equation (10) may be put equal to zero; hence

$$\int_{v=f(u)}^{v=f^{-1}(u)} \frac{V\alpha(u,v)\,dv}{(v_D-v)^{\frac{1}{2}}} = \int_{v=0}^{v=f(u)} \frac{\lambda_1(u,v)\,dv}{(v_D-v)^{\frac{1}{2}}} + \int_{v=f^{-1}(u)}^{v=v_D} \frac{\lambda_2(u,v)\,dv}{(v_D-v)^{\frac{1}{2}}} \quad . \quad . \quad . \quad (9)$$

A similar expression can be written for the area S_{D1}, giving, with equation (9), a pair of simultaneous equations for $\lambda_1(u,v)$ and $\lambda_2(u,v)$; but this paper is only concerned with a wing which is symmetrical about the line $u=v$, and the relationship between the two upwash velocities is

$$\lambda_1(u,v)=\lambda_2(v,u). \quad . \quad . \quad . \quad . \quad . \quad (10)$$

If equation (9) is rewritten in the form

$$\int_{v=f^{-1}(u)}^{v=v_D} \frac{\lambda_2(u,v)\,dv}{(v_D-v)^{\frac{1}{2}}} = \int_{v=f(u)}^{v=f^{-1}(u)} \frac{V\alpha(u,v)\,dv}{(v_D-v)^{\frac{1}{2}}} - \int_{v=0}^{v=f(u)} \frac{\lambda_1(u,v)\,dv}{(v_D-v)^{\frac{1}{2}}}, \quad . \quad . \quad (11)$$

then this could be regarded as an Abel type of integral equation for $\lambda_2(u,v)$. It is known that if

$$\int_k^x \frac{u(\xi)\,d\xi}{(x-\xi)^{\mu}} = f(x), \qquad \text{where} \qquad \begin{cases} 0<\mu<1 \\ k<x<k_1, \end{cases}$$

$$\text{then} \qquad u(x)=\frac{\sin\mu\pi}{\pi}\frac{d}{dx}\int_k^x \frac{f(\xi)\,d\xi}{(x-\xi)^{1-\mu}}.$$

Hence, the solution of equation (11) is

$$\lambda_2(u,v)=\frac{1}{\pi}\frac{\partial}{\partial v}\int_{f^{-1}(u)}^{v} \frac{dv_D}{(v-v_D)^{\frac{1}{2}}} \left\{ \int_{v'=0}^{v'=f^{-1}(u)} \frac{V\alpha(u,v')\,dv'}{(v_D-v')^{\frac{1}{2}}} - \int_{v'=f(u)}^{v'=f(u)} \frac{\lambda_1(u,v')\,dv'}{(v_D-v')^{\frac{1}{2}}} \right\}$$

$$= \frac{1}{\pi}\left\{ \int_{v'=f(u)}^{v'=f^{-1}(u)} \frac{V\alpha(u,v')}{v-v'}\left(\frac{f^{-1}(u)-v'}{v-f^{-1}(u)}\right)^{\frac{1}{2}} dv' - \int_{v'=0}^{v'=f(u)} \frac{\lambda_1(u,v')}{v-v'}\left(\frac{f^{-1}(u)-v'}{v-f^{-1}(u)}\right)^{\frac{1}{2}} dv' \right\} \quad (12)$$

This equation can be regarded as an integral equation for $\lambda_2(u, v)$ by using the symmetrical relationship of equation (10). The second term depending on $\lambda_1(u, v)$, however, is in general smaller than the first term, depending on the wing incidence, for Mach numbers greater than unity, and may be neglected for a first approximation to the upwash problem. Further approximations may be obtained by a successive approximation technique of substitution of the first value of $\lambda_2(u, v)$ in the second integral.

4. Method 1

In this method we attempt to extend Evvard's idea of replacing the upwash integrals by integrals over the wing surface. We begin by substituting equation (12) for $\lambda_2(u, v)$, and the similar symmetric integral expression for $\lambda_1(u, v)$, in equation (5). Consider first the integral

$$I_{D2} = \int\int_{S_{D2}} \frac{\lambda_2(u, v)\, du dv}{[(\bar{u}-u)(\bar{v}-v)]^{\frac{1}{2}}} = \int_{u=0}^{u=u_2} \frac{du}{(\bar{u}-u)^{\frac{1}{2}}} \int_{v=f^{-1}(u)}^{v=v_1} \frac{\lambda_2(u, v)\, dv}{(\bar{v}-v)^{\frac{1}{2}}} , \qquad (13)$$

where $u_2 = f(v_1) = f^2(\bar{u})$, shown in Fig. 3. Then, on substitution of equation (12) in equation (13), the expression (14) is obtained, on integration with respect to v, and then changing the variable v' to v.

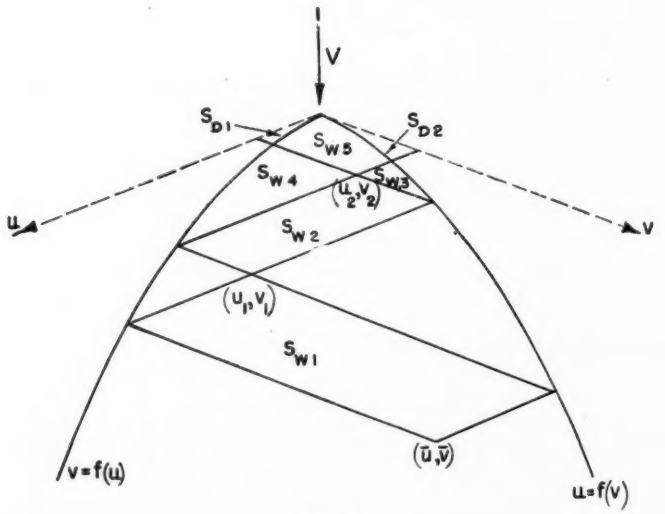

Fig. 5.
Areas of integration.

$$I_{D2}=\int_{u=0}^{u=u_2}\frac{du}{(\bar{u}-u)^{\frac{1}{2}}}\int_{v=f(u)}^{v=f^{-1}(u)}\frac{\alpha(u,v)}{(\bar{v}-v)}\left\{1-\frac{2}{\pi}\tan^{-1}\left(\frac{f^{-1}(u)-v}{\bar{v}-v}\right)\left(\frac{\bar{v}-v}{v_1-f^{-1}(u)}\right)^{\frac{1}{2}}\right\}dv-$$

$$-\int_{u=0}^{u=u_2}\frac{du}{(\bar{u}-u)^{\frac{1}{2}}}\int_{v=0}^{v=f(u)}\frac{\lambda_1(u,v)}{(\bar{v}-v)^{\frac{1}{2}}}\left\{1-\frac{2}{\pi}\tan^{-1}\left(\frac{f^{-1}(u)-v}{\bar{v}-v}\right)\left(\frac{\bar{v}-v}{v_1-f^{-1}(u)}\right)^{\frac{1}{2}}\right\}dv \quad (14)$$

Therefore, using equation (14), equation (5) reduces to

$$\phi(\bar{u},\bar{v})\,\pi M=\iint_{S_{W1}}\frac{V\alpha(u,v)\,dudv}{[(\bar{u}-u)(\bar{v}-v)]^{\frac{1}{2}}}-\iint_{S_{W2}}\frac{V\alpha(u,v)\,dudv}{[(\bar{u}-u)(\bar{v}-v)]^{\frac{1}{2}}}-$$

$$-\iint_{S_{W3}}\frac{V\alpha(u,v)}{[(\bar{u}-u)(\bar{v}-v)]^{\frac{1}{2}}}\left(\frac{2}{\pi}\right)\tan^{-1}\left(\frac{f^{-1}(u)-v}{\bar{v}-v}\right)\left(\frac{\bar{v}-v}{v_1-f^{-1}(u)}\right)^{\frac{1}{2}}dudv-$$

$$-\iint_{S_{W4}}\frac{V\alpha(u,v)}{[(\bar{u}-u)(\bar{v}-v)]^{\frac{1}{2}}}\left(\frac{2}{\pi}\right)\tan^{-1}\left(\frac{f^{-1}(v)-u}{\bar{u}-u}\right)\left(\frac{\bar{u}-u}{u_1-f^{-1}(v)}\right)^{\frac{1}{2}}dudv+$$

$$+\iint_{S_{W5}}\frac{V\alpha(u,v)}{[(\bar{u}-u)(\bar{v}-v)]^{\frac{1}{2}}}\left\{1-\frac{2}{\pi}\tan^{-1}\left(\frac{f^{-1}(u)-v}{\bar{v}-v}\right)\left(\frac{\bar{v}-v}{v_1-f^{-1}(u)}\right)^{\frac{1}{2}}-\right.$$

$$\left.-\frac{2}{\pi}\tan^{-1}\left(\frac{f^{-1}(v)-u}{\bar{u}-u}\right)\left(\frac{\bar{u}-u}{u_1-f^{-1}(v)}\right)^{\frac{1}{2}}\right\}dudv-$$

$$-\iint_{S_{D1}}\frac{\lambda_1(u,v)}{[(\bar{u}-u)(\bar{v}-v)]^{\frac{1}{2}}}\left\{1-\frac{2}{\pi}\tan^{-1}\left(\frac{f^{-1}(u)-v}{\bar{v}-v}\right)\left(\frac{\bar{v}-v}{v_1-f^{-1}(u)}\right)^{\frac{1}{2}}\right\}dudv-$$

$$-\iint_{S_{D2}}\frac{\lambda_2(u,v)}{[(\bar{u}-u)(\bar{v}-v)]^{\frac{1}{2}}}\left\{1-\frac{2}{\pi}\tan^{-1}\left(\frac{f^{-1}(v)-u}{\bar{u}-u}\right)\left(\frac{\bar{u}-u}{u_1-f^{-1}(v)}\right)^{\frac{1}{2}}\right\}dudv$$

. . . . . (15)

where the areas of integration are shown in Fig. 5.

Theoretically it is possible to repeat the process of substitution for $\lambda_1(u,v)$ and $\lambda_2(u,v)$ in equation (15) and so reduce further the integrals of the upwash velocities to regions of the wing surface. A reasonable approximation would result by neglecting the integrals over S_{D1} and S_{D2}, giving a value slightly greater than the accurate solution, but the integrations over the remaining areas would in general have to be computed, preferably in the manner suggested by Etkin and Woodward[9]. A further approximation could be developed by replacing $\lambda_1(u,v)$ and $\lambda_2(u,v)$ by the first term in equation (12).

As pointed out in the Introduction, Evvard's[8] assumption involved the integral over S_{W1}, while Etkin and Woodward[9] included also the integral over S_{W2}. However, for more reliable results recourse must be made to an equation similar to (15).

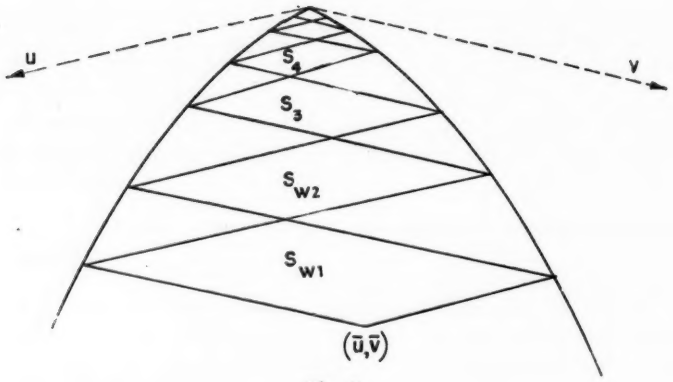

Fig. 6.
Areas of integration.

The question of accuracy arises if the process indicated by equation (15) is stopped at any particular stage and, in general, the maximum error will appear on approaching $M=1$. As pointed out in the Introduction (Section 1) a mathematical check is available at $M=1$ from slender-body theory, so that all that is necessary is to ensure that the integrations give solutions as true as possible for conditions as near to $M=1$ as possible. In general, one could only do this by actually computing specific examples, but it is interesting to discuss the convergence of a similar expansion to equation (15). It is assumed that the velocity potential is given by

$$\phi(\bar{u},\bar{v})=\frac{1}{\pi M}\underset{S_{w1}-S_{w2}+S_3-S_4}{\int\int}\frac{V\alpha(u,v)\,du dv}{[(\bar{u}-u)(\bar{v}-v)]^{\frac{1}{2}}}$$

where S_{w1}, S_{w2}, S_3, etc., are indicated in Fig. 6.

For a triangular flat plate, $\alpha=$ constant and $v=ku$, $u=kv$ are the equations of the leading edges (k being a constant depending on the angle of sweepback and the Mach number); hence

$$\phi(\bar{u},\bar{v})=\frac{V\alpha}{\pi M}\left\{4\left[(\bar{u}-k\bar{v})(\bar{v}-k\bar{u})\right]^{\frac{1}{2}}-4\left[(\bar{u}-k^2\bar{u})^{\frac{1}{2}}-(\bar{u}-k\bar{v})^{\frac{1}{2}}\right]\left[(\bar{v}-k^2\bar{v})^{\frac{1}{2}}-\right.\right.$$
$$\left.\left.-(\bar{v}-k\bar{u})^{\frac{1}{2}}\right]+4\left[(\bar{u}-k^3\bar{v})^{\frac{1}{2}}-(\bar{u}-k^2\bar{u})^{\frac{1}{2}}\right]\left[(\bar{v}-k^3\bar{u})^{\frac{1}{2}}-(\bar{v}-k^2\bar{v})^{\frac{1}{2}}\right]\ldots\ldots\right\}.$$

The pressure loading then becomes

$$p(\bar{u},\bar{v})=2\rho V\frac{\partial\phi}{\partial x}=2\rho V\left(\frac{M}{2\beta}\right)\left(\frac{\partial}{\partial\bar{u}}+\frac{\partial}{\partial\bar{v}}\right)\phi(\bar{u},\bar{v})$$
$$=\frac{2\rho V^2\alpha}{\pi\beta}\left\{(1-k)\left[\left(\frac{\bar{v}-k\bar{u}}{\bar{u}-k\bar{v}}\right)^{\frac{1}{2}}+\left(\frac{\bar{u}-k\bar{v}}{\bar{v}-k\bar{u}}\right)^{\frac{1}{2}}\right]-\ldots\ldots\right\}.$$

At $M=1$, since $k \longrightarrow 1$ as $\beta \longrightarrow 0$, so that $(1-k)/\beta$ is finite in the limit, the pressure loading on the centre chord line $\bar{u}=\bar{v}$ is

$$p\ (\bar{u}, \bar{u}) = K\ \{2 - 0{\cdot}34 + 0{\cdot}20 - \ \ldots\ . + (-1)^n 2\ [2n+1-2\ (n^2+n)^{\frac{1}{2}}]\ \ldots\ \}$$

where K depends on ρa^2, α and the angle of sweep. Although the convergence of this series is slow the first three terms give an answer to within four per cent.

On the basis of this example it could be argued that the approximation to equation (15), as suggested, forms the starting point for calculating pressure loadings for all practical purposes.

5. Method 2

In Section 4 a rigorous approach to the problem is presented which involves rather complicated integrals, leading to a numerical approach which can be used to give any desired accuracy. However, in general, this would be too cumbersome, so that an alternative, if more approximate, technique should be developed. This possibility is investigated in this section.

The method is to obtain expressions for the upwash velocities directly from equation (12), substitute them in equation (5) and integrate approximately.

Now equation (14) states that

$$\lambda_2\ (u, v) = \frac{1}{\pi} \int_{v'=f(u)}^{v'=f^{-1}(u)} \frac{V\alpha\ (u, v')}{v - v'} \left(\frac{f^{-1}\ (u) - v'}{v' - f^{-1}\ (u)} \right) dv' \qquad . \quad . \quad (16)$$

$$+ \text{an integral depending on } \lambda_1\ (u, v).$$

It is possible to neglect the effect of the second integral depending on $\lambda_1\ (u, v)$, but the percentage effect can be calculated by a successive approximation technique, as suggested previously. The integral over the wing can be worked out fairly easily; for example

(*i*) flat plate, *i.e.* $\alpha = \text{constant}$

$$\lambda_2\ (u, v) = \frac{2\alpha V}{\pi} \left\{ \left(\frac{f^{-1}\ (u) - f\ (u)}{v - f^{-1}\ (u)} \right)^{\frac{1}{2}} - \tan^{-1} \left(\frac{f^{-1}\ (u) - f\ (u)}{v - f^{-1}\ (u)} \right)^{\frac{1}{2}} \right\} \qquad . \quad (17)$$

(*ii*) linear camber, *i.e.* $\alpha = C_1 u + C_2 v$, then

$$\lambda_2\ (u, v) = \frac{2V}{\pi} (\text{?} + \text{?}) \left\{ \left(\frac{f^{-1}\ (u) - f\ (u)}{v - f^{-1}\ (u)} \right)^{\frac{1}{2}} - \tan^{-1} \left(\frac{f^{-1}\ (u) - f\ (u)}{v - f^{-1}\ (u)} \right)^{\frac{1}{2}} \right\} -$$

$$- \frac{2VC_2}{3\pi} \left(\frac{[f^{-1}\ (u) - f\ (u)]^3}{v - f^{-1}\ (u)} \right)^{\frac{1}{2}}$$

and similarly for more complex cambers.

The second approximation is found by substituting the first approximation derived already in the second integral in equation (12); hence for a flat plate wing

$$\lambda_2(u,v)=\frac{2\alpha V}{\pi}\left\{\left(\frac{f^{-1}(u)-f(u)}{v-f^{-1}(u)}\right)^{\frac{1}{2}}-\tan^{-1}\left(\frac{f^{-1}(u)-f(u)}{v-f^{-1}(u)}\right)^{\frac{1}{2}}-\right.$$
$$\left.-\frac{1}{\pi}\int_{v'=0}^{v'=f(u)}\left\{\left(\frac{f^{-1}(v')-f(v')}{u-f^{-1}(v')}\right)^{\frac{1}{2}}-\tan^{-1}\left(\frac{f^{-1}(v')-f(v')}{u-f^{-1}(v')}\right)^{\frac{1}{2}}\right\}\left(\frac{f^{-1}(u)-v'}{v-f^{-1}(u)}\right)^{\frac{1}{2}}dv'\right\} \quad (18)$$

For a flat plate with straight edges

$$\begin{pmatrix}u\\v\end{pmatrix}=f\begin{pmatrix}v\\u\end{pmatrix}$$

can be taken as

$$\begin{pmatrix}u\\v\end{pmatrix}=k\begin{pmatrix}v\\u\end{pmatrix},$$

where k is a constant and equal to $(1-\beta\tan\theta)/(1+\beta\tan\theta)$, θ being the semi-apex angle. Equation (18) reduces in this case to

$$\lambda_2(u,v)=\frac{2\alpha V}{\pi}\left\{\left[\frac{u(1-k^2)}{kv-u}\right]^{\frac{1}{2}}-\tan^{-1}\left[\frac{u(1-k^2)}{kv-u}\right]^{\frac{1}{2}}-\right.$$
$$\left.-\frac{u[1-(1-k^2)^{\frac{1}{2}}]}{2(v-ku)k}\left[\frac{u(1-k^2)}{kv-u}\right]^{\frac{1}{2}}\right\} \quad . \quad . \quad . \quad (19)$$

The maximum effect of the third term compared with the first term is for $u=kv$, and then the ratio of these terms is

$$\frac{1-(1-k^2)^{\frac{1}{2}}}{2k(1-k^2)}.$$

For $k=0{\cdot}3$, $\dfrac{1-(1-k^2)^{\frac{1}{2}}}{2k(1-k^2)}=0{\cdot}025$,

$k=0{\cdot}5$, $\dfrac{1-(1-k^2)^{\frac{1}{2}}}{2k(1-k^2)}=0{\cdot}085$,

$k=0{\cdot}7$, $\dfrac{1-(1-k^2)^{\frac{1}{2}}}{2k(1-k^2)}=0{\cdot}30$,

so that it seems that, for $k=0{\cdot}5$, the third term could be neglected in comparison with the first term, but for higher values of k it should be taken into consideration. It is worth noting that $k=0{\cdot}5$ corresponds to $\beta\tan\theta=\frac{1}{3}$, so for a 45° sweep this corresponds to Mach 1·05; hence the range of k greater than 0·5 only contributes to the range of Mach number 1·00 to 1·05 for this particular wing. An approximate theory which is valid down to a Mach number near to unity is sufficient for most practical cases. For the rest of the analysis this third correction term in

equation (19) will be neglected. The foregoing example is taken as a test case in respect that other problems, such as cambered wings, curved leading edges, and so on result in terms of the same relative order in an equation corresponding to (19).

It follows from the foregoing argument that in equation (15) the terms involving the upwash velocities can be neglected to the same degree of approximation as intimated.

6. Determination of Pressure Loading

The integral for the velocity potential is given in equation (5), and may be written

$$\phi(\bar{u}, \bar{v}) = \frac{1}{\pi M}(I_w + I_D) \quad . \quad . \quad . \quad . \quad . \quad (20)$$

where $$I_w = V \iint_{S_{w1}-S_{w2}} \frac{\alpha(u, v)\, du dv}{[(\bar{u}-u)(\bar{v}-v)]^{\frac{1}{2}}} \quad . \quad . \quad . \quad . \quad . \quad (21)$$

and $$I_D = \iint_{S_{D1}+S_{D2}} \frac{\lambda(u, v)\, du dv}{[(\bar{u}-u)(\bar{v}-v)]^{\frac{1}{2}}} \quad . \quad . \quad . \quad . \quad . \quad (22)$$

The areas S_{w1}, S_{w2}, S_{D1} and S_{D2} are shown in Fig. 3. The wing incidence $\alpha(u, v)$ is known for any given wing. The upwash velocity is determined by the method suggested in Section 5.

The pressure loading $p(\bar{u}, \bar{v})$ is given by

$$p(\bar{u}, \bar{v}) = 2\rho V \phi_x$$
$$= \frac{\rho V M}{\beta}\left(\frac{\partial}{\partial \bar{u}} + \frac{\partial}{\partial \bar{v}}\right)\phi(\bar{u}, \bar{v}) \quad . \quad . \quad . \quad . \quad (23)$$

on account of transformation equation (2). This can be applied to equation (20) in two ways. Either the integration is performed first, as defined by equation (20), followed by the operational equation (23) for each specific example, or, general expressions can be developed for $p(\bar{u}, \bar{v})$ by differentiating equation (20) under the integral signs. In both cases the expression involving I_w (equation (21)) will be composed of standard integrals for most leading edge contours and cambers. The evaluation of equation (23) is complex but a slight modification may be introduced which reduces the integrals to a more amenable form. Consider, for example, the integration over area S_{D2} (*see* Fig. 3). Since the variation of u is within the range $0 \leqslant u \leqslant f(v_1)$, or $0 \leqslant u \leqslant f^2(\bar{u})$, and $f^2(\bar{u}) << \bar{u}$, the function $\bar{u}-u$ may be replaced by $\bar{u}-f^2(\bar{u})$ and taken outside the integral sign. This approximation may be regarded as being of the same order of error as those incurred in the calculation of the upwash velocities $\lambda(u, v)$.

These ideas have been applied to the calculation of pressure loadings over particular wings.

6. Triangular Flat Plate

6.1. The General Case

In this case the equations of the leading edges are given by

$$\begin{pmatrix} u \\ v \end{pmatrix} = k \begin{pmatrix} v \\ u \end{pmatrix},$$

where, as previously noted, $k = \dfrac{1-\beta \tan\theta}{1+\beta \tan\theta}$, θ being the semi-apex angle.

Mach 1 corresponds to $k=1$, and occurs when the leading edge becomes sonic. The formulae of the pressure loading are simple in this case.

The graph of $C_p/(2\pi \tan\theta)$ against $\beta \tan\theta$, where C_p is the pressure coefficient on the centre chord line, is shown in Fig. 7, derived by the foregoing method. It is compared with the exact solution, and also with that of Etkin and Woodward.

6.2. Cropped Delta Flat Plate

The application of this approximate theory to the problem of the severely cropped delta wing has greater practical significance than that for the triangular wing, since the exact solution of the problem involves the superposition of conical fields. The wing contour is defined by

$$\begin{pmatrix} u \\ v \end{pmatrix} = k_1 \begin{pmatrix} v \\ u \end{pmatrix} \qquad \text{for the leading edges}$$

$$\text{and} \quad = \begin{pmatrix} u \\ v \end{pmatrix} \begin{matrix} v + k_2 \\ u + k_2 \end{matrix} \qquad \text{for the wing tips,}$$

together with the Mach regions of influence A, B and C, as shown.

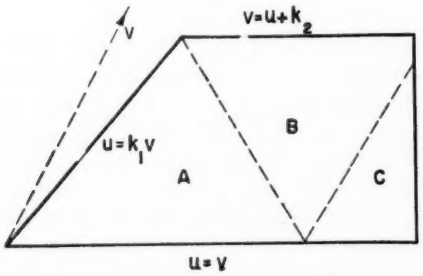

The pressure distribution in area A is given by the solution for the triangular wing in Section 6.1. The pressure at a point (u, v) in areas B and C follow directly from this solution, since the related point (u_1, v_1) lies in area A, so that the upwash velocities around the leading edge only are needed.

The loading has been calculated for a wing of 45° sweep, unit tip chord, root chord = 2 at $M = 1{\cdot}1$, and is shown in Fig. 8.

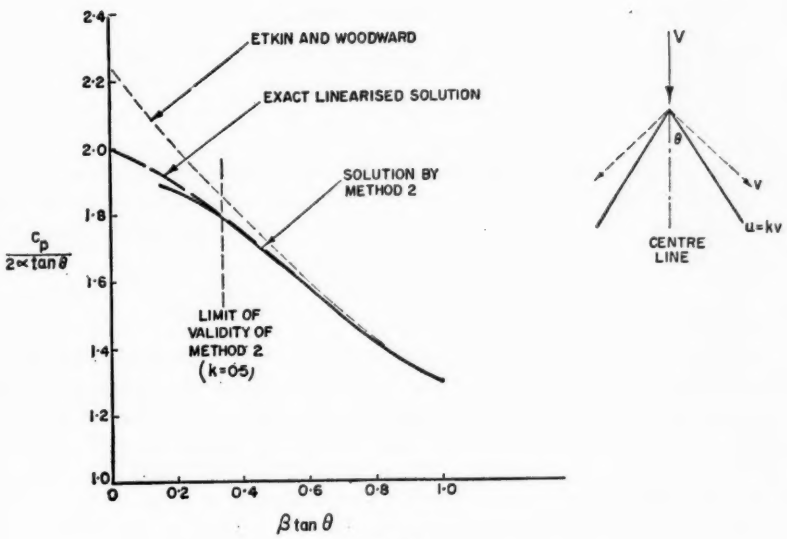

Fig. 7.
Pressure coefficient on the centre line of triangular wings.

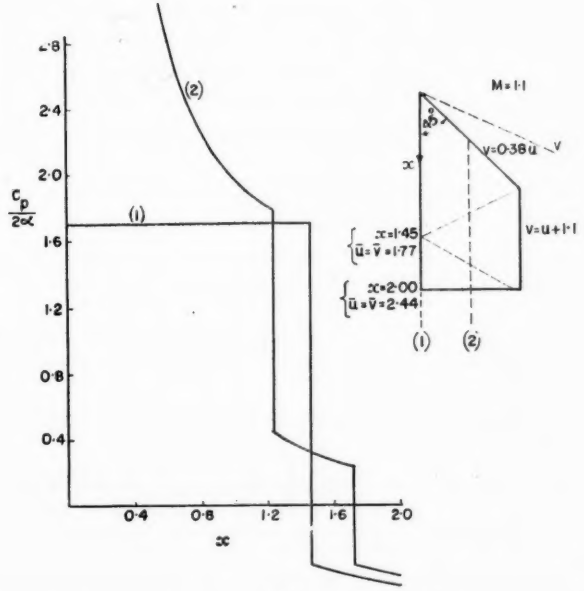

Fig. 8.
Pressure distribution on the cropped delta wing.

6.3. Flat Plate with Curved Leading Edges

In this case the equation of the leading edge will be of the form

$$v = f(u) = k_1 + [k_2 + k_3 u + k_4 u^2]^{\frac{1}{2}},$$

where the k_n's are constants depending on the wing contour and Mach number. It can be shown that the integrals reduce to standard types, especially if the wing contour changes slowly so that $v = f(u)$ can be expressed by the first few terms of its Taylor series with reasonable accuracy.

6.4. Cambered Aerofoils

The procedure for cambered aerofoils is exactly the same as that for the flat plate aerofoils. The approximations intimated are sufficient to reduce the integrals to standard forms if the incidence distribution is given as a series, although the number of integrals to be evaluated rises appreciably as the complexity of the incidence increases. However, the method is straightforward, even if tedious, and has the fundamental advantage of being completely general.

References

1. Evvard, J. C. Use of Source Distribution for Evaluating Theoretical Aerodynamics of Thin Finite Wings at Supersonic Speeds. N.A.C.A. Report 951, 1950.
2. Robinson, A. Rotary Derivatives of a Delta Wing at Supersonic Speeds. *Journal of the Royal Aeronautical Society*, Vol. 52, pp. 735-752, November 1948.
3. Stewartson, K. On Linearized Potential Theory of Unsteady Supersonic Motion. Symposium on Aerodynamics. Institute of Aerophysics. University of Toronto, 1954.
4. Brown, C. E. Theoretical Lift and Drag on Thin Triangular Wings at Supersonic Speeds. N.A.C.A. Report 839, 1946.
5. Cohen, D. M. Formulae for Supersonic Loading, Lift, Drag of Flat Swept-Back Wings with Leading Edges behind Mach Lines. N.A.C.A. T.N. 1050, 1952.
6. Stewart, H. J. and Li, T. Y. Periodic Motions of a Rectangular Wing Moving at Supersonic Speeds. *Journal of the Aeronautical Sciences*, Vol. 17, pp. 529-539, September 1950.
7. Stewart, H. J. and Li, T. Y. On an Integral Equation in the Supersonic Oscillating Wing Theory. *Journal of the Aeronautical Sciences*, Readers Forum, Vol. 20, October 1953.
8. Evvard, J. C. Effects of Yawing Thin Pointed Wings at Supersonic Speeds. N.A.C.A. T.N. 1429, 1947.
9. Etkin, B. and Woodward, F. A. Lift Distribution on Supersonic Wings with Subsonic Leading Edges and Arbitrary Angles of Attack. Proceedings of the Second Canadian Symposium on Aerodynamics. Institute of Aerophysics. University of Toronto, 1954.

Non-Linear Elasticity in Aluminium Alloys

A. B. WATTS*, B.Sc.(Eng.), Ph.D.

SUMMARY: Tests have been carried out on round bar specimens of various strong aluminium alloys (unclad) in the fully heat-treated condition in both tensile and compressive loading. A careful study of the results establishes beyond reasonable doubt that there is a progressive change in the tangent elastic modulus with stress. The variation is appreciably greater than that predicted by the consideration of second-order effects in the conventional stress and strain representation. It is found that the modulus decreases with tension and increases with compression by about 5 per cent at 30 tons/in.^{2}, the form of the variation being a continuous function. Tests on two alloys of aluminium other than those of the normal zinc-bearing and the copper-bearing types were also carried out. The first of these was a simple fully heat-treated binary alloy of 4 per cent copper which was very similar in behaviour to D.T.D.364; the second was a 5 per cent alloy (N.S.6-½H) which, after its initial loading, showed only very slight elastic modulus variation in the subsequent loading and unloading lines. An additional test to compare naturally and artificially aged D.T.D.364 did not reveal any difference in the degree of modulus variation.

In view of the present experimental findings, the use of the "second" modulus line in the proof stress determination of unclad strong alloys should be adopted generally, if practicable. A high level of internal stress can cause slight errors in this method because the elastic limit is then prematurely reached. As an occasional check on the method when applied to routine mechanical testing, the elastic component of strain can be found for the last point on the loading line by returning to the zeroing load.

In the Appendix the difference between true and nominal stress-strain relationships is calculated. The meaning and theory of modulus variation is also discussed and aluminium alloys are compared with a high-tensile steel.

A simple expression for the form of the variation is proposed.

1. Introduction

The non-linear elasticity of metallic materials is a direct contradiction of the simple laws which are commonly regarded to hold true. In attempting to decide for any material whether or not there is non-linear elastic behaviour, it is important to eliminate a number of factors which can, and do, modify the shape of a stress-strain curve such as is obtained in a proof stress determination. If a particular material does exhibit a genuine curvature of the purely elastic portion of its stress-strain curve when all these factors have been eliminated, then the result has far-reaching implications in several different fields.

*The work described in this paper was done while the author was a research engineer with The British Aluminium Company.

Received April 1956.

6.3. Flat Plate with Curved Leading Edges

In this case the equation of the leading edge will be of the form

$$v = f(u) = k_1 + [k_2 + k_3 u + k_4 u^2]^{\frac{1}{2}},$$

where the k_n's are constants depending on the wing contour and Mach number. It can be shown that the integrals reduce to standard types, especially if the wing contour changes slowly so that $v = f(u)$ can be expressed by the first few terms of its Taylor series with reasonable accuracy.

6.4. Cambered Aerofoils

The procedure for cambered aerofoils is exactly the same as that for the flat plate aerofoils. The approximations intimated are sufficient to reduce the integrals to standard forms if the incidence distribution is given as a series, although the number of integrals to be evaluated rises appreciably as the complexity of the incidence increases. However, the method is straightforward, even if tedious, and has the fundamental advantage of being completely general.

References

1. Evvard, J. C. Use of Source Distribution for Evaluating Theoretical Aerodynamics of Thin Finite Wings at Supersonic Speeds. N.A.C.A. Report 951, 1950.
2. Robinson, A. Rotary Derivatives of a Delta Wing at Supersonic Speeds. *Journal of the Royal Aeronautical Society*, Vol. 52, pp. 735-752, November 1948.
3. Stewartson, K. On Linearized Potential Theory of Unsteady Supersonic Motion. Symposium on Aerodynamics. Institute of Aerophysics. University of Toronto, 1954.
4. Brown, C. E. Theoretical Lift and Drag on Thin Triangular Wings at Supersonic Speeds. N.A.C.A. Report 839, 1946.
5. Cohen, D. M. Formulae for Supersonic Loading, Lift, Drag of Flat Swept-Back Wings with Leading Edges behind Mach Lines. N.A.C.A. T.N. 1050, 1952.
6. Stewart, H. J. and Li, T. Y. Periodic Motions of a Rectangular Wing Moving at Supersonic Speeds. *Journal of the Aeronautical Sciences*, Vol. 17, pp. 529-539, September 1950.
7. Stewart, H. J. and Li, T. Y. On an Integral Equation in the Supersonic Oscillating Wing Theory. *Journal of the Aeronautical Sciences*, Readers Forum, Vol. 20, October 1953.
8. Evvard, J. C. Effects of Yawing Thin Pointed Wings at Supersonic Speeds. N.A.C.A. T.N. 1429, 1947.
9. Etkin, B. and Woodward, F. A. Lift Distribution on Supersonic Wings with Subsonic Leading Edges and Arbitrary Angles of Attack. Proceedings of the Second Canadian Symposium on Aerodynamics. Institute of Aerophysics. University of Toronto, 1954.